УДК 539.12; 539.125; 539.126; 539.128

SPIN STRUCTURE OF NUCLEONS: EXPERIMENTAL STATUS

I. A. Savin, A. P. Nagaitsev***

Joint Institute for Nuclear Research, Dubna

*E-mail: Igor.Savin@cern.ch; savin@sunse.jinr.ru

**E-mail: nagajcev@mail.desy.de

УДК 539.12; 539.125; 539.126; 539.128

SPIN STRUCTURE OF NUCLEONS: EXPERIMENTAL STATUS

I. A. Savin, *A. P. Nagaitsev***

Joint Institute for Nuclear Research, Dubna

The experimental data on inclusive and semi-inclusive cross sections of deep inelastic scattering of polarized leptons on polarized nucleons are reviewed in this paper. The results of these experiments are usually expressed in terms of spin-dependent structure functions of nucleons and used for testing of different theoretical predictions such as Quantum Chromodynamics, Bjorken sum rule, Ellis–Jaffe sum rules, Gerasimov–Drell–Hearn sum rules and others, as well as for determination of quark contributions to the spin of nucleons. A short summary of underlying theoretical works and description of experimental set-ups at CERN, DESY, and SLAC, where the experiments have been performed, precedes the data review.

Проведен обзор экспериментальных данных по изучению инклюзивных и полуинклюзивных сечений глубоконеупругих рассеяний поляризованных лептонов на поляризованных нуклонах. Результаты экспериментов выражаются в терминах структурных функций нуклонов, зависящих от спина, и используются для проверки различных теоретических предсказаний — квантовой хромодинамики, правила сумм Бьеркена, правил сумм Эллиса–Джаффе, Герасимова–Дрелла–Херна и др., а также для определения вклада в спин нуклонов их конституентных кварков. Обзору результатов предшествует краткое резюме соответствующих теоретических работ, а также описание экспериментальных установок в CERN, DESY и SLAC, на которых получены основные результаты.

1. INTRODUCTION AND THEORETICAL SUMMARY

Deep Inelastic lepton-nucleon Scattering (DIS) is a powerful method to study the quark-parton structure of nucleons, i. e., of the proton and neutron [1–6]. High energy DIS of polarized leptons on polarized nucleons also probes the polarization of quarks inside the polarized target and allows one to measure the contribution of quarks to the spin of the nucleon [7–30].

Cross sections of both polarized and unpolarized lepton-nucleon scattering are expressed via spin-dependent and spin-independent structure functions (SF) for which there are definite predictions of the modern theory of strong interactions — Quantum ChromoDynamics (QCD). QCD predicts the Q^2 evolution, or

───────────

*E-mail: Igor.Savin@cern.ch; savin@sunse.jinr.ru
**E-mail: nagajcev@mail.desy.de

dependence on the four-momentum transfer Q^2 from leptons to nucleons, of the structure functions and their sum rules. For the unpolarized SF, data confirm the QCD predictions. Precise measurements of spin-dependent structure functions constitute also important tests of QCD.

The fundamental Bjorken sum rule relates the first moments of the spin-dependent SF to the neutron β-decay coupling constants, i.e., the strong and weak-interaction processes. It is independent of the internal spin structure of nucleons, and its verification constitutes an important test of our understanding of the structure and interactions of elementary particles. The Bjorken sum rule is derived now in QCD and, being verified, can be used to determine the strong-interaction coupling constant $\alpha_s(Q^2)$.

The model-dependent sum rules, derived for the first time by J. Ellis and R. Jaffe, relate the first moments of the spin-dependent SF of the proton and neutron to the coupling constants characterizing the hyperon β decays of the baryon octet. At the finite Q^2, the Ellis–Jaffe sum rules are subjects of the QCD corrections. The experimental tests of these sum rules are very important for the verification of the underlying assumptions.

The first experiments to measure the polarized SF of the proton in inclusive DIS were performed at SLAC in 1978–1983 by using polarized electrons (experiments E80 and E130). Later, in 1989, similar measurements in a much larger kinematic range were performed at CERN by the European Muon Collaboration (EMC) [31–34] using polarized muons. The EMC experiment has demonstrated that the Ellis–Jaffe sum rule for the spin-dependent SF of the proton is violated by about 3 standard deviations. In the framework of Quark-Parton Model (QPM), the EMC results also indicated that the total contribution of quarks to the proton spin is small in contradiction with naive expectations. These surprising results triggered a series of new experiments aiming:

— to confirm the EMC measurements and extend them in an enlarged kinematic range,

— to perform similar measurements using different polarized targets: proton, deuterium, and ^{3}He and to test the Ellis–Jaffe sum rules in each case,

— to test the Bjorken sum rule for the first time,

— to study spin effects in Semi-Inclusive Deep Inelastic Scattering (SIDIS).

These new measurements, similarly to E80/E130 and EMC, were planned with longitudinally polarized leptons and nucleons producing the spin-dependent structure function $g_1(x, Q^2)$, where x is a dimensionless Bjorken variable interpreted in QPM as a fraction of nucleon momentum carried by a constituent quark. In addition to that, new experiments were planning to measure, for the first time, the second spin-dependent SF $g_2(x, Q^2)$ using transversely polarized targets.

Among the new experiments proposed in 1988–1989, the first ones which started to take and publish data, were the experiment NA47 by the Spin Muon Collaboration (SMC) at CERN [35–48] and experiments E142 and E143 at SLAC

[49–55]. These experiments were complimented later by E154 and E155 experiments at SLAC [69–76] and by HERMES at DESY [56–68]. The SLAC experiments E154 and E155 used the electron beam with the energy of 50 GeV. The HERMES experiment at DESY uses polarized positrons (or electrons) at 27.5 GeV. The data of these experiments together with the data of SLAC E80/130 and EMC represent the basis of the present experimental understanding of the nucleon spin structure.

New generation experiments on the spin structure of nucleons have been approved. They include experiments STAR and PHENIX at RHIC which started in 2000 with Au-Au collisions and with polarized protons up to 500 GeV in the centre of mass somewhat later. COMPASS experiment at CERN started at the same time and HERMES continues to operate until 2006. The well-known collaborations H1 and ZEUS at HERA, DESY turned attention to the possible spin effects in electron-proton collisions. New collaborations using the CEBAF Large Acceptance Spectrometer (CLAS) at the Thomas Jefferson National Accelerator Facility, USA, compliment the high energy spin-effects studies with investigations of spin observables related to the so-called Generalized Parton Distribution functions (GPD) at low energy of 4.5 GeV. There is also proposal to continue these studies at larger energies [83]. New spin-dependent SF's characterizing the transverse spin structure of nucleons will be measured for the first time. These experiments will compliment the existing data of E80/130, EMC, SMC, E142/143/154/155 and substantially improve our understanding of the nucleon spin structure including contributions to it from gluons and quark orbital momenta.

The paper is organized as follows. In Subsecs. 1.1–1.5 there is a summary of the theoretical overview of DIS cross sections and asymmetries as well as of structure functions g_1 and g_2 and their sum rules. One can find the complete theoretical review of spin physics in [7] and in more recent paper [8]. Section 2 briefly reminds how the first measurements of the structure function g_1 by the E80/E130 and EMC experiments created the so-called «spin crisis». Section 3 describes the experiments SMC, HERMES, SLAC E142/E154 and E143/155. The world data on spin-dependent SF's g_1 and g_2 are reviewed in Sec. 4. Section 5 outlines the data on Semi-Inclusive DIS (SIDIS) and the prospects. A short summary in Sec. 6 concludes the paper.

In many places the text closely follows the SMC [42] and other publications [35–85].

1.1. Polarized DIS Cross Sections. Inclusive deep inelastic scattering of polarized leptons ($\mathbf{l}$) on polarized nucleons ($\mathbf{N}$):

$$\mathbf{l} + \mathbf{N} \rightarrow l' + X \tag{1.1}$$

is a reaction probing the nucleon quark and spin structure. It is assumed that for the initial state one knows (measures):

— a 4-momentum, $k = (E_\ell, \mathbf{k})$, of the incident lepton, which can be either electron (e) or muon (μ);

— orientation of the lepton spin, S_l, with respect to the lepton momentum;

— orientation of the nucleon spin, S_N, with respect to the lepton momentum, too.

In the final state one needs to identify a scattered lepton, ℓ', and measure its scattering angle, θ, and momentum, p' (or energy, E'). Other particles (hadrons), X, produced in reaction (1.1) are not taken into account for inclusive DIS. One, two or more particles out of X are identified and measured for SIDIS reactions. The standard DIS notations are used in the text:

$$Q^2 = 4EE' \sin^2(\theta/2), \quad \nu = E - E', \quad y = (E - E')/E, \quad x = Q^2/2M\nu,$$

M is a mass of the proton.

A quantitative characteristic of the reaction (1.1) is a double differential cross section, $\boldsymbol{\sigma} \equiv d^2\boldsymbol{\sigma}/d\Omega dE'$. This cross section can be calculated theoretically assuming that the main contribution to it comes from the one-photon exchange process, represented by a diagram in Fig. 1, a, i.e.,

$$\boldsymbol{\sigma} = \boldsymbol{\sigma}_{\text{one-photon}} + \boldsymbol{\sigma}_{\text{RC}},$$

where $\boldsymbol{\sigma}_{\text{RC}}$ is a contribution from other radiative processes (Radiative Corrections) [86].

It is known [2] that one-photon exchange cross section is defined as

$$\boldsymbol{\sigma}_{\text{one-photon}} \equiv \frac{d^2\boldsymbol{\sigma}^{S_\ell S_N}}{d\Omega dE'} = \left(\frac{4\alpha^2}{Q^4} \frac{E'}{E} \right) L_{\mu\nu} W^{\mu\nu}, \tag{1.2}$$

where the term in brackets characterizes the point-like interaction, $L_{\mu\nu}$ is a lepton current tensor representing the lepton vertex in Fig. 1, a and $W^{\mu\nu}$ is a hadronic tensor amplitude characterizing the hadron vertex structure. The tensors have two parts, one of which (SIM) is independent of the spin orientations and the second one (ASIM) is spin-dependent:

$$L_{\mu\nu} = L_{\mu\nu}^{\text{SIM}} + iL_{\mu\nu}^{\text{ASIM}}, \quad W^{\mu\nu} = W_{\text{SIM}}^{\mu\nu} + iW_{\text{ASIM}}^{\mu\nu}. \tag{1.3}$$

The form of $L_{\mu\nu}$ is exactly known from Quantum ElectroDynamics (QED). The hadronic tensor $W^{\mu\nu}$ is not calculated theoretically. It is a pure phenomenological quantity characterizing the nucleon structure. Theory tells us that from the most common considerations for electromagnetic interactions $W^{\mu\nu}$ should have the form:

$$\begin{aligned}
W_{\text{SIM}}^{\mu\nu} &= A_1^{\mu\nu}(q, q')W_1(Q^2, \nu) + A_2^{\mu\nu}(q, q')W_2(Q^2, \nu), \\
W_{\text{ASIM}}^{\mu\nu} &= B_1^{\mu\nu}(q, q')G_1(Q^2, \nu) + B_2^{\mu\nu}(q, q')G_2(Q^2, \nu),
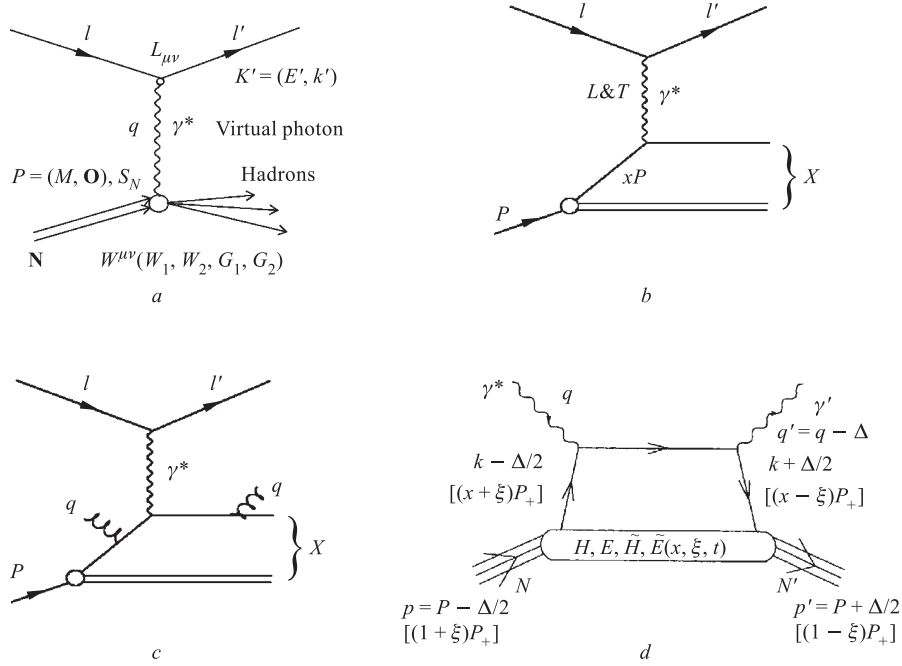\end{aligned} \tag{1.4}$$

Fig. 1. The Feynman diagrams of DIS in one-photon exchange approximation. *a*) A virtual photon transferring a four-momentum squared, Q^2, and energy, ν, and having longitudinal or transverse polarization is absorbed by nucleon; variables: $-q^2 \equiv Q^2 = -(k - k')^2 = 4EE' \sin^2(\theta/2)$; $\nu = PQ/M = E - E'$; $x = Q^2/2M\nu$; $y = \nu/E$; *b*) in QPM the virtual photon is absorbed by a constituent quark carrying the fraction of the nucleon momentum x; *c*) in QCD the quark absorbing virtual photon can emit gluons before or after absorption; *d*) hand-bag diagram introducing GPD (see Subsec. 1.5.4 for details)

where A_1, A_2, B_1, and B_2 are known kinematic expressions; $W_1(Q^2, \nu)$ and $W_2(Q^2, \nu)$ are spin independent and $G_1(Q^2, \nu)$ and $G_2(Q^2, \nu)$ are spin-dependent structure functions representing the nucleon structure. In general, these structure functions should be functions of two independent variables — either (Q^2, ν); or (Q^2, x); or (x, y), etc. But in the DIS (scaling) limit $(Q^2, \nu \to \infty, x$ fixed), following the Bjorken hypothesis, the structure functions become the functions of only one (Bjorken) scaling variable x:

$$
\begin{aligned}
MW_1(Q^2, \nu) &\to F_1(x), \\
\nu W_2(Q^2, \nu) &\to F_2(x), \\
\nu M^2 G_1(Q^2, \nu) &\to g_1(x), \\
\nu^2 M G_2(Q^2, \nu) &\to g_2(x).
\end{aligned}
\tag{1.5}
$$

Performing the calculations as prescribed by Eq. (1.2) and summing over the spin orientations of scattered leptons, which are usually not known, one can get that

$$\frac{d^2\boldsymbol{\sigma}^{S_e S_N}}{d\Omega dE'} = \frac{d^2\sigma^{\mathrm{unp}}}{d\Omega dE'} + S_N S_e \frac{d^2\sigma^{\mathrm{pol}}}{d\Omega dE'}, \qquad (1.6)$$

where σ^{unp} (σ^{pol}) is an unpolarized (polarized) part of the cross section and $S_N = \pm 1$ is orientation (helicity) of the nucleon spin.

In the most commonly used notations the spin-independent part of the cross section, σ^{unp}, is expressed via two spin-independent structure functions F_1 and F_2:

$$\frac{d^2\sigma^{\mathrm{unp}}}{dxdQ^2} = \frac{4\pi\alpha^2}{Q^2 x}\left[xy^2 \left(1 - \frac{2m_e^2}{Q^2} \right) F_1(x,Q^2) + \right.$$

$$\left. + \left(1 - y - \frac{\gamma^2 y^2}{4} \right) F_2(x,Q^2) \right], \quad (1.7)$$

where m_e is the lepton mass and $\gamma = 2Mx/\sqrt{Q^2} = \sqrt{Q^2}/\nu$. The σ^{unp} is also expressed via $F_2(x,Q^2)$ and $R(x,Q^2) = \sigma_L/\sigma_T$, where $\sigma_L \sigma_T)$ is a cross section of the absorption by nucleon of virtual photons with longitudinal (transverse) polarization:

$$\sigma^{\mathrm{unp}} \equiv \frac{d^2\sigma^{\mathrm{unp}}}{dxdQ^2} =$$

$$= \frac{4\pi\alpha^2}{Q^4 x} F_2(x,Q^2) \left[1 - y - \frac{y^2 \gamma^2}{4} + \frac{y^2(1+\gamma^2)}{2(1+R(x,Q^2))} \right]. \quad (1.7a)$$

The structure functions $R(x,Q^2)$ and $F_2(x,Q^2)$ have been measured by the well-known collaborations SLAC, EMC, BCDMS, NMC and others (see [6]).

The spin-dependent part of the cross section (1.6), or σ^{pol}, can be separated from the σ^{unp} in the so-called asymmetries which are proportional to the difference of cross sections for two opposite target polarizations. In the general case, when the angle between the lepton scattering plane (see Fig. 2) and the target polarization plane is ϕ, and the angle between the incident lepton momentum and the target polarization vector is ψ, the difference of cross sections is given by the following expression:

$$\Delta\sigma \equiv \frac{d^3\left[\boldsymbol{\sigma}(\psi) - \boldsymbol{\sigma}(\psi+\pi)\right]}{dx\, dy\, d\phi} = \frac{4\pi\alpha^2}{Q^2}\left[B\cos\psi - C\sin\psi\cos\phi \right],$$

where

$$B = \left[1 - \frac{y}{2} - \frac{y^2}{4}\gamma^2 \right] g_1(x,Q^2) - \frac{y^2\gamma^2}{2} g_2(x,Q^2)$$
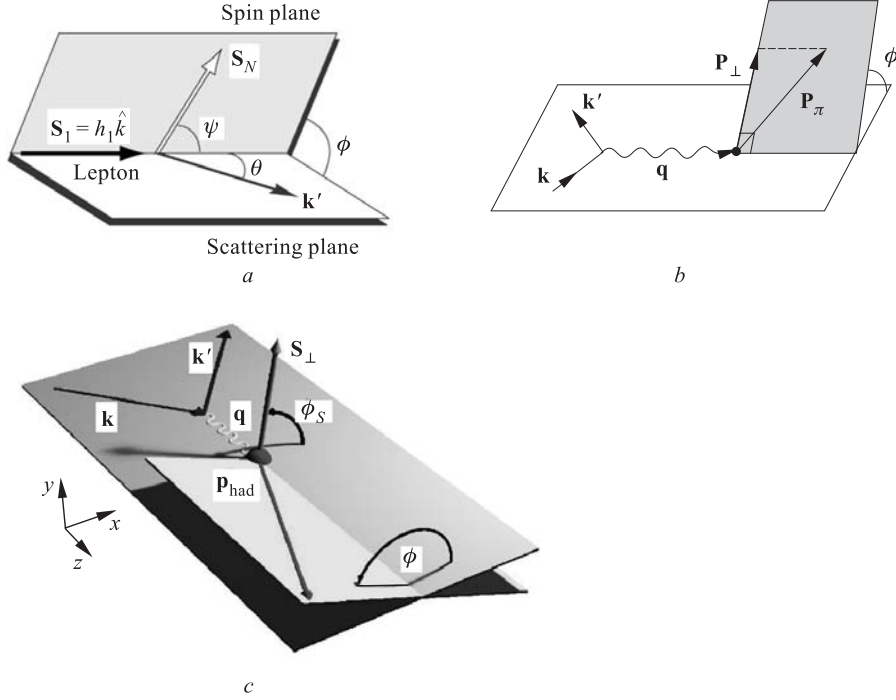
Fig. 2. Vectors characterizing the DIS of polarized leptons on polarized nucleon in inclusive (*a*) and semi-inclusive (*b*) processes and the definition of the «Collins angle» $\phi_c = \phi - \phi_S$ (*c*), where $\mathbf{S}_\perp$ is a vector of the quark spin, see Subsec. 1.5.5 for details

and

$$C = \sqrt{\gamma^2 \left(1 - y - \frac{y^2}{4}\gamma^2\right)} \left[\frac{y}{2}g_1(x, Q^2) + g_2(x, Q^2)\right].$$

Obviously, the measurements with $\psi = 0°$, or with longitudinally polarized nucleons, will give B, while the measurements with $\psi = 90°$, or with transversely polarized nucleons, will give C. The measurements of both B and C permit one to separate g_1 and g_2.

Differences of cross sections for two opposite longitudinal, $\Delta\sigma_\parallel$, and transverse, $\Delta\sigma_\perp$, target polarizations are given by the expressions:

$$\Delta\sigma_\parallel \equiv \Delta\left(\frac{d^2\sigma_\parallel^{\text{pol}}}{dxdQ^2}\right) = \frac{16\pi\alpha^2 y}{Q^4}\left[\left(1 - \frac{y}{2} - \frac{y^2\gamma^2}{4}\right)g_1 - \frac{y\gamma^2}{2}g_2\right],$$

$$\Delta\sigma_\perp \equiv \Delta\left(\frac{d^2\sigma_\perp^{\text{pol}}}{dxdQ^2}\right) = -\cos\phi\frac{8\alpha^2 y\gamma}{Q^4}\sqrt{1-y-\frac{y^2\gamma^2}{4}}\left(\frac{y}{2}g_1 + g_2\right).$$

The polarized part of the cross section (1.6), σ^{pol}, is small compared to σ^{unp} and its contribution to the experimental counting rate is further reduced by incomplete beam and target polarizations. So, to separate σ^{pol}, instead of measurements of differences of the cross sections (1.6), the experimentalists measure the asymmetries in which σ^{unp} is cancelled in numerators. The longitudinal, or $A_\parallel$, and transverse, or $A_\perp$, asymmetries are defined as:

$$A_\parallel = \frac{\Delta\sigma_\parallel}{2\sigma^{\text{unp}}} = \frac{\sigma^{\to\Rightarrow} - \sigma^{\to\Leftarrow}}{\sigma^{\to\Leftarrow} + \sigma^{\to\Rightarrow}}, \quad A_\perp = \frac{\Delta\sigma_\perp}{2\sigma^{\text{unp}}} = \frac{\sigma^{\to\Uparrow} - \sigma^{\to\Downarrow}}{\sigma^{\to\Uparrow} + \sigma^{\to\Downarrow}}, \qquad (1.8)$$

where $\to$ indicates polarization of incident lepton and $\Rightarrow$ ($\Uparrow$) indicates polarization of the target. They are related to the virtual photon asymmetries A_1 and A_2 (see Subsec. 1.2.1) by expressions:

$$A_\parallel = D(A_1 + \eta A_2), \quad A_\perp = d(A_2 - \varepsilon A_1), \qquad (1.9)$$

where

$$A_1 = \frac{g_1 - \gamma^2 g_2}{F_1} = \frac{\sigma_{1/2} - \sigma_{3/2}}{\sigma_{1/2} + \sigma_{3/2}}, \quad A_2 = \gamma\frac{g_1 + g_2}{F_1} = \frac{2\sigma_{TL}}{\sigma_{1/2} + \sigma_{3/2}}, \qquad (1.10)$$

and the quantities D, η, d and ε are defined as follows:

$$d = \frac{\sqrt{1-y-\gamma^2 y^2/4}}{1-y/2}D, \quad \eta = \frac{\gamma(1-y-\gamma^2 y^2/4)}{(1-y/2)(1+\gamma^2 y/2)}, \quad \varepsilon = \frac{\gamma(1-y/2)}{1+\gamma^2 y/2},$$

$$D = \frac{y(2-y)(1+\gamma^2 y/2)}{(1+\gamma^2)[y^2(1-2m_e^2/Q^2) + 2(1-y-\gamma^2 y^2/4)(1+R)/(1+\gamma^2)]}.$$
$$(1.11)$$

The $\sigma_{1/2}$ and $\sigma_{3/2}$ are absorption cross sections of virtual photons (γ^*) by nucleons (see Fig. 1) with the total photon-nucleon angular momentum along the γ^* axis of 1/2 and 3/2, respectively; σ_L and σ_T are absorption cross sections of longitudinally and transversely polarized virtual photons, and σ_{TL} is an interference cross section. With these cross sections one can have alternative expressions of asymmetries (right sides of Eq. (1.10)).

The second terms in Eq. (1.9) are estimated to be small. Then in the first approximation

$$\frac{A_\parallel}{D} \approx A_1 = \frac{g_1 - \gamma^2 g_2}{F_1} \approx \frac{g_1}{F_1}, \quad \frac{A_\perp}{d} \approx A_2 = \gamma\frac{g_1 + g_2}{F_1}, \qquad (1.12)$$

where $F_1 = \dfrac{1 + \gamma^2}{2x(1 + R)} F_2$ is the usual expression of F_1 in terms of structure functions $F_2(x, Q^2)$ and $R(x, Q^2)$.

1.2. Structure Function g_1. *1.2.1. Asymmetry A_1 and Structure Function g_1 in the Quark Parton Model.* As we have seen, A_1 is a dominant asymmetry for the longitudinally polarized leptons and nucleons.

In the Quark Parton Model (QPM) DIS is represented by a diagram in Fig. 1, *b*: virtual photon is absorbed by a constituent quark carrying the fraction x of the nucleon momentum. Due to conservation of the total angular momentum, this photon can be absorbed only by a quark having the spin oriented in the opposite direction to the photon angular momentum. Schematically:

$$\gamma^\uparrow q^\downarrow \to q^\uparrow, \quad \gamma^\downarrow q^\uparrow \to q^\downarrow, \quad \gamma^\uparrow q^\uparrow \text{ or } \gamma^\downarrow q^\downarrow \to \text{ no interactions.} \tag{1.13}$$

Now let us consider the cross section $\sigma^p_{1/2}$ for protons. Remind that it is a cross section corresponding to absorption of virtual photons when the total angular momentum of photon and proton is 1/2. Schematically:

$$\sigma^p_{1/2} : \gamma^\downarrow + p^\uparrow = \gamma^\downarrow + \begin{pmatrix} u^\uparrow u^\uparrow d^\downarrow \\ u^\downarrow u^\uparrow d^\uparrow \\ \text{::::::::::::} \end{pmatrix} \to \sum_i e_i^2 q_i^\uparrow(x). \tag{1.14}$$

It is seen that due to (1.13) only those quarks will absorb photons, whose spins are oriented along the spin of the proton.

Similarly:

$$\sigma^p_{3/2} : \gamma^\uparrow + p^\uparrow = \gamma^\uparrow + \begin{pmatrix} u^\uparrow u^\uparrow d^\downarrow \\ \text{.............} \\ \text{.............} \end{pmatrix} \to \sum_i e_i^2 q_i^\downarrow(x), \tag{1.15}$$

i.e., only those quarks contribute to this cross section, whose spins are oriented opposite to the spin of the proton. Taking the difference and the sum of Eqs. (1.14) and (1.15), one can get the asymmetry:

$$A_1^p = \frac{\sigma^p_{1/2} - \sigma^p_{3/2}}{\sigma^p_{1/2} + \sigma^p_{3/2}} = \frac{\sum e_i^2 \left[q_i^\uparrow(x) - q_i^\downarrow(x) \right]}{\sum e_i^2 \left[q_i^\uparrow(x) + q_i^\downarrow(x) \right]}. \tag{1.16}$$

The denominator of this expression by definition is equal to the unpolarized structure function $F_1^p(x)$ and the numerator is associated with the structure function g_1 (see Eq. (1.12)):

$$g_1(x) = \sum_i e_i^2 \left[q_i^\uparrow(x) - q_i^\downarrow(x) \right], \tag{1.17}$$

which is, averaged over the squared quark flavor charges, the difference of probabilities to find in a longitudinally polarized nucleon the quark carrying a fraction x of the nucleon momentum and having a spin aligned along and opposite to the nucleon spin. In other words, g_1 gives information on the quark spin orientation with respect to the nucleon spin.

Eqs. (1.16) and (1.17) predict the possible x behaviour of A_1 and g_1. Let us consider the case when $x \to 0$. From unpolarized DIS it is known that in this case virtual photons are absorbed mostly by sea quarks from $q\bar{q}$ pairs produced by gluons and decoupled from the valence quarks carrying the information on the nucleon spin. Then it is expected that probabilities $q_i^\uparrow$ and $q_i^\downarrow$ are approximately equal and $A_1(x \to 0) \to 0$ and $g_1(x \to 0) \to 0$. In other extreme case, when $x \to 1$, a single quark carries almost the whole nucleon momentum and, presumably, its spin. Then the probability for this quark to have the spin oriented in the opposite direction is small, i. e., $q_i^\downarrow(x \to 1) \to 0$, and $A_1(x \to 1) \to 1$. It is obvious that $|A_1(x)| \leqslant 1$ at any x.

1.2.2. The g_1 in QCD. In QCD quarks inside the nucleon interact via the gluon exchange. So, the quark, which in DIS absorbs the virtual photon, can emit the gluon before or after absorption (Fig. 1, c). This gives a Q^2 dependence of the structure functions proved in unpolarized experiments. The QCD treatment of unpolarized structure functions is well developed [87–93].

The QCD treatment of g_1 is developing now and closely follows that for unpolarized SF. Briefly, at a given scale Q^2 the g_1 is related to the polarized quark and gluon distributions by coefficient functions C_q and C_g corresponding to the photon-quark and photon-gluon scattering cross sections, respectively:

$$g_1(x,t) = \frac{1}{2} \sum_{k=1}^{n_f} \frac{e_k^2}{n_f} \int\limits_x^1 \frac{dy}{y} \left[C_q^S \left(\frac{x}{y}, \alpha_s(t) \right) \Delta\Sigma(y,t) + \right.$$

$$\left. + 2n_f C_g \left(\frac{x}{y}, \alpha_s(t) \right) \Delta g(y,t) + C_q^{NS} \left(\frac{x}{y}, \alpha_s(t) \right) \Delta q^{NS}(y,t) \right]. \quad (1.18)$$

Here $t = \ln(Q^2/\Lambda^2)$; e_k is the quark charge; $\alpha_s(t)$ is the strong coupling constant; Λ is the scale parameter of QCD; n_f is a number of the active flavors; superscripts S and NS indicate the flavor singlet and nonsinglet parton distributions, respectively; $\Delta\Sigma$, Δq^{NS} and Δg are the polarized singlet quark, nonsinglet quark, and gluon distributions, respectively. The coefficient functions are calculated in perturbative QCD (pQCD) as a power series of the α_s. Singlet and

nonsinglet combinations of polarized quarks and antiquarks distributions are:

$$\Delta\Sigma(x,t) = \sum_{i=1}^{n_f} \Delta q_i(x,t),$$

$$\Delta q^{NS}(x,t) = \frac{\sum_{i=1}^{n_f} \left(e_i^2 - 1/n_f \sum_{k=1}^{n_f} e_k^2 \right)}{1/n_f \sum_{k=1}^{n_f} e_k^2} \Delta q_i(x,t).$$

The t dependence of the distributions is determined by Gribov–Lipatov–Altarelli–Parisi (GLAP) equations [87, 88]:

$$\frac{d}{dt}\Delta\Sigma(x,t) = \frac{\alpha_s(t)}{2\pi} \int_x^1 \frac{dy}{y} \left[P_{qq}^S \left(\frac{x}{y}, \alpha_s(t) \right) \Delta\Sigma(y,t) + \right.$$

$$\left. + 2n_f P_{qg} \left(\frac{x}{y}, \alpha_s(t) \right) \Delta g(y,t) \right], \quad (1.19)$$

$$\frac{d}{dt}\Delta g(x,t) = \frac{\alpha_s(t)}{2\pi} \int_x^1 \frac{dy}{y} \left[P_{gq} \left(\frac{x}{y}, \alpha_s(t) \right) \Delta\Sigma(y,t) + \right.$$

$$\left. + P_{gg} \left(\frac{x}{y}, \alpha_s(t) \right) \Delta g(y,t) \right], \quad (1.20)$$

$$\frac{\Delta}{dt}\Delta q^{NS}(x,t) = \frac{\alpha_s(t)}{2\pi} \int_x^1 \frac{dy}{y} P_{qq}^{NS} \left(\frac{x}{y}, \alpha_s(t) \right) \Delta q^{NS}(y,t), \quad (1.21)$$

where P_{ij} are splitting functions for polarized parton distributions known in QCD. The set of coefficient functions [128, 129] and splitting functions [98] has been computed up to Next-to-Leading Order (NLO) in α_s, i. e., up to α_s^2. At NLO these functions and, in general, parton distributions depend on the renormalization and factorization schemes while the physics observables, such as g_1 and others, should remain scheme-independent. Parton distributions in different schemes can be different but they are related to each other by well-defined transformations [106].

Knowing the splitting and coefficient functions, one can perform QCD analysis of spin-dependent structure functions starting from the parameterization of the parton distributions at the initial value Q_i^2, which is usually found from fits to the experimental data. Then the distributions at any value of Q^2 are obtained from the solutions of the GLAP equations.

The renormalization scheme choice is arbitrary. Two widely used schemes are the $\overline{MS}$ scheme [5] and the Adler–Bardeen (AB) scheme [96, 101] which is a modified $\overline{MS}$ scheme. The transformation from $\overline{MS}$ to AB scheme is constructed in paper [96]. In the $\overline{MS}$ scheme the first moment of the gluon coefficient function C_g is equal to zero, which implies that gluon distribution $\Delta g(x, Q)^2$ does not contribute to the integral $\Gamma_1 = \int_0^1 g_1(x)dx$. The first moments of the singlet quark distribution in two schemes differ:

$$\Delta\Sigma_{\overline{MS}}(Q^2) = \Delta\Sigma_{\mathrm{AB}} - n_f \frac{\alpha_s(Q^2)}{2\pi}\Delta g(Q^2),$$

where $\Delta g(Q^2)$ is the value of Δg obtained from the analysis performed in the AB scheme.

As is seen from (1.12), the asymmetry A_1 is approximately equal to the ratio g_1/F_1. In QCD this ratio is Q^2-dependent because the splitting functions are different for polarized and unpolarized parton distributions. This is due to gluons known to be distributed mainly at small x. However, in a kinematic region dominated by valence quarks ($x \gtrsim 0.1$), the Q^2 dependence of g_1/F_1 is expected to be small [98].

Practical formalizms of the QCD analysis of polarized structure functions have been developed in papers [106, 107].

1.2.3. Small-x Behaviour of g_1. The naive considerations of the small-x behaviour of $g_1(x)$ are presented in Subsec. 1.2.1. In fact there is no unique theoretical approach to this question.

From the Regge theory it is expected that at $x \to 0$ for fixed moderate Q^2 and $\nu \to \infty$, $g_1(x)$ behaves like $x^{-\alpha}$, where α is an intercept of the contributing Regge trajectory which is of a meson a_1 or f_1. The intercepts of these trajectories are negative in the limits: $-0.5 < \alpha < 0$.

The Donnachie–Landshoff model [120] of a spin-dependent diffractive scattering predicts for $g_1(x)$ at small x the behaviour of the type: $g_1(x) \sim [2\ln(1/x) - 1]$.

A very divergent dependence like $g_1(x) \sim (x \ln^2 x)^{-1}$ is suggested in [121].

In QCD considerations [122] it is estimated that $(\ln 1/x)^a \ll g_1(x) \ll x^{-b}$, where a and b are positive. Other QCD analyses [123] suggest that

$$g_1^{NS}(x, Q^2) \sim x^{-0.4}\left(\frac{Q^2}{\mu^2}\right)^{0.2} \quad \text{or} \quad g_1^S(x, Q^2) \sim x^{-1}\left(\frac{Q^2}{\mu^2}\right)^{0.5}.$$

None of these predictions have been proved experimentally.

Fits of the QCD predictions (1.18) to the data on $g_1(x, Q^2)$ in the region of measurements and corresponding extrapolations provide practical predictions for the unmeasured small-x region (see Subsec. 4.1 below).

1.2.4. The Bjorken Sum Rule. The important predictions for structure functions g_1 of the proton, $g_1^p(x)$, and neutron, $g_1^n(x)$, exist in the form of sum rules involving the first moments of $g_1(x)$:

$$\Gamma_1^{p,n} = \int\limits_0^1 g_1^{p,n}(x)dx.$$

The most important sum rule has been obtained by Bjorken [124] in 1966–1970 for the difference of the first moments of $g_1^p(x)$ and $g_1^n(x)$, $\Gamma_1^p - \Gamma_1^n$:

$$\Gamma_1^p - \Gamma_1^n \equiv \int\limits_0^1 \left[g_1^p(x) - g_1^n(x)\right] dx = \frac{1}{6}\left|\frac{g_A}{g_V}\right|,$$

where $g_A(g_V)$ is the axial vector (vector) weak interactions coupling constant determined from nucleon β decays.

To derive this sum rule, the quark current algebra technique was used together with standard quark-charge assignments and assumption on validity of the isospin symmetry. This sum rule is of the fundamental character because it is independent of nucleon spin structure details. The failure of it would have an impact on present understanding of high energy physics and structure of particles.

The Bjorken sum rule in the above form is of the asymptotic character, i. e., at $Q^2 \to \infty$. At the finite Q^2 it is a subject of QCD corrections:

$$\Gamma_1^p(Q^2) - \Gamma_1^n(Q^2) = \frac{1}{6}\left|\frac{g_A}{g_V}\right|C_1^{NS}(Q^2). \tag{1.22}$$

At present these corrections are calculated up to $\alpha_s^3(Q^2)$ [125–127]:

$$C_1^{NS}(Q^2) = \left[1 - \frac{\alpha_s}{\pi} - 3.5833\frac{\alpha_s^2}{\pi^2} - 20.2153\frac{\alpha^3}{\pi^3} - O(130)\frac{\alpha^4}{\pi^4} + \dots\right]. \tag{1.23}$$

A powerful method of calculations of structure function moments is provided by the Operator Product Expansion (OPE) technique. Using this technique one can reduce the product of the leptonic and hadronic tensors entering in Eq. (1.2) to the expansion of the product of two electromagnetic currents. It is shown in [126–131], that only NS- and S-axial currents contribute to this product at leading twist and the first moment of g_1 is given by

$$s_\mu \Gamma_1^{p(n)}(Q^2) = \frac{C_1^{NS}(Q^2)}{6}\left\{+(-)\langle ps|A_\mu^3|ps\rangle + \frac{1}{\sqrt{3}}\langle ps|A_\mu^8|ps\rangle\right\} +$$
$$+ \frac{C_1^S(Q^2)}{2}\left\{\langle ps|A_\mu^0|ps\rangle\right\}, \tag{1.24}$$

where $A_\mu^k = \bar\psi(\lambda_k/2)\gamma_5\gamma_\mu\psi$, $\lambda_k(k = 1,\dots,8)$ and $\lambda_0 = 2I$ are Gell-Mann $SU(3)$ flavor matrices, and s_μ is a covariant spin vector.

Proton (or neutron) matrix elements of (1.24) can be written in terms of the axial matrix elements (axial couplings) $a_i(Q^2)$ for flavor q_i, $s_\mu a_i(Q^2) = \langle ps|\bar q_i\gamma_5\gamma_\mu q_i|ps\rangle$:

$$\langle ps|A_\mu^3|ps\rangle = \frac{s_\mu}{2}a_3 = \frac{s_\mu}{2}(a_u - a_d) = \frac{s_\mu}{2}\left|\frac{g_A}{g_V}\right|, \qquad (1.25)$$

$$\langle ps|A_\mu^8|ps\rangle = \frac{s_\mu}{2\sqrt3}a_8 = \frac{s_\mu}{2\sqrt3}(a_u + a_d - 2a_s), \qquad (1.26)$$

$$\langle ps|A_\mu^0|ps\rangle = s_\mu a_0 = s_\mu(a_u + a_d + a_s) = s_\mu a_0(Q^2). \qquad (1.27)$$

If the exact $SU(3)$ symmetry is assumed for flavor currents, the axial couplings a_3 and a_8 can be expressed via coupling constants F and D obtained from hyperon β decays [9132]:

$$a_3 = F + D = g_A/g_V, \quad a_8 = 3F - D. \qquad (1.28)$$

The Bjorken sum rule in OPE technique is obtained from Eq. (1.24):

$$\Gamma_1^p(Q^2) - \Gamma_1^n(Q^2) = \frac{1}{6}\left|\frac{g_A}{g_V}\right|C_1^{NS}, \qquad (1.29)$$

where C_1^{NS} is the nonsinglet coefficient function depending on the number of flavors and renormalization scheme. For three flavors and $\overline{MS}$ renormalization scheme it is given by Eq. (1.23).

1.2.5. The Ellis–Jaffe Sum Rules. Originally the Ellis–Jaffe sum rules [132] for the first moments of structure functions $g_1(x)$ of the proton and neutron have been obtained by using the quark current algebra and assuming the isospin symmetry, standard quark-charge assignments, $SU(3)$ symmetry in decays of octet baryons and zero net polarization for strange sea quarks:

$$\Gamma_1^{p(n)} = +(-)\frac{1}{12}(F + D) + \frac{5}{36}(3F - D). \qquad (1.30)$$

In QCD the Ellis–Jaffe sum rules follow from Eqs. (1.24)–(1.27) assuming $a_s = 0$ and using (1.28):

$$\Gamma_1^{p(n)} = C_1^{NS}\left[+(-)\frac{1}{12}\left|\frac{g_A}{g_V}\right| + \frac{1}{36}(3F - D)\right] + \frac{1}{9}C_1^S(3F - D), \qquad (1.31)$$

where C_1^{NS} is given by Eq. (1.23) and the singlet coefficient function C_1^S for three flavors in the $\overline{MS}$ renormalization scheme is equal to:

$$C_1^S(Q^2) = 1 - \frac{\alpha_s}{\pi} - 1.0959\frac{\alpha_s^2}{\pi^2} - O(6)\frac{\alpha_s^3}{\pi^3}. \qquad (1.32)$$

1.2.6. Quark Contributions to the Spin of the Nucleon. Since in QPM the nucleon is not an elementary particle, its spin should be composed of spins and orbital momenta of constituent partons. From unpolarized DIS it is known that nucleons consist of valence and sea quarks and gluons with the help of which quarks interact. One can naturally assume that the spin of the nucleon, which is equal to 1/2, should be composed of spins of quarks, $1/2\Delta\Sigma$, its angular momenta, L_q, spins of gluons, Δg, and its angular momenta, L_g:

$$S_z^p = \frac{1}{2} = \frac{1}{2}\Delta\Sigma + L_q + \Delta g + L_g. \tag{1.33}$$

The contribution $\Delta\Sigma$ can be determined from measurements of Γ_1^p, Γ_1^n, and Γ_1^d. Using the definition of the structure function $g_1(x)$ as given by Eq. (1.17), the integrals can be written in the forms:

$$\Gamma_1^p = \int_0^1 dx g_1^p(x) = \int_0^1 \frac{1}{2}dx e_i^2[q_i^{\uparrow p} - q_i^{\downarrow p}] = \frac{1}{2}\left[\frac{4}{9}\Delta u + \frac{1}{9}\Delta d + \frac{1}{9}\Delta s + \dots\right],$$

$$\Gamma_1^n = \int_0^1 dx g_1^n(x) = \int_0^1 \frac{1}{2}dx e_i^2[q_i^{\uparrow n} - q_i^{\downarrow n}] = \frac{1}{2}\left[\frac{1}{9}\Delta u + \frac{4}{9}\Delta d + \frac{1}{9}\Delta s + \dots\right],$$

$$\Gamma_1^d \approx \frac{1}{2}[\Gamma_1^p + \Gamma_1^n] = \frac{1}{2}\left[\frac{5}{9}\Delta u + \frac{5}{9}\Delta d + \frac{2}{9}\Delta s + \dots\right],$$

where $\Delta u = \int_0^1 dx \left[u^{\uparrow p} - u^{\downarrow p}\right]$; $\Delta d = \int_0^1 dx \left[d^{\uparrow p} - d^{\downarrow p}\right]$ and $\Delta s = \int_0^1 dx[s^{\uparrow p} - s^{\downarrow p}]$ are contributions to the integrals from u, d, and s quarks. By the definition of the structure function g_1, Δu (Δd and Δs) is proportional to the total difference of probabilities for quarks u (d and s) to have spin parallel and antiparallel to the proton spin, i. e., contribution of quarks u (d and s) to the proton spin. Assuming that there are only three active flavors contributing to DIS at present energies and that $\Delta s = 0$, i. e., the strange sea is symmetric and does not contribute to asymmetries $A_1(x)$, then Δu and Δd can be separated from measurements of Γ_1^p and Γ_1^d or Γ_1^p and Γ_1^n.

In the general QCD approach using the OPE technique, the first moments $\Gamma^{p(n)}$ are given by Eq. (1.24) from which, and also from Eqs. (1.25)–(1.27), it follows that

$$\Gamma_1^p(Q^2) = \frac{1}{12}\left[\left(a_3 + \frac{1}{3}a_8\right)O_1(\alpha_s) + \frac{4}{3}a_0 O_2(\alpha_s)\right], \tag{1.34}$$

$$\Gamma_1^n(Q^2) = \frac{1}{12}\left[\left(-a_3 + \frac{1}{3}a_8\right)O_1(\alpha_s) + \frac{4}{3}a_0 O_2(\alpha_s)\right], \tag{1.35}$$

where $O_i(\alpha_s)$ are known QCD corrections; a_0 is the $SU(3)$ flavor singlet and a_3 and a_8 are flavor nonsinglet axial current matrix elements (axial couplings). It is known (see Eq. (1.28)) that these couplings are expressed via F and D coupling constants determined from [133] hyperon decays:

$$a_3 = g_A/g_V = F + D = 1.2573 \pm 0.0028, \tag{1.36}$$

$$a_8 = (3F - D) = 0.579 \pm 0.025. \tag{1.37}$$

From Eqs. (1.34)–(1.37) one can determine a_0, a_3, and a_8.

In the naive QPM the axial couplings are related with quark contributions to the nucleon spin:

$$a_0 = \Delta\Sigma = \Delta u + \Delta d + \Delta s,$$
$$a_3 = \Delta u - \Delta d, \tag{1.38}$$
$$a_8 = \Delta u + \Delta d - 2\Delta s.$$

So, measuring the first moments Γ_1^p and Γ_1^n and knowing the F and D coupling constants from hyperon β decays, one can determine the total quark spin contribution and contributions of flavors u, d, and s to the nucleon spin.

The relations (1.38) are broken in QCD because gluons also contribute to $a_0(Q^2)$ and this contribution depends on Q^2. In the $\overline{MS}$ scheme the relation between a_0 and $\Delta\Sigma$ remains the same but now it is Q^2-dependent:

$$a_0(Q^2) = \Delta\Sigma_{\overline{MS}}(Q^2).$$

In the Adler–Bardeen [101–105] factorization scheme

$$a_0(Q^2) = \Delta\Sigma_{\mathrm{AB}} - n_f \frac{\alpha_S(Q^2)}{2\pi} \Delta g_{\mathrm{AB}}(Q^2), \tag{1.39}$$

where $\Delta\Sigma_{\mathrm{AB}}$ is independent of Q^2. This is an attractive feature of the AB scheme. The difference between schemes does not vanish with $Q^2 \to \infty$. So, the interpretation of axial couplings in terms of quark contributions to the nucleon spin is not unique in QCD.

1.3. Structure Function g_2**.** The structure function g_2 of nucleons has no direct physics interpretation. It is of a pure phenomenological nature and appears due to interference in the absorption of transversely and longitudinally polarized virtual photons by the nucleon. Due to that, g_2 contains contributions from both the longitudinal and transverse polarization distributions (densities) within the nucleon.

Properties of g_2 and its interpretation beyond the simple QPM have been established by using the OPE technique [147–161]. The expression for g_2 contains two terms: (1) g_2^{WW} from twist-2 and (2) $\bar{g}_2$ from twist-3 contributions:

$$g_2(x, Q^2) = g_2^{\mathrm{WW}}(x, Q^2) + \bar{g}_2(x, Q^2).$$

Wandzura and Wilczek [158] have calculated the twist-2 term from g_1, i. e., from the longitudinal polarization density in the nucleon:

$$g_2^{\mathrm{WW}}(x, Q^2) = -g_1(x, Q^2) + \int\limits_x^1 g_1(t, Q^2)\frac{dt}{t}. \qquad (1.40)$$

The additional twist-2 contribution to g_2 arising from the transverse polarization density in the nucleon is expected to be suppressed by the ratio of the quark to nucleon mass. The analysis of the twist-3 part of the g_2 turns out to be rather complicated (see [160] and references therein).

There are sum rules [7,8] involving the structure function g_2: the Burkhardt–Cottinghem sum rule [159]:

$$\Gamma_2 = \int\limits_0^1 g_2(x, Q^2)dx = 0 \qquad (1.41)$$

and Efremov–Leader–Teryaev sum rule for the valence part of g_1 and g_2 [161]:

$$\Gamma_{\mathrm{ELT}} = \int\limits_0^1 dx\, x[g_1^V(x) + 2g_2^V(x)] = 0. \qquad (1.42)$$

There are the QCD sum rules [7,8] which also should be tested.

Experimentally $g_2(x)$ is measured from DIS asymmetries $A_\perp$ and $A_\parallel$ (see Eqs. (1.9) and (1.12)) and expressed via virtual photon asymmetries A_1 and A_2. From (1.12) it is seen that A_2 is dominated by g_2. The asymmetry A_2, and hence g_2, is bounded by the positivity limit $|A_2| \leqslant \sqrt{R}$ [194] and the more stringent limit $|A_2| \leqslant \sqrt{R(1 + A_1)/2}$ from the recent paper [198].

1.4. The Generalized Gerasimov–Drell–Hearn (GDH) Sum Rule. The GDH sum rule [137] relates the anomalous magnetic moment, k, of the nucleon with the total absorption cross sections of circularly polarized real photons:

$$\int\limits_0^\infty [\sigma_{1/2}(\nu) - \sigma_{3/2}(\nu)]\frac{d\nu}{\nu} = -\frac{2\pi^2\alpha}{M^2}k^2, \qquad (1.43)$$

where α is the electromagnetic constant. With $k_p = 1.79$ and $k_n = -1.91$ the theoretical predictions for the integrals are about -204 and -233 μb for proton and neutron, respectively. The sum rule was derived using very general principles of causality, unitarity, crossing symmetry and Lorentz and gauge invariance. It has never been directly tested, due to the absence of a circularly polarized beam with a wide range of photon energies. There are several predictions for the

contribution of nucleon resonance excitation to the GDH integral [143], derived from multipole analyses of data for unpolarized single-pion photoproduction, and the prediction for the contribution of high energy multihadron production [144], based on a multiple-Reggeon exchange analysis of deep inelastic asymmetries. The estimate from multipole analysis was confirmed by results from the experiments at Mainz [145], which covered the photon energy range from 200 up to 800 MeV, and at Bonn [146] up to 3 GeV.

The integral (1.43) can be generalized [138] to the absorption of virtual photons with energy ν and four-momentum Q^2:

$$
I(Q^2) \equiv \int\limits_{Q^2/2M}^{\infty} [\sigma_{1/2}(\nu, Q^2) - \sigma_{3/2}(\nu, Q^2)]\frac{d\nu}{\nu} =
$$

$$
= \frac{8\pi^2\alpha}{M} \int\limits_{0}^{1} \frac{g_1(x, Q^2) - \gamma^2 g_2(x, Q^2)}{K}\frac{dx}{x}, \quad (1.44)
$$

where $K = \nu\sqrt{1 + \gamma^2}$ is the flux of virtual photons. For $\gamma \ll 1$, the right side of Eq. (1.44) is reduced to

$$
I(Q^2) \approx 16\pi^2\alpha\frac{\Gamma_1(Q^2)}{Q^2}. \quad (1.45)
$$

A strong variation of the integral (1.44) is required in order to connect $\Gamma_1^p(Q^2)$ which is positive, to the GDH prediction for real photons which is negative. So, $I(Q^2)$ must change the sign at low Q^2. Several phenomenological models have been proposed to describe the dependence of the generalized GDH integral on Q^2 [138, 139]. Some of these models predict large effects either from nucleon resonance excitation, or from higher twists (even for Q^2 up to a few GeV^2), or from the structure function g_2.

1.5. Semi-Inclusive and Exclusive DIS. Semi-inclusive and exclusive polarized deep inelastic scattering experiments give additional information on the spin structure of nucleons. Using the correlation between the struck quark and the hadron observed in the final state (flavor tagging) the separate spin contributions of quarks and antiquarks to the spin of nucleon can be determined. Additionally, the gluon polarization can be measured by isolating the photon-gluon fusion process, i. e., by measuring spin asymmetries in charm production or hadron pair production at high transverse momenta. The role of orbital momenta of nucleon constituents is to be determined by studying Deeply Virtual Compton Scattering (DVCS) processes.

1.5.1. Asymmetries in Semi-Inclusive Production of Hadrons. Hadron production in DIS is described as the absorption of a virtual photon by a quark with

its subsequent fragmentation into a hadronic final state. The processes can be characterized by two functions: the quark distribution function $q_f(x, Q^2)$, and the fragmentation function $D_f^h(z, Q^2)$. The semi-inclusive DIS cross section, $\sigma^h(x, Q^2, z)$, to produce a hadron of a type h with the energy fraction $z = E^h/\nu$ is then given by

$$\sigma^h \sim \sum_f e_f^2 q_f(x, Q^2) D_f^h(z, Q^2). \tag{1.46}$$

It is assumed that the fragmentation process is spin-independent, i. e., that the probability to produce a hadron of type h from a quark of flavor f is independent of the relative spin orientations of quark and nucleon. The spin asymmetry A_1^h in the semi-inclusive cross section for production of a hadron of type h by a polarized virtual photon is then given by

$$A_1^h = \frac{\sum_f e_f^2 \Delta q_f(x, Q^2) D_f^h(z, Q^2)}{\sum_f e_f^2 q_f(x, Q^2) D_f^h(z, Q^2)} \frac{1 + R(x, Q^2)}{1 + \gamma^2}, \tag{1.47}$$

where $\Delta q_f(x, Q^2) = q_f^{\uparrow\uparrow}(x, Q^2) - q_f^{\uparrow\downarrow}(x, Q^2)$ is the polarized quark distribution function and $q_f^{\uparrow\uparrow(\uparrow\downarrow)}(x, Q^2)$ is the distribution function of quarks with spin orientation parallel (antiparallel) to the spin of the nucleon. The ratio $R = \sigma_L/\sigma_T$ of the longitudinal to transverse photon absorption cross sections appears in this formula to correct for the longitudinal component that is included in the experimentally determined parameterizations of $q_f(x, Q^2)$ but not in $\Delta q_f(x, Q^2)$.

Using Eq. (1.47) one can extract the polarized quark distribution functions from semi-inclusive asymmetries A_1^h (see [62]):

$$A_1^h = \sum_f P_f^h(x) \frac{\Delta q_f(x)}{q_f(x)} \frac{1 + R(x)}{1 + \gamma^2}, \tag{1.47'}$$

where $P_f^h(x)$ are the so-called «integrated purities» written as

$$P_f^h(x) = \frac{e_f^2 q_f(x) \int D_f^h(z) dz}{\Sigma_{f'} q_{f'}(x) \int D_{f'}^h(z') dz'}.$$

The inclusive asymmetry A_1 is expressed similarly to (1.47') replacing P_f^h by P_f, where $P_f(x) = e_f^2 q_f(x)/\Sigma_{f'} e_{f'}^2 q_{f'}(x)$. Equations (1.47') for A_1^h and similar equations for A_1 can be written in the matrix form

$$\mathbf{A}(x) = P(x)\mathbf{Q}(x), \tag{1.47''}$$

where the vector $\mathbf{A} = (A_{1p}, A_{1p}^{h+}, A_{1p}^{h-}, A_{1n}, A_{1n}^{h+}, A_{1n}^{h-})$ contains the experimentally measured asymmetries as elements. The vector $\mathbf{Q}(x)$ contains the relative

quark and antiquark polarizations,

$$\mathbf{Q} = \left(\frac{\Delta u(x) + \Delta \bar{u}(x)}{u(x) + \bar{u}(x)}, \frac{\Delta d(x) + \Delta \bar{d}(x)}{d(x) + \bar{d}(x)}, \frac{\Delta s(x) + \Delta \bar{s}(x)}{s(x) + \bar{s}(x)} \right).$$

The matrix P contains the integrated purities for the proton and neutron as well as the $(1 + R(x))/(1 + \gamma^2)$ factor. So, these purities describe the probability that the virtual photon hits a quark of the flavor f when a hadron of type h is experimentally detected.

There are the theoretical models [9, 10] relating the spin distributions of the sea flavors. The first model assumes that the polarization $\Delta q_s(x)/q_s(x)$ of sea quarks is independent of a flavor: $\Delta u_s(x)/u_s(x) = \Delta d_s(x)/d_s(x) = \Delta s(x)/s(x) = \Delta \bar{u}(x)/\bar{u}(x) = \Delta \bar{d}(x)/\bar{d}(x) = \Delta \bar{s}(x)/\bar{s}(x)$. As an alternative, the second one assumes that: $\Delta u_s(x) = \Delta d_s(x) = \Delta s(x) = \Delta \bar{u}(x) = \Delta \bar{d}(x) = \Delta \bar{s}(x)$. Due to that the polarizations of the strange quarks and of the total sea are equal:

$$(\Delta s(x) + \Delta \bar{s}(x))/(s(x) + \bar{s}(x)) = \Delta q_s(x)/q_s(x).$$

An alternative to (Eq. (1.47)) the method of the semi-inclusive spin asymmetries, analysis in QPM has been proposed in [28]. The asymmetries A_1^{+-} are determined from the differences of the cross sections from (Eq. (1.46)) for positively and negatively charged hadrons:

$$A_{1p}^{+-} = \frac{(\sigma_{1/2}^+ - \sigma_{1/2}^-) - (\sigma_{3/2}^+ - \sigma_{3/2}^-)}{(\sigma_{1/2}^+ + \sigma_{1/2}^-) + (\sigma_{3/2}^+ + \sigma_{3/2}^-)}, \quad A_{1d}^{+-} = \frac{(\sigma_0^+ - \sigma_0^-) - (\sigma_2^+ - \sigma_2^-)}{(\sigma_0^+ + \sigma_0^-) + (\sigma_2^+ + \sigma_2^-)}.$$

These asymmetries are functions of the valence quark distributions only:

$$A_{1p}^{+-} = \frac{4\Delta u_V - \eta \Delta d_V}{4u_V - \eta d_V}, \quad A_{1d}^{+-} = \frac{\Delta u_V + \Delta d_V}{u_V + d_V},$$

where η is calculated from fragmentation functions. The asymmetry A_{1d}^{+-} does not depend on fragmentation functions, whereas A_{1p}^{+-} is only weakly sensitive to them. The method is further developed in [29]. It has some advantages when assymetries are analyzed in NLO QCD.

1.5.2. Gluon Polarization. As has been shown in Subsec. 1.2.6, from the inclusive polarized DIS data one can determine the contributions of quarks to the nucleon spin. Polarized gluons can also contribute to it. A direct measurement of Δg is planned by COMPASS [191] via the photon-gluon fusion processes (PGF). Experimentally it can be detected via semi-inclusive reactions of charmed particle production or production of jets (hadrons) with high transverse momenta (high-p_T) [11]. The latter reaction [12] is a production of two *high-p_T jets* at high energies requiring the detection of two jets with p_T jet > 5 GeV/c. At the

moderate energies (less than ~ 50 GeV) in fixed target experiments the criteria for identifying jets are not reliable due to their large angular spread and low particle multiplicity.

1.5.3. Longitudinal Spin Transfer to Λ. Additional information on the polarized quark distributions in the nucleon can be obtained from production of Λ hyperons in the polarized DIS [13, 14]. The Λ's which originate from the struck quarks («current fragmentation») measure the spin transfer $D_{LL's}^{\Lambda}$ defined as the fraction of the virtual photon polarization transferred to the Λ. Assuming $SU(3)$ flavor symmetry, the up, down and strange quark distributions and fragmentation functions for the Λ can be related to those in the proton. In the naive quark parton model the Λ polarization is entirely due to the strange quark. Combining $SU(3)$ flavor symmetry with data on hyperon-decays and polarized structure functions, one can estimate the spin transfer in the Λ fragmentation from the up (down) quark. Thus, spin-dependent production of Λ hyperons in the current fragmentation region is a probe of $SU(3)$ flavor symmetry in fragmentation processes.

1.5.4. Generalized Parton Distribution Functions and DVCS. The interest to Deeply Virtual Compton Scattering (DVCS) has been triggered by introduction of the Generalized Parton Distributions (GPD) [112, 113] (see also a review in [116]) formalism, which is believed to be a generalization of the Feynman's parton model and brings new insights into the understanding of the nucleon substructure. As a consequence it appears that DVCS is a reaction providing a completely new way of accessing the spin structure of the nucleon. On the other hand, experimental possibilities for GPD have become available recently from measurements of exclusive DIS reactions including production of real photons.

One of these reactions is: $\gamma^* p \rightarrow \gamma p$, where γ^* is a virtual photon. It is accessed in lepton-nucleon scattering $lp \rightarrow l'p'\gamma$. There are three kinematic variables describing DVCS: $Q^2, s = (p + q)^2 = (p' + q')^2$, the centre of mass energy squared of the photon-nucleon system, and $t = (q - q')^2 = (p - p')^2$, the transfer related to the scattering angle of the virtual photon with respect to the real one. Two other variables complement the description: ε, the polarization of the virtual photon, and ϕ, the angle between the leptonic and hadronic planes.

At leading order in perturbative QCD the DVCS is dominated by a single quark scattering, and therefore the scattering amplitude can be expressed in terms of GPD. The process is described by a hand-bag diagram shown in Fig. 1, d. Nucleon of momentum $p = P - \Delta/2$ emits a quark of momentum $k - \Delta/2$ which absorbs a virtual photon of momentum q. In the deeply-virtual Bjorken limit with large $Q^2 = -q^2$ and ν and finite x the quark which absorbs the virtual photon becomes highly virtual and hence propagates perturbatively. The simplest way to form the final state is for the quark to promptly radiate a real photon of momentum $q' = q - \Delta$ and to fall back to the nucleon ground state of momentum $p' = P + \Delta/2$.

Radyushkin [112] and Ji [113] have shown that the leading order DVCS amplitude can be factorized in (1) a hard scattering part (the upper part of the diagram in Fig. 1, d) which is exactly calculable in perturbative QCD and (2) in a soft nonperturbative part which can be expressed in terms of four GPD's: H_i, $\tilde{H}_i$, E_i, and $\tilde{E}_i$ (i is a parton flavor $i = u, d, s, \ldots, g$). They depend upon three variables: x, ξ, t, where x is the average longitudinal momentum fraction of the active quark coinciding with x-Bjorken in the Bjorken limit, ξ is skewedness or the longitudinal fraction of the transfer Δ, $\Delta = q - q' = p - p'$, and $t = \Delta^2$ is the squared transfer between the virtual and real photons. In the Bjorken limit $2\xi \to x/(1 - x/2)$. The condition of factorization is a small $t, t \leqslant 1$ GeV^2. The light-cone variables are shown in Fig. 1, d in square brackets.

The GPD's H and $\tilde{H}$ conserve the nucleon helicity, while the E and $\tilde{E}$ flip the nucleon helicity. In the limit of $\xi \to 0$ and $t \to 0$, the H and $\tilde{H}$ are reduced to the ordinary parton distributions

$$H(x, 0, 0) = q(x), \quad \tilde{H}(x, 0, 0) = \Delta q(x), \tag{1.48}$$

where $q(x)$ and $\Delta q(x)$ are the unpolarized and polarized quark densities, respectively. Similar equations hold for gluon distributions.

Integrating the GPD over x one gets the following sum rules:

$$\int\limits_{-1}^{1} dx H(x, \xi, t) = F_1(t), \quad \int\limits_{1}^{1} dx E(x, \xi, t) = F_2(t), \tag{1.49}$$

$$\int\limits_{-1}^{1} dx \tilde{H}(x, \xi, t) = G_A(t), \quad \int\limits_{-1}^{1} dx \tilde{E}(x, \xi, t) = G_P(t), \tag{1.50}$$

where F_1 and F_2 are the Dirac and Pauli form factors and G_A and G_P are the axial-vector and pseudo-scalar form factors of nucleons. The interpretation of GPD's follows from these integrals: the GPD represents a partial contribution of quarks with longitudinal momentum fraction x to the corresponding form factors.

The angular momentum operator in QCD is the sum of quark and gluon contributions to it:

$$\mathbf{J}_{\mathrm{QCD}} = \mathbf{J}_q + \mathbf{J}_g, \tag{1.51}$$

where

$$\mathbf{J}_q = \int d^3 x \mathbf{x} \times \mathbf{T}_q, \quad \text{and} \quad \mathbf{J}_g = \int d^3 x \mathbf{x} \times \tilde{T}_g. \tag{1.52}$$

Here $\mathbf{T}_q$ and $\tilde{T}_g$ are the quark and gluon part of the energy-momentum tensor, respectively. Separate quark and gluon contributions to the nucleon spin can

be deduced by an analogy with the magnetic moment if the form factors of the momentum density are known at zero momentum transfer:

$$J_{q,g} = 1/2(A_{q,g}(0) + B_{q,g}(0)), \tag{1.53}$$

where A and B are form factors of the momentum density and $J_q + J_g = 1/2$. The angular momenta of partons in the nucleon are introduced via second moments of GPD yielding:

$$\int_{-1}^{1} dx\, x [H_i(x, \xi, t) + E_i(x, \xi, t)] = A_i(t) + B_i(t), \tag{1.54}$$

where the ξ dependence drops out. The Ji's sum rule states that at $t = 0$ the sum of the integrals (1.54) over the quark flavors gives the total (spin + orbital) angular momentum carried by quarks:

$$\frac{1}{2} \sum_i \int_{-1}^{1} dx\, x \left[H_i(x, \xi, t = 0) + E_i(x, \xi, t = 0)\right] = A_q(0) + B_q(0) = J_q. \tag{1.55}$$

The quark angular momentum decomposes as

$$J_q = \frac{1}{2}\Delta\Sigma + L_q,$$

where $\Delta\Sigma/2$ and L_q are the quark spin and orbital angular momentum, respectively. Similarly one can get J_g.

Balitsky and Ji [117] have estimated the parton contributions to the nucleon spin using a QCD sum rule approach. They found that the spin of the nucleon looks like

$$\frac{1}{2} = 0.1 \left(\text{from } \frac{1}{2}\Delta\Sigma\right) + 0.15\,(\text{from } L_q) + 0.25\,(\text{from } J_g). \tag{1.56}$$

The calculations [118] also confirmed 0.25 for the gluon contribution to the nucleon spin.

In paper [113] Ji has considered different ways to access GPD. One of them is a measurement of the single spin asymmetry A_L in electroproduction of real photons by polarized leptons on unpolarized targets via the DVCS process. The A_L is proportional to

$$A_L \sim -2\frac{e^6}{\Delta^2 q^2} \left(\Delta l^{(\mu\nu)} \operatorname{Im} H_{(\mu\nu)} + \Delta l_{(\mu\nu)} \operatorname{Im} H^{(\mu\nu)}\right), \tag{1.57}$$

where $l_{(\mu\nu)}(H_{(\mu\nu)})$ and $l^{(\mu\nu)}(H^{(\mu\nu)})$ are symmetric and antisymmetric parts of lepton (hadron) tensor, respectively. The full expressions for the relation between GPD and these tensors are given in [113]. From them one can see that the single-spin asymmetry, A_L, includes the interference term between DVCS and Bethe–Heitler (BH) diagrams. The latter represent QED processes of the photon radiation by a lepton before or after scattering.

It is important to see which amplitude can be extracted from measurements of the real photon production with different combinations of the azimuthal angle, ϕ, and beam helicities. The cross section is given by

$$\frac{d^4\sigma}{d\phi\, dt dQ^2 dx} = \frac{1}{32(2\pi^4)} \frac{xy^2}{Q^4} \frac{1}{(1 + 4x^2 M^2/Q^2)^{1/2}} |\tau_{\text{BH}} + \tau_{\text{DVCS}}|^2. \quad (1.58)$$

The squared BH contribution has the structure:

$$|\tau_{\text{BH}}|^2 = f_1(\varepsilon, x, \Delta_T) + \frac{1}{Q} \cos{(\phi)} f_2(\varepsilon, x, \Delta_T) + O(1/Q^2), \quad (1.59)$$

where the functions f_1 and f_2 do not depend on Q^2.

The squared DVCS amplitude is read as follows:

$$|\tau_{\text{DVCS}}|^2 = \frac{e^6}{Q^2} \frac{2}{1-\varepsilon} \sum \left[\frac{1}{2}\{|M_{h,h'}^{1,1}|^2 + |M_{h,h'}^{-1,1}|^2\} + \varepsilon |M_{h,h'}^{0,1}|^2 - \right.$$
$$- \cos{(\phi)}\sqrt{\varepsilon(1+\varepsilon)} \operatorname{Re}\{(M_{h,h'}^{1,1})^* M_{h,h'}^{0,1} - (M_{h,h'}^{-1,1})^* M_{h,h'}^{0,1}\} -$$
$$\left. - \cos{(2\phi)}\varepsilon \operatorname{Re}\{(M_{h,h'}^{1,1})^* M_{h,h'}^{-1,1}\} \right], \quad (1.60)$$

where $M_{h,h'}^{\lambda,\lambda'}$ are helicity amplitudes with λ (λ') being helicity of the initial (final) photon state and h (h') that of the initial (final) proton state.

And finally, the DVCS + BH interference term can be written as

$$\tau_{\text{BH}}^* \tau_{\text{DVCS}} + \tau_{\text{DVCS}}^* \tau_{\text{BH}} = \frac{e^6}{t} \frac{M}{Q} \frac{4\sqrt{2}}{x} \frac{1}{\sqrt{1-x}} \left[\cos{(\phi)} \frac{1}{\sqrt{\varepsilon}(1-\varepsilon)} \operatorname{Re}\tilde{M}^{1,1} - \right.$$
$$- \cos{(2\phi)}\sqrt{\frac{1+\varepsilon}{1-\varepsilon}} \operatorname{Re}\tilde{M}^{0,1} - \cos{(3\phi)}\sqrt{\frac{\varepsilon}{1-\varepsilon}} \operatorname{Re}\tilde{M}^{-1,1} \left] + O(1/Q^2). \quad (1.61) \right.$$

Here the $\gamma^* p \to \gamma p$ helicity amplitudes are linear combinations:

$$\tilde{M}^{\lambda,\lambda'} = \Delta_T[(1-x)G_M - (1-x/2)F_2]M_{-1/2,-1/2}^{\lambda,\lambda'} +$$
$$+ \frac{\Delta_T}{M}[G_M - (1-x/2)F_2]M_{1/2,1/2}^{\lambda,\lambda'} +$$
$$+ \left[x^2 G_M + \frac{\Delta_T^2}{2M^2}F_2\right] M_{1/2,-1/2}^{\lambda,\lambda'} - \frac{\Delta_T^2}{2M^2}F_2 M_{-1/2,1/2}^{\lambda,\lambda'}, \quad (1.62)$$

where G_M and F_2 are magnetic and Pauli form factors of the proton. For small Δ_T we have

$$\Delta_T^2 = (1-x)(t_0 - t) \tag{1.63}$$

and t_0 is a kinematic limit given by

$$t_0 = -M^2 \frac{x^2}{1 - x + xM^2/Q^2}. \tag{1.64}$$

As one can see from above, the hierarchy in powers of Q contributions to the cross section from the BH, BH + DVCS and DVCS is like 1, $1/Q$, and $1/Q^2$, respectively, accompanied with ϕ-dependence proportional to $\cos(n\phi)$ with $n = 0, 1, 2$, and 3.

The DVCS amplitude, τ_{DVCS}, has real and imaginary parts. The last one can be measured from the cross section difference for different beam polarizations:

$$d^4\sigma^+ - d^4\sigma^- \sim \mathrm{Im}\,(\tau_{\mathrm{DVCS}}\tau_{\mathrm{BH}}) \sim A\,\mathrm{Im}\,M^{1,1}\,\sin\phi + B\,\mathrm{Im}\,M^{0,1}\,\sin 2\phi + \dots$$

But experimentally it is simpler to measure the asymmetry

$$A_L = (d^4\sigma^+ - d^4\sigma^-)/(d^4\sigma^+ + d^4\sigma^-)$$

in spite of the more complex ϕ dependence due to the terms in the denominator.

1.5.5. Hadron Azimuthal Distributions and Transverse Spin Asymmetries in DIS. Azimuthal distributions of hadrons (mainly π^+ and π^-) produced in semi-inclusive DIS off transversely polarized targets (proton or deuteron) are sources of new spin observables.

Following Collins [20], the fragmentation function for transversely polarized quarks, D_f^h, contains two terms, a spin-independent term, D_f, and a spin-dependent term, ΔD_f:

$$D_f^h = D_f(z, p_f^h) + \Delta D_f(z, p_f^h)\,\sin\phi_c,$$

where ϕ_c is an azimuthal «Collins» angle (see Fig. 2, c) between outgoing hadron, ϕ, and final quark spin, ϕ_S. It is given by $\phi_c = \phi - \phi_S$. This spin dependence of the fragmentation function leads to specific azimuthal dependence of outgoing leading hadrons:

$$A_h \cong \mathrm{const}\,(1 + A_N\,\sin\phi_c).$$

The amplitude A_N of the azimuthal distribution of hadrons is proportional both to transversity distribution $h(x)$ and analyzing power in the polarized quark fragmentation, a_c:

$$A_N = h(x)a_c(z, p_T).$$

The detailed studies of the transverse spin effects in DIS are planned by HERMES and COMPASS [191].

2. THE FIRST MEASUREMENTS OF $g_1^p(x)$

The first measurements of the spin-dependent asymmetry $A_1^p(x)$ and structure function $g_1^p(x)$ of the proton have been performed in 1978–1983 by the SLAC experiments E80 and E130 [31, 32]. Due to the electron beam energy, 18 GeV at that time, and geometrical conditions of the apparatus, the asymmetries of cross sections for longitudinally polarized electrons and protons were obtained in the region $x = 0.1$–0.7 and $Q^2 < 10$ GeV^2. During the analysis the data were averaged over Q^2 range of the measurement with $\langle Q^2 \rangle = 2$ GeV^2 and presented as a function of x. No surprises were observed in that region: as it had been expected, $A_1^p(x)$ was monotonous increasing with rising x with a tendency to approach a unity at $x = 1$. The results and techniques of these experiments were reviewed by V. Hughes and J. Kuti [34].

Five years later, the SLAC measurements were updated by the EMC [33] at CERN using a high energy muon beam M2. This beam can supply longitudinally polarized muons in the energy region up to 200 GeV. Due to that and also due to the spectrometer acceptance optimized in the forward direction, EMC was able to extend the kinematic region of DIS measurements in x and Q^2: $x = 0.01$–0.7 and $Q^2 < 50$ GeV^2. In the logarithmic scale the region in x was extended by one order of magnitude compared to the SLAC region. As one can see, this was very important for the interpretation of the experimental results. The EMC data averaged over Q^2 range of measurements with $\langle Q^2 \rangle = 11$ GeV^2 are shown in Fig. 3. These figures show that the EMC and SLAC data are compatible in the overlapping x regions. Although they belong to different average Q^2 (11 and 2 GeV^2, respectively) the results do not seem to be sensitive to the Q^2 change between these values.

New features of the EMC data are seen at small x inaccessible at SLAC. There is a clear tendency of $A_1^p(x)$ to approach zero at $x \to 0$ (Fig. 3, a) and flattening of $g_1^p(x)$ in the same region (Fig. 3, b). These features are reflected on the dependence of the integral $\Gamma_1^p(x)$ on x: the contribution of the small x region to $\Gamma_1^p(x)$ becomes less and less while x approaching zero (Fig. 3, c). This could not be seen with SLAC data only. The integral Γ_1^p calculated by the EMC in the whole x region was found to be

$$\Gamma_1^p = 0.126 \pm 0.018, \tag{2.1}$$

where the error represents combined statistical and systematic uncertainties. The value of Γ_1^p is about three standard deviations away from the Ellis–Jaffe prediction at the same Q^2: 0.189 ± 0.009.

The difference between the experimental and theoretical values of Γ_1^p is clearly seen in Fig. 3.
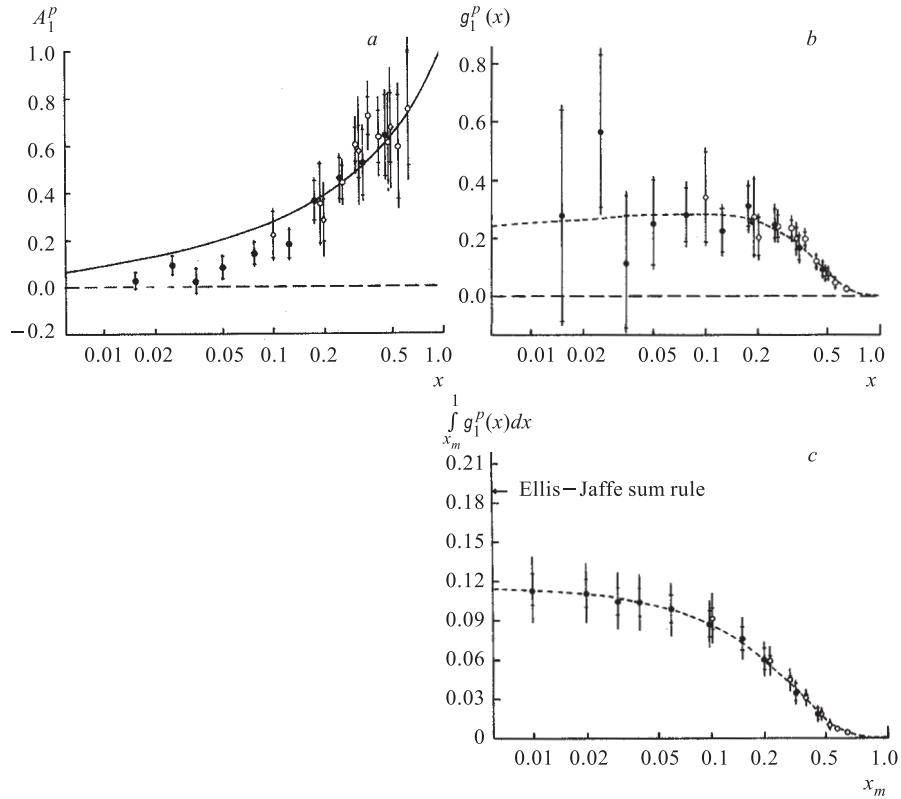
Fig. 3. The asymmetry $A_1^p(x)$ (a), structure function $g_1^p(x)$ (b) and integral $\Gamma_1^p(x)$ (c) measured by the SLAC E80, E130 (open symbols) and EMC (closed symbols) experiments

Using the technique described in Subsec. 1.2.6, the EMC has related the result (2.1) to the quark contributions to the proton spin and found that

$$\Delta\Sigma = 0.12 \pm 0.1 \quad \text{and} \quad \Delta s = -0.06 \pm 0.1, \tag{2.2}$$

contrary to Ellis–Jaffe predictions

$$\Delta\Sigma_{\text{EJ}} \cong 0.6 \quad \text{and} \quad \Delta s_{\text{EJ}} = 0.$$

This means that quarks contribute little to the proton spin and strange sea quarks are polarized. The surprising EMC results created a kind of crisis in understanding of the proton spin and triggered a lot of theoretical papers trying to explain it. New experiments have been proposed in 1989–1993 at CERN, SLAC, and DESY.

3. FURTHER MEASUREMENTS OF SPIN-DEPENDENT
STRUCTURE FUNCTIONS

Further measurements of spin-dependent structure functions were proposed and performed by the

— Spin Muon Collaboration (SMC) at CERN using the muon beam M2 at 100 and 200 GeV;

— SLAC collaborations (experiments E142 and E143) using the electron beam at 23–26 GeV later on updated by experiments E154 and E155 at 50 GeV;

— HERMES collaboration at DESY using the positron or electron beam at 27.5 GeV.

The goals of these experiments were:

— to prove (disprove) the EMC results on g_1^p with a better accuracy;

— to measure the structure function $g_1^{d,n}$ of the deuteron and neutron;

— to test the Ellis–Jaffe sum rules for the proton and neutron;

— to test the Bjorken sum rule for the first time;

— to measure the structure function g_2 of the proton and deuteron for the first time;

— to study spin-dependent effects in semi-inclusive DIS reactions.

The data of these experiments will be reviewed in Sec. 4 and 5. Here we consider the details of the experimental set-ups to understand better the data and their limitations.

3.1. Experiment SMC. This experiment was designed to measure cross section asymmetries for inclusive and semi-inclusive scattering of longitudinally polarized muons from longitudinally and transversely polarized protons and deuterons. Ideally for this purpose one needs to know:

— a trajectory, momentum and polarization, P_μ, of incident muons;

— polarization of protons (deuterons), P_t, and

— angle of scattering (θ) and momentum of scattered muons (p').

All these characteristics, except P_μ and P_t, are determined in the SMC experiment for each detected event. P_μ and P_t are determined on the average for some data samples.

The main features of the SMC experiment are:

— the polarized muon beam;

— the world largest polarized target in which protons or deuterons can be polarized longitudinally or transversely;

— the high resolution spectrometer to measure momentum and angle of a scattered muon;

— two types of polarimeters to measure the beam polarization.

3.1.1. CERN Polarized Muon Beam. The muon beam M2 at CERN SPS is a complicated physics engineering complex. The protons are accelerated in the SPS up to 450 GeV, extracted from the accelerator in the direction of the North experimental area and brought on the berillium (Be) target.

Secondary particles produced in the target, mainly pions and kaons, are momentum selected and directed into about 600 m long decay channel which has a distributed system of FODO (Focus-Ou-Defocus-Ou) quadrupoles optimizing the intensities of particles. Few percent of pions and kaons decay mainly via two particle decays:

$$\pi, K \rightarrow \mu\nu.$$

The remaining hadrons at the end of the decay channel are absorbed in the 9.9 m long Be absorber placed inside a sweeping magnet. Muons passed through the absorber are additionally focused with FODO quadrupoles then momentum selected and transported to the experimental hall. All elements forming the muon beam are placed in the inclined tunnel bringing the beam from the underground target area to the surface experimental hall.

The muon momentum is measured by means of the so-called Beam Momentum Station (BMS). It consists of the deflecting magnet B6 (see Fig. 4 *a*), quadrupoles (Q) and four planes of scintillating hodoscopes (H1–4) measuring the muon track before and after the magnet for each event detected by the spectrometer. The resolution of the momentum measurement was better than 0.5 %. It is defined by granularities of the hodoscopes and deflecting power of B6.

The beam phase space is defined by a set of collimators, FODO quadrupoles, scrapers and absorbers installed along the beam line.

In addition to that at the end of the beam line there is a Beam Definition Station (BDS) which defines the beam spot on the polarized target with the set of veto counters V1,2 and shields the spectrometer against halo muons accompanying the beam with the help of the absorber and large veto counter V3 (Fig. 4, *b*).

The beam spot on the target was approximately circular with r. m. s. radius 1.6 cm and r. m. s. width in momentum of about 2.5 %. The beam intensity depends on the momentum. But due to time resolutions of the detectors used in the SMC spectrometer, the intensity was limited to $4 \cdot 10^7$ muons per SPS pulse which was 2.4 s long with a repetition period of 14.4 s.

The beam is naturally polarized due to the properties of weak decays of pions and kaons. It is seen from the following schemes, representing the two-particle decay of the pion (or kaon) in the pion centre-of-mass system (c. m. s.) in extreme cases when muon is emitted in the forward (*a*) or backward (*b*) directions:
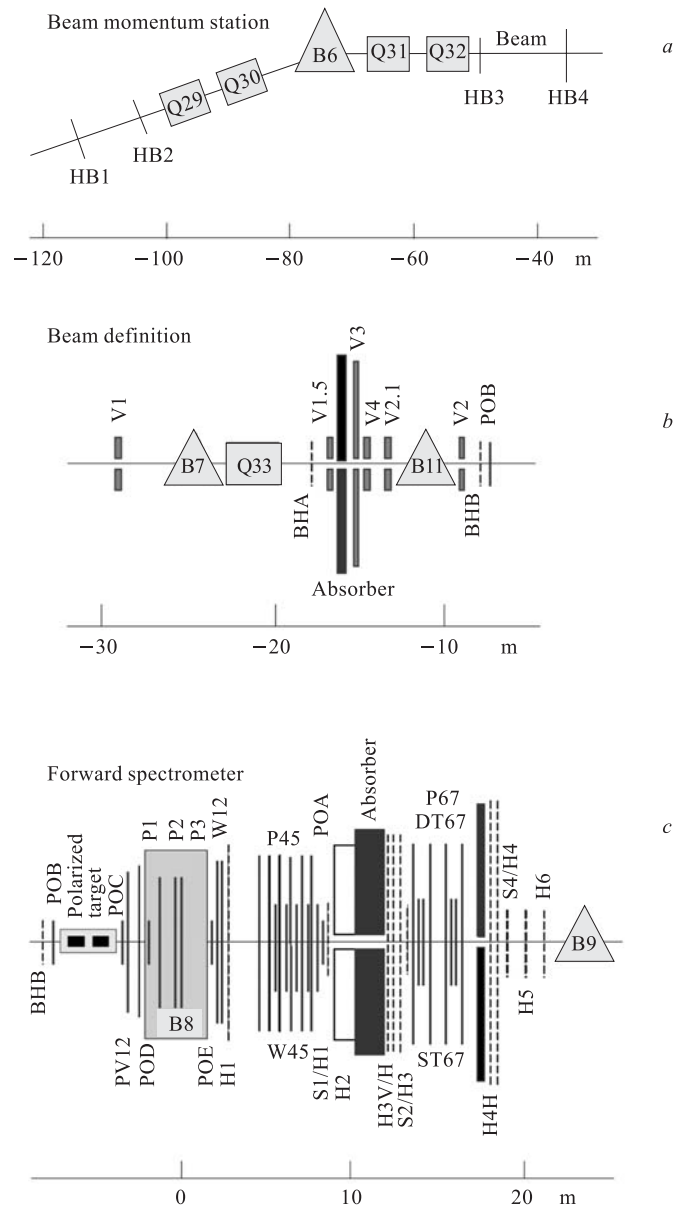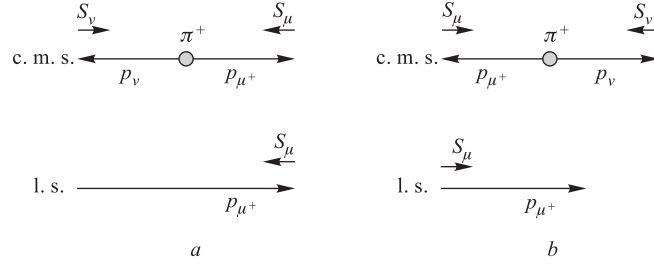
Fig. 4. The scheme of the Beam Momentum Station and the Beam Definition Station at the end of the CERN muon beam M2 and the SMC spectrometer

$$
\begin{array}{cc}
\text{c. m. s.} \quad \xrightarrow{S_\nu} \quad \pi^+ \quad \xleftarrow{S_\mu} & \text{c. m. s.} \quad \xrightarrow{S_\mu} \quad \pi^+ \quad \xleftarrow{S_\nu} \\
p_\nu \qquad p_{\mu^+} & p_{\mu^+} \qquad p_\nu \\[1em]
\text{l. s.} \quad \xleftarrow{S_\mu} \atop p_{\mu^+} & \text{l. s.} \quad \xrightarrow{S_\mu} \atop p_{\mu^+} \\[1em]
a & b
\end{array}
$$

Let us consider the case a. Due to the total angular momentum conservation the spins of neutrino and muon have to be oriented in opposite directions because the spin of pion is zero. But it is known that neutrino is a left-handed particle and its spin is always opposite to its momentum. Hence the muon spin also must be opposite to the muon momentum. If we transform this case to the laboratory (l. s.) system, muon will have a maximum possible energy and its spin will be oriented along the momentum (longitudinally) in opposite (negative) direction. Similar considerations have shown that in case b muon will have a minimal possible momentum and its spin will be in the same (positive) direction. The generalization of these examples is straightforward. If we select positive muons whose momenta are close to the maximum possible ones, these muons will be longitudinally and negatively polarized. For the monochromatic hadron and muon beams, the polarization P_μ is a function of the ratio of muon and hadron energies [162–165]:

$$
P_{\mu+(\mu-)} = -(+)\frac{m_{\pi,K}^2 + \left(1 - \dfrac{2E_{\pi,K}}{E_\mu}\right)m_\mu^2}{m_{\pi,K}^2 - m_\mu^2}. \tag{3.1}
$$

In practice neither of the beams is monochromatic, polarization is smeared and its value can be calculated using Monte Carlo simulations or/and determined experimentally. Although, in principle, one can vary (reverse) the polarization of the beam, it was not reversed during the SMC experiment and was always negative.

3.1.2. The SMC Polarized Target. The SMC has built the world largest polarized target. It contains two target cells in which target material can be polarized in opposite directions. The large length of the target provides the high statistic accuracy of measurements while simultaneous measurements of cross sections for oppositely polarized material and frequent reverse of these polarizations provides minimal systematic errors of measurements.

The detailed description of the target is given elsewhere [166–176,178]. Briefly, the target material can be polarized using the method of the dynamic nuclear polarization [179]. This method requires a strong magnetic field, low

temperature and special microwave technique. Target cells, each 60 cm long, separated by a 30 cm gap were placed inside the superconducting magnet system.

The target materials were either butanol (normal — C_4H_9OH or deuterated — C_4D_9OD) plus 5 % of the water doped with paramagnetic EHBA-Cr(V) molecules, or ammonia (normal $^{14}NH_3$).

The magnet system includes a superconducting solenoid magnet with the longitudinal field of 2.5 T, a dipole magnet with a perpendicular «holding» field of 0.5 T and trim coils to correct relative homogeneity of the field over the volume.

The low temperature bath for the target cells is provided by the ^{3}He–^{4}He dilution refrigerator (DR), which can cool the target materials to the temperature below 0.5 K.

The polarization of the material is obtained approximately as follows. The DR cools the material to the temperature below 0.5 K. At this temperature and in the 2.5 T field, free electron spins are nearly 100 % polarized. At this moment the microwave generator (MW), whose frequency is adjusted to a value of about 70 GHz (electron Larmor frequency), is turned on and spins of electrons are transferred to the nuclear spins. For materials similar to those used in the SMC target, in which the solid-state effects dominate in the polarization mechanism, the degree of polarization can be substantially enhanced by frequency modulation (FM) of the microwaves. For example, the polarization of the deuterated butanol has been enhanced with FM by a factor of 1.7 [175]. Once a high nuclear spin polarization is reached, MW is turned off and the target material is cooled down to about 50 mK. At this temperature «frozen spin» conditions are fulfilled and polarization is preserved during a long period of time and periodically (every five hours) reversed by rotating the superimposed solenoid and dipole fields.

The polarization was measured every minute while data taking by means of five Nuclear Magnetic Resonance (NMR) coils placed along each target cell. The highest values of polarization achieved with the SMC target were 0.93 with hydrogen and 0.61 with deuterium. The average polarizations while data taking were 0.86 ± 0.03 and 0.50 ± 0.03 for hydrogen and deuterium, respectively.

3.1.3. The SMC Spectrometer. The SMC spectrometer (Fig. 4, *c*) is similar to the one used previously by the EMC [180] and NMC. Logically it consists of detectors tracking the incident and scattered muons and detectors providing triggers. The incident muon trajectory is determined by scintillator hodoscopes BHA and BHB and multiwire proportional chambers (MWPC) POB. The momentum and angle of scattered muons are measured with the large aperture dipole magnet (B8) and a system of more than 100 planes of gas detectors:

— in front of the magnet: multiwire proportional chambers POC, PV12 and POD;

— inside the magnet: multiwire proportional chambers P1, P2 and P3;

— between the magnet and hadron absorber: multiwire proportional chambers POE, P45, and POA and drift chambers W45;

— behind the absorber: multiwire proportional chambers P67, a drift tube system DT67 and a streamer tube system ST67 [177].

The fastest gas detectors — MWPC — were placed in the central region, close to the beam where the intensity load is higher.

The spectrometer was triggered by coincidence of hits in scintillating hodoscopes. Three physics triggers provided the data collection in different but overlapping x, Q^2 regions:

— the large-angle trigger T1 organized with hodoscopes H1, H3, and H4 had a good acceptance at θ above 20 mrad;

— the small-angle trigger T2 used the small hodoscopes S1/H1, S2/H3, and S4/H4 and covered angles of scattering in the range $5 \leqslant \theta \leqslant 15$ mrad and

— the smallest-angle trigger T14 covered the scattering angles between 3 and 10 mrad.

The trigger rates per SPS spill were about 200 for T1, 50 for T2 and 100 for T14.

3.1.4. The SMC Polarimeters. Two polarimeters downstream of the spectrometer allowed one to perform measurements of the beam polarization while data taking.

The first polarimeter was measuring the energy spectrum of positrons from muons decaying in flight: $\mu^+ \rightarrow e^+ \bar{\nu}_\mu \nu_e$.

The form of this spectrum depends on muon polarization:

$$\frac{dN}{dy_e} = N_0 \left[\frac{5}{3} - 3y_e^2 + \frac{4}{3}y_e^3 - P_\mu \left(\frac{1}{3} - 3y_e^2 + \frac{8}{3}y_e^3 \right) \right], \tag{3.2}$$

where N_0 is a number of decays and $y_e = E_e/E_\mu$.

Muons decayed in the vacuum pipes 30 m long and positrons were detected with MWPC in front and behind the analyzing magnet and their energy was measured by the lead glass calorimeter. A shower veto detector consisting of Pb foils and scintillating hodoscopes were placed in front of the vacuum pipes to eliminate positrons originating earlier.

The measured positron spectrum was corrected for the detector acceptance and resolution. The polarization of muons, $P_\mu \pm \Delta P_\mu$, was determined fitting the measured spectrum with the expected shape (3.2). The error, except the statistical one, includes the systematic uncertainties, main contributions to them came from the detector acceptance and resolution and from the background rejection.

The second polarimeter was used to measure the asymmetry in the cross sections of the elastic scattering of longitudinally polarized muons on longitudinally polarized electrons [174]:

$$\frac{d\sigma}{dy_{\mu e}} = \frac{2\pi r_e^2 m_e}{E_\mu} \left(\frac{1}{y_{\mu e}^2} - \frac{1}{y_{\mu e} Y} + \frac{1}{2} \right) (1 + P_e P_\mu A_{\mu e}), \qquad (3.3)$$

where $y_{\mu e} = 1 - E'_\mu / E_\mu$; $Y = (1 + m_\mu^2 / 2 m_e E_\mu)^{-1}$ and $A_{\mu e}$ is the asymmetry of cross sections with antiparallel ($\uparrow\downarrow$) and parallel ($\uparrow\uparrow$) orientations of the muon and electron spins:

$$A_{\mu e} = \frac{\sigma^{\uparrow\downarrow} - \sigma^{\uparrow\uparrow}}{\sigma^{\uparrow\downarrow} + \sigma^{\uparrow\uparrow}} = y_{\mu e} \frac{1 - y_{\mu e}/Y + y_{\mu e}/2}{1 - y_{\mu e}/Y + y_{\mu e}^2/2}. \qquad (3.4)$$

The measured asymmetry, A_{mes}, is related to $A_{\mu e}$ by expression

$$A_{\mathrm{mes}}(y) = P_e P_\mu A_{\mu e}(y), \qquad (3.5)$$

from which one can find P_μ.

The polarized electron target — a 2.7 mm thick foil of a ferromagnetic aloy (49 % Fe + 49 % Co + 2 % V) — was installed in the 2.3 T magnetic field. Reversing this field one can change the orientation of the electron polarization. The value of the polarization P_e was determined from measurements of the magnetomechanical ratio of the foil material.

Trajectories of incident muons were reconstructed with scintillating hodoscopes and MWPC. Scattered muons were traced with MWPC before and after the magnet and identified with hodoscopes behind the absorber. Scattered electrons were detected by the same detectors as positrons from μ^+ decays.

Measuring the polarization of the muon beam, the SMC in fact performed two additional experiments simultaneously with data taking. The values of the polarizations determined by two methods were consistent within the errors and equal to $P_\mu = -0.810 \pm 0.013 \pm 0.026$ from μ decays and $P_\mu = -0.784 \pm 0.026 \pm 0.012$ from $\mu - e$ scattering.

3.1.5. Data Taking. Table 1 summarizes the SMC data taking from 1991 to 1996. Each year the data were collected during about 200 days mostly at the μ^+ energy of 190 GeV using either the proton or deuterium polarized target. At the beginning of data taking the target material was butanol replaced in 1996 by ammonia. The kinematic range, event numbers, beam and target polarizations are given in Table 1 as reported in SMC publications [35–47].

3.2. Experiment HERMES. The HERMES experiment (HERA Measurement of Spin) [181] was designed to study DIS of longitudinally polarized electrons (positrons) from polarized (unpolarized) hydrogen, deuterium and ^{3}He and other gas targets.

Table 1. **SMC data taking**

	1991–1992	1993		1994	1995		1996
Running time, days	200	200	17	200	150	50	200
E Beam, GeV*	100	190	100	190	190	190	190
x	0.006–0.6	0.003–0.7	0.006–0.6	0.003–0.7	0.0008–0.7	0.0015–0.6	0.003–0.7
Q^2, GeV^2	1.5–30	1–60	1.5–30	1–60	0.2–100	0.8–18	1–100
Events	$3.2 \cdot 10^6$	$4.4 \cdot 10^6$	$8.7 \cdot 10^5$	$6 \cdot 10^6$	$11.2 \cdot 10^6$	$2 \cdot 10^6$	$9.6 \cdot 10^6$
P_μ	-0.82 ± 0.06	-0.8	-0.82 ± 0.06	-0.81	-0.77 ± 0.04	-0.77 ± 0.04	-0.77 ± 0.03
P_T	0.35 ± 0.02	0.86 ± 0.03	0.80 ± 0.04	0.50 ± 0.02	0.50 ± 0.02	0.43 ± 0.02	0.89 ± 0.03
Polarized Target	D**	P***	P***	D***	D***	D***	P****
Measured Asymmetry	$A_\parallel^d$	$A_\parallel^p$	$A_\perp^p$	$A_\parallel^d$	$A_\parallel^d$	$A_\perp^d$	$A_\parallel^p$

*Beam intensity — $4 \cdot 10^7$ muons per spill of 2.4 s.

**Butanol, 2×40 cm.

***Butanol, 2×60 cm.

****Ammonia.

HERA is a collider at the Deutsches Elektronen-Synchrotron (DESY) Laboratory, Hamburg, Germany. It provides collisions between electrons (positrons) and protons which are injected, accelerated up to 27 and 820 GeV, respectively, and stored in the intersecting storage rings. Two intersection regions of HERA are occupied by large experiments ZEUS and H1. The HERMES experiment is located in the East experimental hall and uses the electron (positron) ring only. The stored electrons (positrons) are arranged in 210 bunches, 96 ns apart, and each bunch contains $3.8 \cdot 10^{10}$ electrons, the bunch length is 27 ps and the average current is 30 mA.

The main features of the HERMES experiment are:

— the polarized high intensity electron (positron) beam from the storage ring of HERA;

— the polarized internal gas target with a storage cell;

— the spectrometer with a good secondary particle identification (PID) system.

The capabilities of HERMES enable the following spin studies[*]:

— precise measurements of structure functions $g_1(x)$ and $g_2(x)$ of the proton and neutron and precision tests of the Bjorken, Ellis–Jaffe and Burkhardt–Cottingham sum rules;

— studies of various Semi-Inclusive DIS (SIDIS) asymmetries;

— measurements of structure functions associated with transverse spin distributions in the nucleon;

— measurements for the first time of new structure functions $b_1(x)$ and $\Delta(x)$ associated with tensor spin variables.

The HERMES takes inclusive data with qualitatively different and smaller than in other experiments systematic uncertainties to improve the world data set for the x dependence of the spin-dependent structure function $g_1(x)$ for both the proton and the neutron. HERMES also provides new precision data on semi-inclusive processes by virtue of the good acceptance of the spectrometer combined with hadron identification and the purity of the targets.

The HERMES experiment has been fully approved at DESY in 1993 and started to take data in 1995. The HERMES progress has been recently reviewed in [66].

3.2.1. The HERA Polarized Electron (Positron) Beam. Electrons (positrons) in the storage ring become transversely polarized due to the Sokolov–Ternov effect [182] in synchrotron radiation. The formulae for electron (positron) synchrotron radiation contain a small asymmetric spin-flip amplitude that enhance the beam polarization state antiparallel (parallel) to the magnetic fields of the storage ring bending magnets. This transverse polarization state is increased exponentially

---

[*]The unpolarized programme of HERMES is not considered here.

in time

$$P(t) = P_{\mathrm{ST}}(1 - \mathrm{e}^{-t/\tau}),$$

where P_{ST} is the asymptotic polarization and $\tau = \dfrac{8m_e\rho^3}{5\sqrt{3}r_e\hbar\gamma^5c^2}$ is a characteristic time, where r_e is the classical electron radius; ρ is the bending radius of the magnetic field and $\gamma = E/m_e$. Due to various depolarization mechanisms, the asymptotic degree of polarization is limited to about 70 %.

The Sokolov–Ternov effect produces the transverse polarization of the beam. As the HERMES experiment requires longitudinal polarization, spin rotators are used to rotate the spin in the longitudinal direction in front of the experiment and back to the transverse direction behind the experimental set-up. The polarization is continuously measured using Compton back-scattering of circularly polarized laser light. Two polarimeters are used. The first one is measuring the transverse polarization in the HERA West straight section and the second one is measuring the longitudinal polarization near the HERMES. The data on transverse and longitudinal polarizations, obtained from a set of rise-time calibration runs taken to compare the performance of two polarimeters are in agreement within better than 1 %. Both polarimeters measure the beam polarization with the statistical accuracy of about 2 % and systematical error of about 5 %. Experimental data on DIS were analyzed only when polarization was above 40 %. The average polarization for analyzed data was 55 %. The beam polarization was not reversed during the measurements. It was always negative (positive) for positrons (electrons).

3.2.2. The HERMES Polarized Internal Gas Target. The target material of the SMC polarized target was butanol or ammonia in which the hydrogen (deuterium) atoms are polarized only whereas the other nuclei stay mainly unpolarized and create a physics background for polarized processes. The low percentage of the hydrogen (deuterium) atoms in the target material (low dilution factor) and admixture of other nuclei introduce systematic uncertainties which could be eliminated in case of pure (monoatomic) targets. Such targets are realized by HERMES using pure gases like H, D, ^{3}He and others.

The HERMES polarized target consists of a source of polarized atoms, a storage cell increasing the target density, the solenoidal magnetic field holding the polarization and a polarimeter measuring the degree of the atom polarization. The holding field is provided by a superconducting magnet defining the direction of the polarization and reducing depolarization effects.

The source of polarized hydrogen or deuterium atoms is based on the Stern–Gerlach separation of atomic spin states. It supplies the atomic beam with an intensity of $6 \cdot 10^{16}$ atoms/s and longitudinal (transverse) polarization better than 90 %. The sign of the polarization can be reversed within milliseconds.

The source of polarized ^{3}He atoms is based on the principle of production of meta-stable exchange between $^3S_1$ and $^3P_0$ states obtained by using the polarized laser light. The intensity of this source is $\sim 2 \cdot 10^{17}$ atoms/s with polarization of about 60 %.

A free gas jet that crosses the stored electron (positron) beam gives the target density which is too low for studies of the electromagnetic interactions with good precision. The storage cell technique increases the target density and corresponding statistics by about two orders of magnitude compared to a free gas jet. The cell basically is a T-shaped 400 mm long open-ended tube in which polarized gas atoms are injected from the source. Atoms perform several hundred wall bounces before they leave the cell via one of openings and pumped out. Thus the probability of the stored beam to collide with atoms is increased. It can be optimized varying the length of the tube, its cross section and temperature. For example, the target density of $3.5 \cdot 10^{14}$ and $7 \cdot 10^{13}$ atoms/cm^2 can be obtained for ^{3}He and hydrogen, respectively, at the cell temperature of 20 K. Note, the storage cell has no walls in the beam direction. Scattered particles exit the target through a 0.3 mm thick stainless steel window.

The polarization and atomic and molecular content of the gas in the cell are measured by pumping a fraction of the gas into a polarimeter of the Breit–Rabi type and into the gas analyzer, respectively. The precision of this polarimeter is about 3 %. The average value of the target polarization was 0.46 ± 0.02 for ^{3}He [56] and 0.88 ± 0.04 for ^{1}H [57]. The target polarization was reversed randomly approximately every one or ten minutes during operations with hydrogen or helium, respectively.

3.2.3. The HERMES Spectrometer. The layout of the HERMES spectrometer [183] is shown in Fig. 5. It contains tracking detectors in front of, inside and behind the 1.3 Tm magnet, PID detectors behind the magnet and trigger hodoscopes.

The tracking detectors include the microstrip gas counters and the mini-drift vertex chambers close to the target, the drift chambers and the proportional chambers.

The PID detectors are the gas Cherenkov counters (replaced later by RICH), Transition Radiation Detectors (TRD), Preshower counters and Lead Glass Electromagnetic Calorimeter. Hadrons and electrons (positrons) are separated in each detector with a certain probability. Typically the lead glass calorimeter and preshower separate electrons and pions to 4000 : 1. TRD improves this ratio by a factor of 100. Cherenkov counters separate pions and kaons in the momentum range below 15.8 GeV. A special likelihood method combined the PID detectors information for the final separation of hadrons and electrons (positrons). Using the tracking and PID information one can identify the produced secondary particles like $K_s^0, \Lambda^0, \rho, \omega, \ldots$ and study the corresponding semi-inclusive reactions.
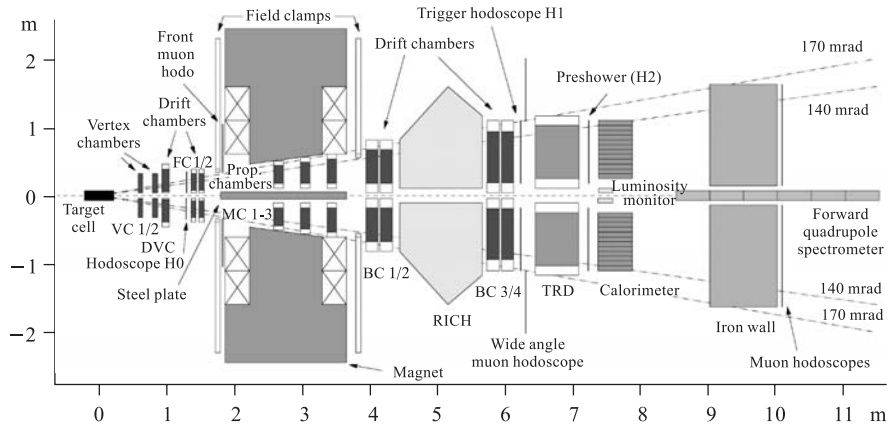
Fig. 5. A scheme of the HERMES spectrometer (side view)

The spectrometer has two parts above and below the beam pipe of the electron (positron) storage ring. The acceptance is limited at small angles by an iron plate which shields the positron (electron) and proton beams from the magnetic field of the spectrometer magnet. Particles with scattering angles within ± 170 mrad in the horizontal direction and between ± 40 and ± 140 mrad in the vertical direction are accepted. The average angular resolution for reconstructed tracks is better than 1 mrad. The momentum resolution is 0.7–1.25 % over the kinematic range of the experiment, while the uncertainty in the scattering angle is below 0.6 mrad everywhere.   The x resolution varies from 4 to 8 % while the Q^2 resolution is better than 2 % over the kinematic range ($0.021 < x < 0.85$ and $0.8 < Q^2 < 20$ GeV^2).

3.3. SLAC Polarized Experiments. SLAC spin physics experiments E142, E143, E154, and E155 have used the polarized high intensity electron beam from SLAC and essentially common spectrometers to identify and measure momenta and energies of DIS electrons at fixed scattering angles. The main characteristics of the beam and spectrometers are given below as well as peculiarities of each experiment. The experiments E154 and E155 have profited the SLAC energy upgrade up to 50 GeV.

3.3.1. The SLAC Polarized Electron Beam. The SLAC polarized electrons [184] were produced by illuminating either the unstrained or strained AlGaAs photocathode with circularly polarized laser light operating at the wavelength of 715 nm. The electron helicity is changed randomly pulse by pulse changing the circular polarization of the excitation light. With the unstrained cathode the polarized source produced an electron beam polarization of about 36 %. The strained photocathode has effectively doubled the beam polarization.

The SLAC has operated with pulses of approximately 1 μs duration at the rate of 120 Hz and intensity $2 \cdot 10^{11}$ e/pulse.

Electrons produced by the source are accelerated in the linear accelerator and then deflected in a beam transport line through an angle 24.5° onto the polarized target. Because of its anomalous magnetic moment, the spin of the electron precesses by an angle $\Delta\Phi$ larger than that of the bend angle of the beam, according to the formula:

$$\Delta\Phi = \pi \left(\frac{24.5°}{180°}\right) \left(\frac{g-2}{2}\right) \left(\frac{E}{m_e}\right) = \left(\frac{E}{3.237}\right) \pi,$$

where g is the gyromagnetic ratio. When $\Delta\Phi$ is an integral multiple of π, the electron spin is longitudinal at the target.

The experiment E142 collected data with longitudinally polarized electrons at three discrete energies of 19.42, 22.66, and 25.51 GeV corresponding to the precession angle $\Delta\Phi = 6\pi$, 7π, and 8π. The beam spot size at the target was typically 2 to 4 mm. The beam polarization was determined measuring the cross section for spin dependent elastic electron-electron scattering (Moeller polarimeter). This is a QED process with a large cross section and analyzing power. The expected cross-section asymmetry can be calculated with high precision and is not significantly modified by radiative processes [186]. The resulting longitudinal beam polarization was $P_B = (0.357 \pm 0.001 \pm 0.011) \cos[\pi E \,(\text{GeV})/3.237]$ with a dominating systematic error of about 3 %. To reduce the systematic errors of DIS measurement, the beam polarization was randomly reversed between the accelerator pulses.

The E143 experiment has used longitudinally polarized electrons with energies of 29.13, 16.18 and 9.71 GeV corresponding to $\Delta\Phi = 9\pi$, 5π, and 3π. The beam polarization was measured to be typically 0.85 ± 0.02.

The experiments E154 and E155 have used the electron beam with the energy of 48.3 GeV and pulses of 250 and 400 ns, respectively. The beam polarization was measured to be 0.82 ± 0.02 over the duration of the experiments.

The position of the beam at the target was monitored during the experiments using two devices, one of which is a travelling-wave radio-frequency beam position monitor placed just in front of the target, and the other is a secondary emission foil array with 1 mm spacing located 10.8 m downstream from the target. The former provided a direct measurement of beam centroid position and was used in an automatic feedback system to keep the beam on target. To minimize the effects such as target depolarization from local beam heating and radiation damage, the beam was moved or «rastered» across the face of the target.

3.3.2. The SLAC DIS Spectrometers. Electrons scattered from the polarized target were detected in two single-arm spectrometers schematically shown in Fig. 6. Each spectrometer was instrumented with two dipole magnets bending particles in opposite directions in a vertical plane, a pair of gas threshold Cherenkov

counters, a segmented lead-glass calorimeter, six planes of segmented scintillation counters grouped into two hodoscopes and two planes of lucite shower trigger counters. Each experiment has used a slightly different magnet setting to accommodate the corresponding scattered momenta range. Parameters of the hodoscopes are also varied depending on counting rates.

The scattered electrons were distinguished from the large pion background using a pair of Cherenkov counters in coincidence. The energies of electrons were measured by two methods — using the track information from the hodoscopes and measuring the energy deposited in the lead-glass calorimeter.

The main electron trigger for each spectrometer consisted of a triple coincidence between the two Cherenkov counters and the sum of the shower counter signals. Up to four triggers were allowed per spectrometer per beam spill. There was a 30 ns dead time after each trigger. The highest rates occurred in the $4.5°$ spectrometer ranging from 1.5 to 2.5 triggers per pulse on the average. The trigger rate in $7°$ spectrometer was typically less than 1 per pulse.

In the E142 and E143 experiments the spectrometers were centered at 4.5 and $7°$ with respect to the beam line in order to maximize the kinematic coverage for the certain electron beam energy and at event selection criteria of $Q^2 > 1.1$ GeV^2. The momentum acceptance ranged from 7 to 20 GeV/c for both the arms. The
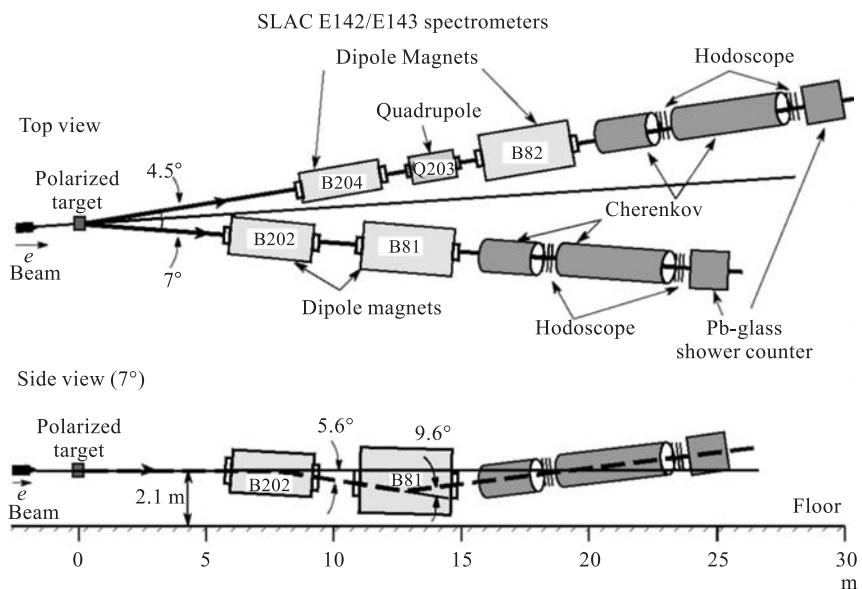

Fig. 6. Layout of the 4.5 and $7°$ spectrometers used in the E142 and E143 experiments

momentum resolutions varied from 0.3 to 3.2 % and from 0.6 to 3.8 % in the 4.5 and 7 ° spectrometers, respectively. The energy resolution ranged from ± 5 % at $E' = 7$ GeV to ± 4 % at $E' = 18$ GeV for each spectrometer. The resulting resolution in $\Delta x/x$ ranged from ± 8 % at low x up to ± 15 % at highest x covered by each spectrometer ($x \leqslant 0.4$ in the $4.5°$ and $x \leqslant 0.6$ in the $7°$ spectrometer).

The experiments E154 and E155 also have used two single-arm spectrometers but at central scattering angles of 2.75 and 5.5°. The structure of the spectrometers was similar to that shown in Fig. 6. The kinematic range covered by two spectrometers was $0.014 < x < 0.7$ and $1 < Q^2 < 17$ GeV^2. The E155 experiment has used an additional spectrometer centred at 10.5° and consisted of a single dipole magnet between two quadrupoles followed by a single scintillator hodoscope, a threshold Cherenkov counter and electromagnetic calorimeter. This additional spectrometer has doubled the Q^2 range covered by 2.75 and 5.5° spectrometers.

3.3.3. The Experiments SLAC E142 and E154. The experiment E142 was designed to measure for the first time the neutron spin-dependent structure functions $g_1^n(x, Q^2)$ and $g_2^n(x, Q^2)$ using a polarized ^{3}He target which can be considered as a neutron target. The main features of the E142 experiment are:

— the polarized high pressure ^{3}He gas target;

— two single-arm spectrometers to measure momenta and energies of scattered electrons at fixed θ.

The experiment E154 has used essentially the same as E142 apparatus but the higher energy of the electron beam.

The E142/154 polarized ^{3}He target relies on the technique of spin-exchange optical pumping [188] referring to a two step process in which: (1) rubidium (Rb) atoms are polarized by optical pumping, and (2) the electronic polarization of the Rb atoms is transferred to the nuclei of the ^{3}He atoms by spin-exchange collisions. The polarized ^{3}He is contained in the 30 cm long glass cells at the pressure of about 9 atm. The target cells comprised two chambers — an upper «pumping chamber» in which the optical pumping and spin exchange took place, and a lower «target chamber» placed in the beam. The pumping chamber was closed by an oven to heat the Rb ^{3}He mixture to about 160 °C. The optical pumping was accomplished with titanium-sapphire lasers through $\lambda/4$ plates to achieve circular polarization. A set of 1.4 m diameter Helmholz coils, coaxial with the electron beam, produced a 20 to 40 G field for ^{3}He nuclear polarization. This polarization was measured by NMR technique with the help of additional RF drive and pickup coils. Additional Helmholz coils transverse to the electron beam were used to rotate the target polarization and for operation with a polarization transverse to the beam.

During the experiment the target polarization was periodically reversed and measured every four hours. The systematic errors of these measurements were

about 7 %. The average ^{3}He polarization over the entire E142 (E154) experiment was about 33 % (38 %).

One of the most important characteristics of the target is a dilution factor f_{He}. This factor in case of E142 defines a fraction of events originating from polarized ^{3}He versus events originating from the rest of the target nuclei. Since the number of events depends on the product of the total number of nucleons and cross section, the dilution factor, as in other experiments, depends on x and Q^2 and is a subject of careful calculations and measurements. It was found that for the E142 spectrometers $f_{\mathrm{He}}(x, Q^2)$ varied from about 30 % at the lowest x to about 35 % at the largest x. For the E154 experiment the dilution factor was found to be 0.55 ± 0.03 over the kinematic range.

3.3.4. The Experiments SLAC E143 and E155. The goal of the E143 experiment was to measure the longitudinal $(A_\parallel)$ and transverse $(A_\perp)$ asymmetries in DIS of longitudinally polarized electrons from polarized protons and deuterons. The main components of the experimental equipment were:

— the polarized proton and deuterium targets;

— two spectrometers to detect scattered electrons.

The E143/155 have used a spin-frozen type of the polarized target with ^{15}NH$_3$ or ^{15}ND$_3$ as the target material [185]. The target required a liquid helium evaporation refrigerator operating near 1 K and a 5 T superconducting magnet. The target insert containing ^{15}ND$_3$, ^{15}NH$_3$, empty and C or Al cells can slid down and up to position any of them into the beam. ^{15}N ammonia (spin 1/2) was chosen over ^{14}N-ammonia (spin 1) to reduce systematic errors of the proton structure functions by eliminating unwanted contributions from neutrons. The ^{15}NH$_3$ targets contained typically: 13 % free protons, 66 % ^{15}N, 10 % ^{4}He, 6 % Al and 5% Cu-Ni. The values of the target polarizations were typically 0.65 ± 0.017 for protons and 0.25 ± 0.011 for deuterons [187]; the dilution factors ranged from 0.12 to 0.17 for NH$_3$ and from 0.22 to 0.24 for ND$_3$.

Instead of ammonia, the E155 experiment has used for the first time a new polarized material ^{6}LiD [189] in the target which was 3 cm long, 2.5 cm in diameter and enclosed in an aluminium cup. Lithium deuterid provides a significant improvement of the so-called «target factor of merit», $P_T \cdot f$, defining the experimental counting rate. The nuclei ^{6}Li can be considered as deuteron plus alpha-particle. So, in the polarized ^{6}LiD target half of nucleons are the desired polarized species. It is also five times more radiative resistant than ammonia. The ^{6}LiD contained typically 18 % free deuterons, 53 % ^{6}Li, 14 % He, 11 % Al, 3 % O, and 1 % N by weight. The average over the experiment polarization of deuterons was 22 ± 4 %.

The main characteristics of experiments on the spin structure of nucleons are summarized in Table 2.

Table 2. **Characteristics of polarized experiments**

Experiment, target	Target	E, GeV	Beam	Q^2, GeV^2	x	Beam polarization	Target polarization	Dilution factor, typical
E80, SLAC	Butanol	9–13	$e-$	1.0–3.0	~ 0.1–0.7	0.85 ± 0.08	0.50 ± 0.04	0.13
E130, SLAC	Butanol	16–23	$e-$	3.5–10.0	0.18–0.7	0.81 ± 0.03	0.58 ± 0.04	0.15
E142, SLAC	^{3}He (gas)	19–26	$e-$	1.0–8.0	0.03–0.6	0.36 ± 0.02	0.33 ± 0.03	0.34
E143, SLAC	^{15}NH$_3$	9–30	$e-$	0.5–10.0	0.02–0.8	0.85 ± 0.022	0.65 ± 0.02	0.17
	^{15}ND$_3$	9–30	$e-$	0.5–10.0	0.02–0.8	0.85 ± 0.022	0.25 ± 0.02	0.24
E154, SLAC	^{3}He (gas)	48.3	$e-$	1.0–17.0	0.014–0.7	0.82 ± 0.02	0.38 ± 0.02	0.55
E155, SLAC	^{15}NH$_3$	48.3	$e-$	1.0–40.0	0.014–0.9	0.81 ± 0.02	0.80 ± 0.06	0.15
	^{6}LiD	48.3	$e-$	1.0–40.0	0.01–0.9	0.81 ± 0.02	0.22 ± 0.04	0.36
EMC, CERN	NH$_3$	100	μ^+	1.5–30.0	0.01–0.7	0.77 ± 0.06	0.77 ± 0.05	0.18
		120	μ^+	2.0–40.0	0.01–0.7	0.79 ± 0.06	0.77 ± 0.05	0.18
		200	μ^+	3.0–90.0	0.01–0.7	0.82 ± 0.06	0.77 ± 0.05	0.18
SMC, CERN	C$_4$D$_9$OD	100,190	μ^+	0.2–100.0	0.0008–0.7	0.8 ± 0.02	0.51 ± 0.02	0.12
	C$_4$H$_9$OH	190	μ^+	1.0–60.0	0.00006–0.7	0.8 ± 0.02	0.86 ± 0.03	0.12
	NH$_3$	190	μ^+	0.2–100.0	0.0008–0.7	0.8 ± 0.02	0.89 ± 0.03	0.18
HERMES, DESY	^{3}He (pure gas)	27.5	$e+$	1.0–15.0	0.023–0.6	0.55 ± 0.05	0.46 ± 0.05	1.0
	^{1}H (pure gas)	27.6	$e+$	0.8–20.0	0.02–0.8	0.55 ± 0.04	0.88 ± 0.04	1.0
	^{2}D (pure gas)	27.6	$e\pm$	0.2–15.0	0.005–0.85	0.50 ± 0.04	0.85 ± 0.04	1.0

4. WORLD DATA ON SPIN-DEPENDENT
STRUCTURE FUNCTIONS

Prior the data presentation, let us summarize briefly the data processing and evaluation of experimental errors.

Without going into details of the event reconstruction and selection, let us consider, for example, a simplified procedure of calculations of asymmetry A_1 and structure function g_1.

In case of the SMC the measured event rates in x, Q^2 bins from the upstream (u) and downstream (d) target cells with opposite longitudinal polarization are used to determine the asymmetry $A_{\parallel}$:

$$
\begin{aligned}
N_u &= n_u \Phi a_u \sigma_0 (1 - f P_\mu P_{Tu} A_{\parallel}), \\
N_d &= n_d \Phi a_d \sigma_0 (1 - f P_\mu P_{Td} A_{\parallel}),
\end{aligned}
\tag{4.1}
$$

where Φ is the beam flux; P_{Tu} and P_{Td} are polarizations of the target cells; n_u and n_d — the densities of target nucleons; a_u and a_d are spectrometer acceptances and f is a dilution factor defining a fraction of hydrogen in the target material. Instead of f, the effective dilution factor f' should be used in the above expressions for the event rates:

$$
f' = \frac{n_{p,d}\sigma_{1\gamma}^{p,d}}{\Sigma_A n_A \sigma_{\text{tot}}^A},
\tag{4.2}
$$

where $\sigma_{1\gamma}$ is the one-photon-exchange (Born) cross section; σ_{tot} is the total cross section and $n_{p,d,A}$ is a number of corresponding nuclei per square centimeter. The sum runs over all types of target nuclei.

For effective measurements the dilution factor f' should be large. In case of the SMC the f' has varied from about 0.05 to 0.2 in the measured x-region. To increase f' and to make it less x-dependent, the SMC has used a special method of the «hadron-tagged event» selection for which at least one secondary hadron is required in the final state of DIS [43]. With this method $f'(x)$ was almost flat at the level of 0.15.

Similar to (4.1), expressions can be written for reversed polarizations, N'_u and N'_d. Then, assuming that acceptance ratios a_u/a_d and a'_u/a'_d are the same before and after the reversal, one can determine $A_{\text{meas}\parallel}$:

$$
A_{\text{meas}\parallel} = f' P_\mu |P_T| A_{\parallel}
\tag{4.3}
$$

from the double ratio

$$
\left(\frac{N_u}{N_d} \frac{N'_d}{N'_u} \right)^{-2} = \frac{1 + A_{\text{meas}\parallel}}{1 - A_{\text{meas}\parallel}}.
\tag{4.4}
$$

Averaging $A_{\mathrm{meas}\|}$ over the number of reversals, one can reduce the systematic errors caused by possible fluctuations of the beam and target polarizations. Violations of assumptions made above can cause corrections and additional systematic errors. Note, that careful account for systematic errors is very important because the measured values of $A_{\mathrm{meas}\|}$ are small: $A_{\mathrm{meas}\|} \sim 10^{-2} \div 10^{-3}$.

The simplified procedure to calculate g_1 and Γ_1 from $A_{\mathrm{meas}\|}$ is straightforward. From (4.3) we have

$$A_{\|} = \frac{1}{f'|P_T|P_\mu} A_{\mathrm{meas}\|} \tag{4.5}$$

and from (1.12):

$$A_{1\mathrm{meas}} \approx \frac{A_{\|}}{D} = \frac{1}{f'D|P_T|P_\mu} A_{\mathrm{meas}\|}. \tag{4.6}$$

The measured asymmetry $A_{1\mathrm{meas}}$ must be corrected for possible contributions from higher order radiative processes (radiative corrections). These corrections are calculated theoretically and accounted for with the help of iteration procedure [86]:

$$A_1 = A_{1\mathrm{meas}} - \Delta_n^{\mathrm{RC}}(A_1), \tag{4.7}$$

where n is a number of iterations. Usually the iteration procedure is converged after 4–5 steps.

Finally $g_1(x, Q^2)$ is calculated from:

$$g_1(x, Q^2) = \frac{A_1(x, Q^2)F_2(x, Q^2)\left(1 + \dfrac{4M^2x^2}{Q^2}\right)}{1 + R(x, Q^2)}, \tag{4.8}$$

where F_2 and R are unpolarized structure functions known from other experiments. Usually for calculations of $g_1(x, Q^2)$ one takes parameterization of all existing data on F_2 [193] and R [194], known as NMC and SLAC parameterizations, respectively*. In the latest publications SLAC experiments have used new SLAC [195] and NMC [196] parameterizations for R and F_2, respectively, based on additional measurements.

Other DIS experiments have used only one target cell and applied different than the SMC procedure of asymmetries $A_{\|}^d$ and $A_{\|}^p$ calculations from the number of scattered electrons per incident beam (rates) with negative (N_-) and positive

---

*An alternative procedure to calculate g_1 and g_2 from the cross section difference is developed in [199].

(N_+) polarizations. In case of the E155:

$$A_\parallel^d = \left(\frac{N_- - N_+}{N_- + N_+} \frac{1}{f'P_b P_t^d C_1} - C_2 A_\parallel^p \right) \frac{1}{f_{\mathrm{RC}}} + A_{\mathrm{RC}},$$

$$A_\parallel^p = \frac{N_- - N_+}{N_- + N_+} \frac{C_N}{f'P_b P_t^p f_{\mathrm{RC}}} + A_{\mathrm{RC}},$$

where f' is a dilution factor; f_{RC} is a multiplicative and A_{RC} is an additive radiative correction; $C_1, C_2,$ and C_N account for the presence of several polarizable nuclei in the target: C_1 includes contribution from free deuterons and deuterons inside $^6\mathrm{Li}$, C_2 accounts for polarized protons in LiH and $^7\mathrm{Li}$ and C_N accounts for polarized nitrogen nuclei in the $^{15}\mathrm{NH}_3$ target.

The rates N_- and N_+ have been corrected for a number of effects and corresponding uncertainties are included in systematic errors.

The method of asymmetry extraction applied by the HERMES is different due to peculiarities of the circulating beam and usage of the pure gas target. The cross section asymmetry $A_\parallel$ is given by:

$$A_\parallel = \frac{N^- L^+ - N^+ L^-}{N^- L_P^+ + N^+ L_P^-}.$$

Here, $N^+(N^-)$ is the number of scattered positrons for target spin parallel (antiparallel) to the beam spin orientation. The dead time-corrected luminosities for each target spin state are L and L_P, the latter being weighted by the product of the beam and target polarization. The structure function ratio g_1/F_1 is approximately equal to the longitudinal virtual photon asymmetry A_1 and it is calculated from $A_\parallel$ using Eq. (1.12).

The values $g_1(x, Q^2)$ calculated from Eq. (4.8) refer to the number of events observed within certain x- and Q^2 bins and should be considered as $g_1(x, Q^2) \equiv g_1(\langle x_i \rangle, \langle Q_{xi}^2 \rangle)$, where $\langle x_i \rangle$ and $\langle Q_{xi}^2 \rangle$ are average values for a given bin. From pure kinematic considerations the values of $\langle Q_{xi}^2 \rangle$ are increased with x increasing. For the analysis and interpretations, the measured $g_1(\langle x_i \rangle, \langle Q_{xi}^2 \rangle)$ are evolved to some average for a particular experiment value of $Q^2 = Q_0^2$: $g_1(\langle x_i \rangle, \langle Q_{xi}^2 \rangle) \rightarrow g_1(x, Q_0^2)$.

To compare the data with the sum rule predictions, the first moment of $g_1(x, Q_0^2)$ is calculated:

$$\Gamma_1(Q_0^2) = \int_0^1 g_1(x, Q_0^2)dx = \int_0^{x_{\min}} + \int_{x_{\min}}^{x_{\max}} + \int_{x_{\max}}^1, \qquad (4.9)$$

where $x_{\min}$ and $x_{\max}$ are experimental limits. To calculate Γ_1, one needs to extrapolate the data measured between $x_{\min}$ and $x_{\max}$ to $x = 0$ and $x = 1$. The problem of extrapolations is not trivial and will be discussed below.

The experimental values of $g_1(x, Q^2)$ calculated from Eq. (4.8) contain statistical and systematic errors. The statistical errors are determined by the number of events observed within certain x- and Q^2 bins. Typically, millions of DIS events are needed to guarantee the high statistical accuracy. To collect such number of events in the muon beam, the SMC should work for several years. With the high intensity electron beam the SLAC experiments have collected the statistics in a relatively short period of time. HERMES also has used the intense electron or positron HERA beam but a low density gas target limits the rate of data accumulation compared to this of SLAC. The longer periods of data taking the more difficulties arise to control the stable conditions of the beam and apparatus and to minimize systematic errors.

The systematic errors are determined by instabilities of the apparatus, uncertainties of parameters and procedures of calculations. Usually each source of uncertainties is estimated separately and then all of them are combined in quadratures. Sometimes one needs to take into account possible correlations between errors. Typical sources and values of systematic errors are given in Table 3 from which one can also see a comparison of total systematic and statistical errors on Γ_1 determined for the proton and deuterium data.

In Table 3 the following sources of systematic uncertainties are considered and their contributions to Γ_1 are quoted by the experiments: beam momentum (E), parameterization of the unpolarized structure functions (F_2), extrapolation of $g_1(x)$ to $x = 0$ ($x \rightarrow 0$), target polarization measurements (P_T), acceptance variations (ACC), dilution factor (DIL), beam polarization (P_μ), neglecting $A_2 (A_2 = 0)$, radiative corrections (RC), extrapolation of $g_1(x)$ to $x = 1$ ($x \rightarrow 1$), measurements of a momentum and angle of scattered muons (Δp, $\Delta\theta$).

As is seen from Table 3, systematic errors are rather large and in some cases they limit the precision of measurements. For example, measuring the $\Gamma_1^p(\Gamma_1^d)$, the SMC (E143) obtained a statistical accuracy of 4 % (8 %). Further increase of statistics will be useless because the result will be limited by the systematic error of 5 % (10 %).

Low systematic errors and their careful estimations are the signatures of the precision experiments. In DIS experiments, the systematics has either hardware or physics origins. In case of the SMC, the hardware systematics includes E, P_T, ACC, DIL, P_μ and Δp, $\Delta\theta$ uncertainties from which E, P_T, and P_μ give the largest contributions to the total errors (see Table 3). With the present technique it is difficult to reduce these uncertainties substantially. Some improvements are possible for future experiments in the determination of incident energies and in measurements of the beam and target polarizations and characteristics of scattered particles.

Reduction of systematics is also possible by means of the optimized software procedures used during the data processing from the stage of raw data to the stage of final physics results. These procedures should include dividing of the whole

Table 3. **Sources and typical values of the systematic errors**

Source	$\Delta\Gamma_1^p$, SMC [43]	$\Delta\Gamma_1^p$, E143 [53]	$\Delta\Gamma_1^d$, SMC [43]	$\Delta\Gamma_1^d$, E143 [53]
E	0.0060	—	0.0015	—
F_2	0.0023	0.003	0.0010	0.0010
$x \to 0$	0.0043	0.008	0.0009	0.0060
P_T	0.0037	0.002	0.0012	0.0020
ACC	0.0015	—	0.0014	—
DIL	0.0027	0.002	0.0006	0.0010
P_μ	0.0029	0.003	0.0008	0.0010
$A_2 = 0$	0.0005	—	0.0006	—
RC	0.0007	0.002	0.0008	0.0010
$x \to 1$	0.0007	0.001	0.0009	0.0010
$\Delta p, \Delta\theta$	0.0003	—	0.0003	—
$\Delta\Gamma_1$ (syst. tot.)	0.0062	0.006	0.0026	0.0030
$\Delta\Gamma_1$ (stat.)	0.0052	0.006	0.0057	0.0040
Γ_1	0.120	0.121	0.0190	0.0440
$\Delta\Gamma/\Gamma$ (syst.), %	5	5	14	10
$\Delta\Gamma/\Gamma$ (stat.), %	4	5	30	8

sample of the data in subsamples with relatively stable conditions on ΔE, ΔP_T, ΔP_μ, treatment of the subsamples separately and averaging of the results at the end [199].

The systematics of the physics origin, i. e., F_2, $x \to 0$, $x \to 1$, RC, and A_2, is almost impossible to control inside the particular experiment. Minor uncertainties related with neglecting A_2 can be removed in principle performing a combined analysis of data on longitudinal $A_\parallel$ and transverse $A_\perp$ asymmetries, if available. But remaining uncertainties are either fixed by the geometrical conditions of the experiments ($x \to 0$, $x \to 1$, and RC) or introduced from outside using the unpolarized measurements of $F_2(x, Q^2)$ and $R(x, Q^2)$. The last source of systematics, the largest of physics uncertainties, can be eliminated in principle calculating g_1 and g_2 not from asymmetries of cross sections but from differences of cross sections, as suggested in [199]. But this possibility has been never realized in the performed experiments.

The SMC, E143, and E155 have used proton and deuterium targets. From measurements of g_1^d and g_1^p one can calculate g_1^n:

$$g_1^n = \frac{g_1^d}{1 - 1.5\omega_D} \frac{F_1^n + F_1^p}{F_1^d} - g_1^p,$$

where $\omega_D = 0.05 \pm 0.01$ [197] is a probability of the D state in deuteron.

The HERMES and SLAC E142/154 experiments have used the ^{3}He targets. From the measurements of $A_\parallel^{^3\mathrm{He}}$ and $A_\perp^{^3\mathrm{He}}$ one can calculate $A_1^{^3\mathrm{He}}$ and $g_1^{^3\mathrm{He}}$ and then A_1^n and g_1^n. The main reason is that in the naive approximation the ^{3}He nucleus consists of three nucleons in a specially symmetric S state. The Pauli principle demands the overall wave function to be antisymmetric. Exchanging the two protons in ^{3}He must yield a symmetric wave function. In this picture, the two proton spins are antiparallel to one another, resulting in a cancellation of spin-dependent effects coming from the protons. Naturally, the ^{3}He nucleus is not exactly a system of nucleons in the pure S state and exact ^{3}He wave function must be used to extract the degree of polarization of the neutron. In the deep inelastic region A_1^n and g_1^n can be extracted from ^{3}He data using a simplified procedure which accounts for S, S', and D states of the ^{3}He wave function:

$$g_{1,2}^n = \frac{1}{\rho_n} \left(g_{1,2}^{^3\mathrm{He}} - 2\rho_p g_{1,2}^p \right),$$

$$A_{1,2}^n = \frac{F_2^{^3\mathrm{He}}}{F_2^n} \frac{1}{\rho_n} \left(A_{1,2}^{^3\mathrm{He}} - 2\frac{F_2^p}{F_2^{^3\mathrm{He}}} \rho_p A_{1,2}^p \right),$$

where $\rho_n = (87 \pm 2)\,\%$ and $\rho_p = (-2.7 \pm 0.4)\,\%$ are effective polarizations of the neutron and proton in ^{3}He due to the S, S', and D states of the wave function. The data on g_1^p and A_1^p are taken from the E143 experiment [49, 50].

The SMC and world data on spin physics have been reviewed earlier in papers [77] and [78], respectively.

4.1. Data on Asymmetries $A_1(x, Q^2)$ **and Structure Functions** $g_1(x, Q^2)$.
4.1.1. The x- and Q^2 Dependence of A_1 and g_1. The data on asymmetries and structure functions for protons and deuterons have been obtained by SMC [35–46], SLAC E143 [49–53] and E155 [73–75] and HERMES [57] collaborations. Having measurements from hydrogen and deuterium targets, one can calculate asymmetries and structure functions for neutrons. The collaborations SLAC E142 [54, 55] and E154 [69–72] and HERMES [56] have measured asymmetries and structure functions from ^{3}He targets which can be considered as neutron targets.

The final SMC data [43] together with other data on the virtual photon asymmetries A_1^p and A_1^d are shown in Fig. 7 as a function of Q^2 at various x.

The SLAC experiments prefer to present data in a form of ratio:

$$\frac{g_1}{F_1} = \frac{A_\parallel}{D} + \frac{g_2 \gamma^2}{F_1},$$

which is approximately equal to A_1 (see Eq. (1.12)). An account for the g_2 term changes the results for a few percent. The SLAC E155 data on g_1/F_1 [73, 76] are shown in Fig. 8 together with other data which are slightly changed to include the g_2 term neglected previously. Most of the E155 systematic errors arising
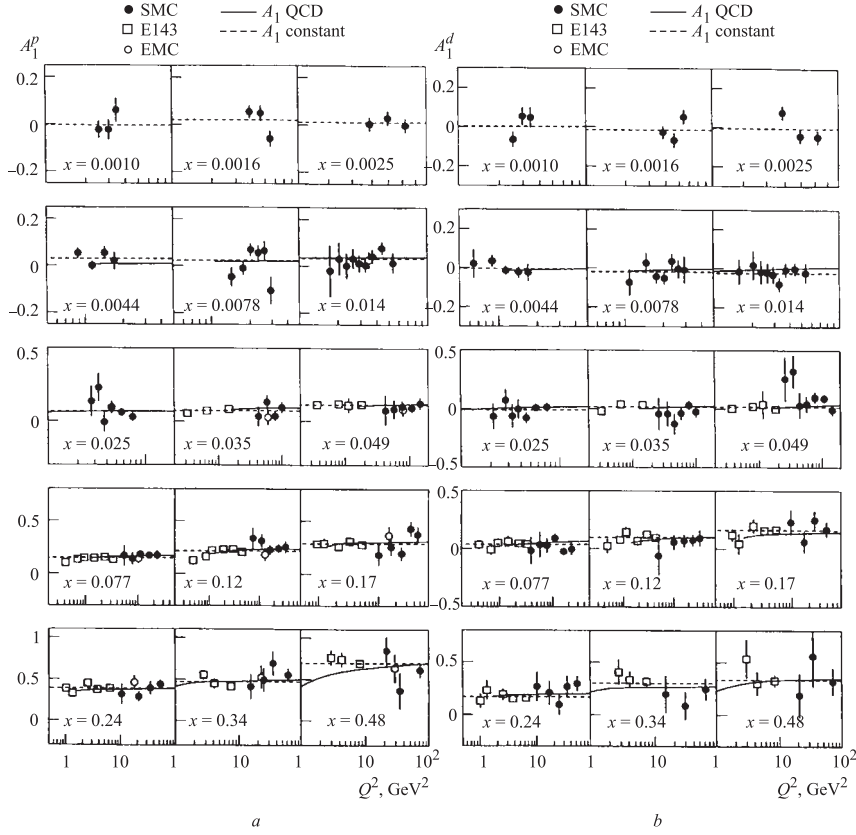
Fig. 7. The final SMC data on the virtual photon asymmetry A_1^p (*a*) and A_1^d (*b*) as a function of the scaling variable x and four momentum transfer Q^2. The closed (open) symbols are data from the SMC (E143 and EMC) experiments. The solid line is a result of the QCD fit [44]. The dashed line is the fit assuming no Q^2 dependence

from uncertainties of the beam and target polarizations, fraction of polarizable nucleons and various corrections are common for a given target and correspond to the overall normalization error of about 7.6 % for the proton data. The remaining systematic errors like errors in radiative corrections, F_1 and resolution corrections vary smoothly with x from a few percent of measured g_1 for midrange x up to 15 % for the high and low x bins.

Within the quoted errors, the E155 data are consistent with other data allowing an overall normalization factor $1.08 \pm 0.03 \pm 0.07$ for the proton data.
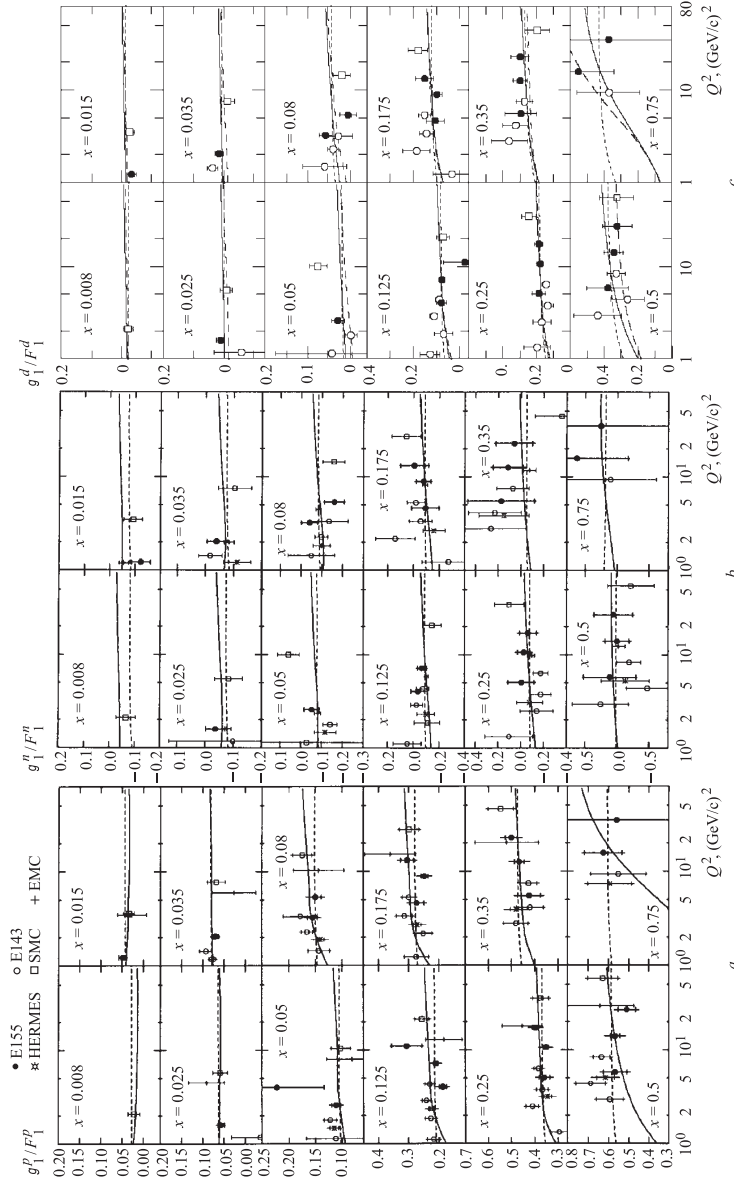
Fig. 8. Values g_1^p/F_1^p (a), g_1^n/F_1^n (b) and g_1^d/F_1^d (c) vs. Q^2 at various x obtained by E155 and compared to other experiments assuming the g_2^{WW} model for g_2. Inner errors are statistical only, while systematic errors are included in the outer error bars. The solid curves correspond to the E154 NLO QCD fit described in Subsec. 4.1.2, while the dashed curves are from the simple fit (4.10). The long-dashed curves are the SMC NLO fit described in the text
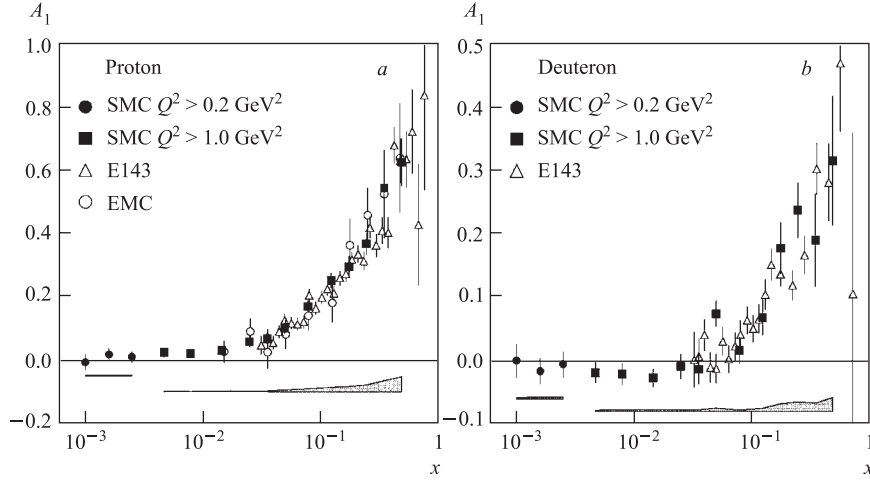
Fig. 9. The virtual photon asymmetry A_1^p (a) and A_1^d (b) as a function of the scaling variable x obtained by SMC and compared to other data. Each point is given at Q^2 corresponding to its average value for a given x bin. Statistical errors are shown as error bars. Shaded bands below indicate SMC systematic errors

All data on A_1 are in perfect agreement. For the Q^2 regions covered by considered experiments no Q^2 dependence is seen within the errors. So, the data can be averaged over Q^2 of the corresponding x bin and presented as $A_1^{p(d)}(x, \langle Q_{xi}^2 \rangle) \equiv A_1^{p(d)}(x)$ (see Fig. 9).

The final SMC data [43] on $g_1(x)$ evolved [42] to the same $Q_0^2 = 5$ GeV^2 are shown in Fig. 10. The E155 data on g_1 presented in the same way are shown in Fig. 11, a, b. The smallest x SMC points are not shown in these figures. In the overlapping x regions the data are in agreement. At $x < 0.02$ there are data from the SMC experiment only.

The low-x data on g_1^p and g_1^d from SMC [45] cover a range: $6 \cdot 10^{-5} < x < 0.15$, $0.01 < Q^2 < 20$ GeV^2 which has not been investigated before. These data have been obtained with the smallest-angle trigger (see Subsec. 3.1.3). No significant spin effects are seen in this region (Fig. 12).

The HERMES data on A_1^n and g_1^n are shown in Fig. 13 and compared to E142.

As is seen from Figs. 7–13, the data obtained by different collaborations are compatible. The main characteristics of these data are the positive values of $g_1^p(x)$ in the measured x range and relatively large negative values of g_1^n at low x observed for the first time by SMC [36] and confirmed by other experiments
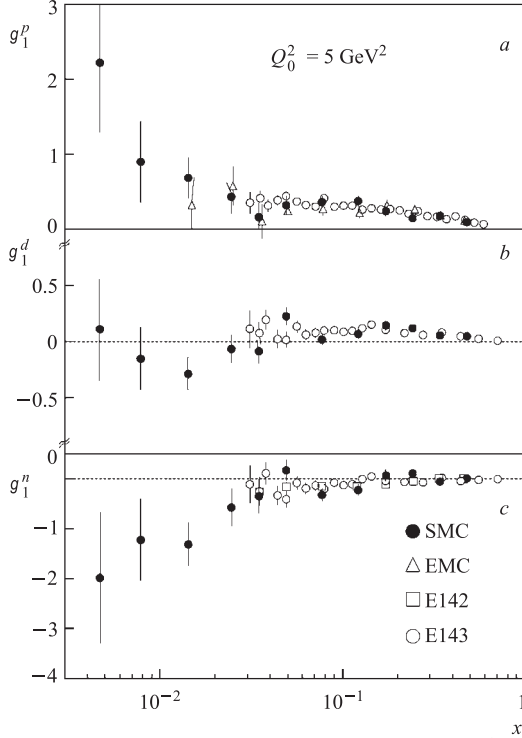
Fig. 10. The SMC measurements of g_1^p (a), g_1^d (b) and g_1^n (c) evolved to $Q_0^2 = 5$ GeV^2 and compared to other data

with better precision. It is obvious from these figures that the data on $g_1^n(x)$ are less accurate than the ones on $g_1^{p,d}(x)$, especially in the region of $x < 0.05$.

Plots in Figs. 7 and 8 show no significant Q^2 dependence of A_1^p and A_1^d. The fits of A_1 by constant values in each x bin are consistent with the data within the errors. Although A_1 seems to be Q^2-independent, g_1 can depend on Q^2 due to F_2 entering in its definition (see (4.8)).

The Q^2 dependence of the $g_1^{p,d,n}$ has been examined by various groups using the global phenomenological fits containing Q^2-dependent part and fits of data to the QCD predictions.

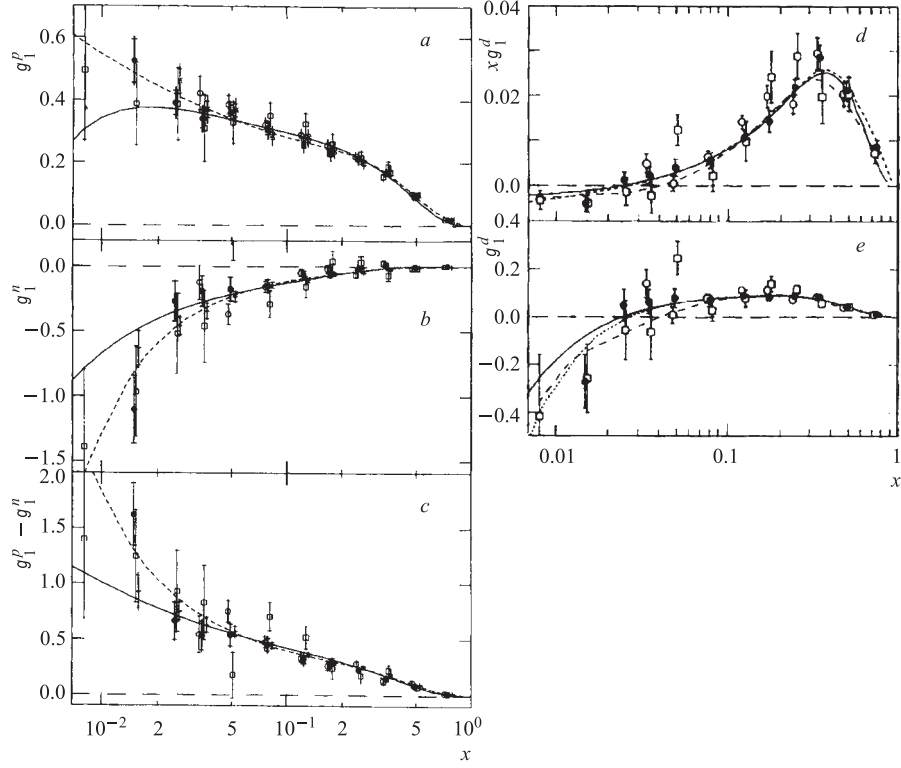For the global phenomenological fits the E143 has used the ratios g_1^p/F_1^p and g_1^d/F_1^d parameterized in the form $ax^\alpha(1 + bx + cx^2)[1 + Cf(Q^2)]$. Four types of the Q^2-dependent term $f(Q^2)$ have been considered:

fit I: $f(Q^2) = 0$, all data points, $\chi^2/DF = 125/104$;

fit II: $f(Q^2) = 0$, data points at $Q^2 < 1$ GeV^2 are excluded, $\chi^2/DF = 94/82$;

fit III: $f(Q^2) \sim 1/Q^2$, all data points, $\chi^2/DF = 104/102$;

fit IV: $f(Q^2) \sim \ln(1/Q^2)$, all data points, $\chi^2/DF = 113/102$.

Although the data consistent with no Q^2 dependence (fit I), better fits are obtained with the correction term $\sim 1/Q^2$ and coefficients $C_p \approx -0.2$ and $C_d \approx -0.5$ for protons and deuterons, respectively.

Fig. 11. Data for g_1^p (a), g_1^n (b), $g_1^p - g_1^n$ (c), xg_1^d (d) and g_1^d (e) evaluated by E155 at $Q_0^2 = 5$ GeV^2. The data are from E155 experiment (solid circles), E143 (open circles), SMC (squares), HERMES (stars), and E154 (crosses). The $g_1^p - g_1^n$ values were obtained from the proton and deuteron results of E155, E143, and SMC, while the proton E155 and neutron E154 results were used to obtain the results with the cross symbol. The curves are as in Fig. 8

Similar parameterization for the world data on g_1 has been used by E155 [75] at $Q^2 > 1$ GeV^2 and $W > 2$ GeV which found:

$$\frac{g_1^p}{F_1^p} = x^{0.70}(0.817 + 1.014x - 1.489x^2)\left(1 + \frac{a^p}{Q^2}\right),$$

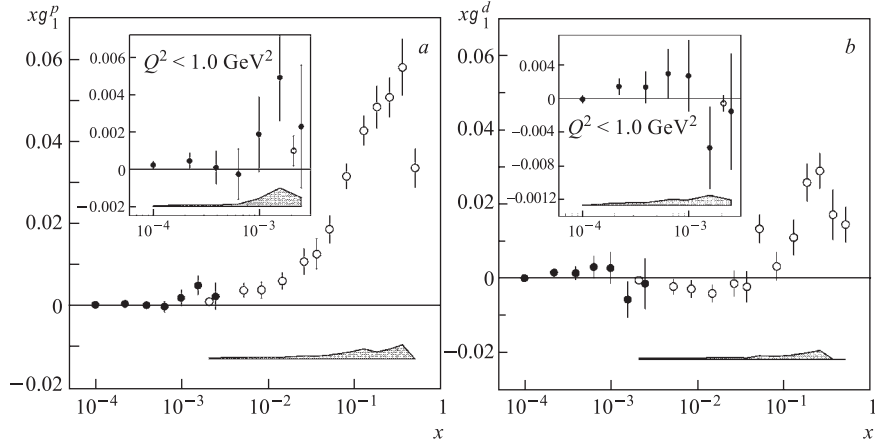$$\frac{g_1^n}{F_1^n} = x^{-0.335}(-0.013 - 0.330x + 0.761x^2)\left(1 + \frac{a^n}{Q^2}\right). \tag{4.10}$$

Fig. 12. The values of xg_1^p (a) and xg_1^d (b) obtained by the SMC with the low x (filled circles) and standard triggers (open circles). The data for $Q^2 < 1$ GeV^2 are shown in the inserts
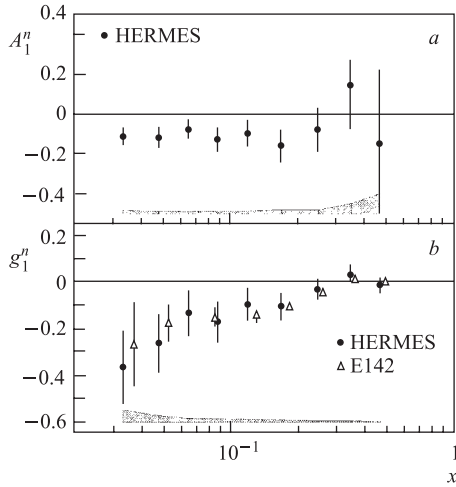

Fig. 13. The HERMES data on the asymmetry A_1^n and the structure function g_1^n as a function of x. Each point is given at Q^2 corresponding to its average value for a given x bin. The error bars are statistical uncertainties. The systematic uncertainties are shown by the error bands. The E142 data are displaced slightly in x for better comparison

Coefficients $a^p = -0.04 \pm 0.06$ and $a^n = 0.13 \pm 0.45$ are small and consistent with zero. These parameterizations are shown in Fig. 8, a–c by the dashed lines.

To examine the x dependence of g_1 at fixed Q^2, the E155 has averaged the data over Q^2 assuming the phenomenological fits above to obtain results for g_1^d, g_1^p, g_1^n and $g_1^p - g_1^n$ at $Q_0^2 = 5$ GeV^2 shown in Fig. 11, a, b by the dashed lines.

The proton data suggest that g_1^p is approximately constant as $x \to 0$ but the deuteron and neutron data consistent with the trend of $g_1^{d,n}$ to become increasingly negative at low x observed for the first time by the SMC and confirmed by the E154 data.

4.1.2. The QCD Analysis of Data on g_1. The QCD analysis of different sets of the $g_1(x, Q^2)$ has been performed by several groups [42, 44, 50, 71, 106–111]. Below we will comment and show results obtained by the experimental groups: SMC [44], E143 [50], and E154 [71]. The progress in the analysis will be seen in parallel with the progress in the data accuracy. Two QCD formalisms have been developed. The first one is by Ball et al. [106] and the second one is by Gluck et al. [107].

SMC has used the QCD formalism developed by Ball et al. [106]. The quality of the QCD fits of the preliminary SMC and E143 data is seen from Fig. 14, *a*. SMC fits [42] are performed at different Q^2: at Q^2 corresponding to $\langle Q_{xi}^2 \rangle$ of the data, at $Q^2 = 10$ GeV^2 which is average Q^2 of the SMC data and at $Q^2 = 1$ GeV^2 which is closer to average Q^2 of the SLAC data. Only a qualitative agreement between the fits and data is seen from this figure. The E143 collaboration has compared [50] the data on g_1^p/F_1^p and g_1^d/F_1^d with QCD NLO analysis performed by Ball et al. [106] and by Gluck et al. [107] (see Fig. 14, *b*, *c*). No definite conclusions can be drawn from this comparison. The theoretical curves are rather different, especially in the case of g_1^d. Qualitatively the data behaviour is closer to that obtained by the Gluck et al. formalism.

The collaboration E154 has performed the QCD fits [71] using the formalism of Gluck et al. [107]. The more complete data of E143, SMC, and E154 on g_1^p and g_1^n have been used. The fits have been performed both in $\overline{MS}$ and AB schemes. The initial parameterizations of polarized parton distributions were found at $Q_i^2 = 0.34$ GeV^2

$$\Delta f \left(x, Q_i^2 \right) = A_f x^{\alpha_f} (1 - x)^{\beta_f} f(x, Q_i^2), \tag{4.11}$$

where $\Delta f = \Delta u_V$, Δd_V, $\Delta \overline{Q}$, and ΔG are polarized valence, sea and gluon distributions, and $f(x, Q_i^2)$ are the unpolarized parton distributions [90]. Eight parameters, A_u, A_d, $A_{\overline{Q}}$, A_G, α_u, α_d, $\alpha_{\overline{Q}}$, α_G, are determined by fits. The total χ^2 of the best fits are 146 and 148 for 168 points in $\overline{MS}$ and AB schemes, respectively. The results of the $\overline{MS}$ and AB fits for the parameters are consistent within the errors but poorly determined by each of the two. Fits to the structure functions at $Q_0^2 = 5$ GeV^2 are shown in Fig. 15. Since the fits are excellent, it is worthwhile to comment some assumption made by the authors which are not common for the standard QCD approach corresponding to Eqs. (1.18)–(1.21). These comments are as follows:
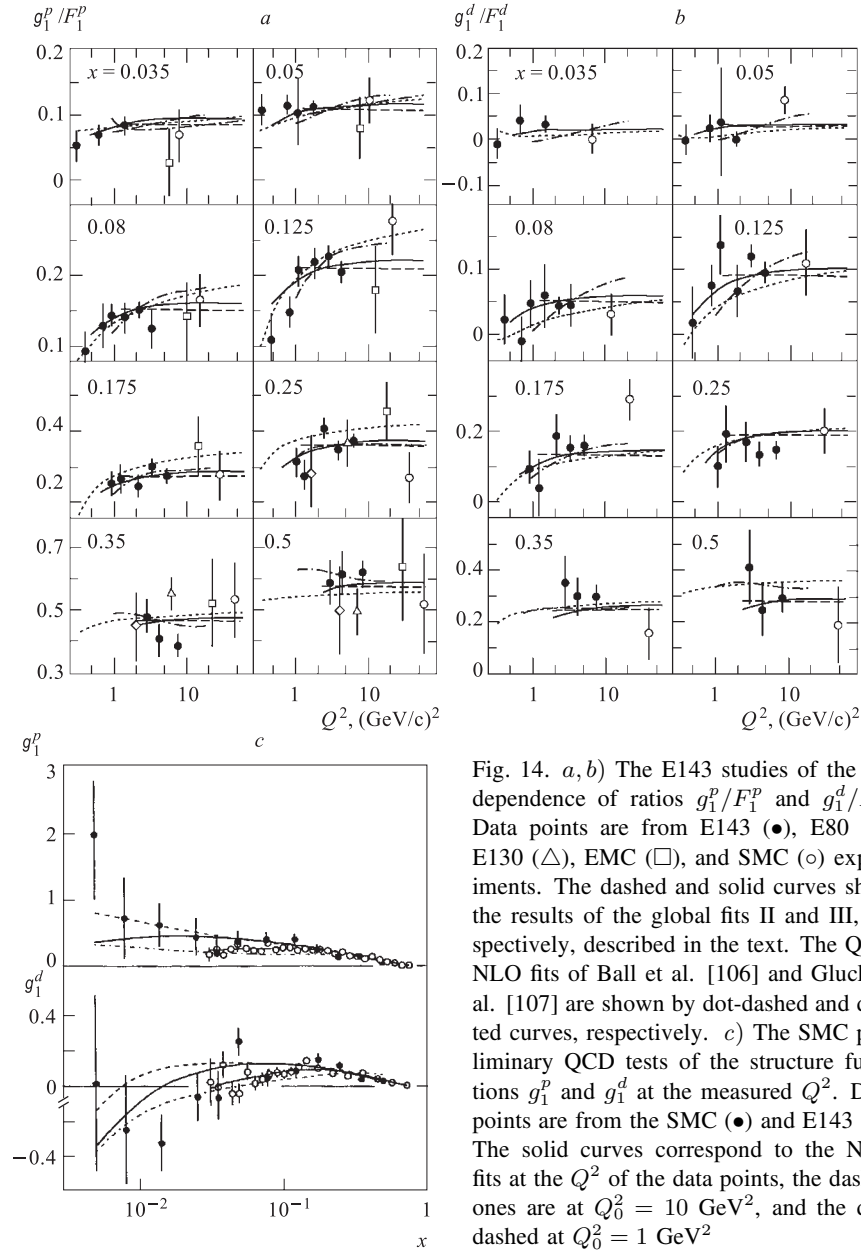
Fig. 14. a, b) The E143 studies of the Q^2 dependence of ratios g_1^p/F_1^p and g_1^d/F_1^d. Data points are from E143 ($\bullet$), E80 ($\diamond$), E130 ($\triangle$), EMC ($\square$), and SMC ($\circ$) experiments. The dashed and solid curves show the results of the global fits II and III, respectively, described in the text. The QCD NLO fits of Ball et al. [106] and Gluck et al. [107] are shown by dot-dashed and dotted curves, respectively. c) The SMC preliminary QCD tests of the structure functions g_1^p and g_1^d at the measured Q^2. Data points are from the SMC ($\bullet$) and E143 ($\circ$). The solid curves correspond to the NLO fits at the Q^2 of the data points, the dashed ones are at $Q_0^2 = 10$ GeV^2, and the dot-dashed at $Q_0^2 = 1$ GeV^2

— an isospin-symmetric sea is assumed, i. e., $\Delta\bar{u} = \Delta\bar{d} = 1/2(\Delta\bar{u} + \Delta\bar{d})$. Under this assumption, the sea quarks contribute equally to the proton and neutron;
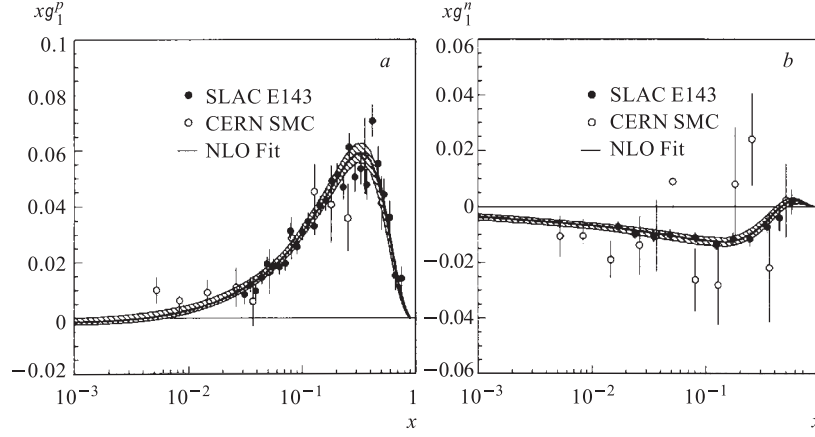
Fig. 15. The structure functions xg_1^p (a) and xg_1^n (b) obtained by different experiments and evolved by the E154 collaboration to $Q_0^2 = 5$ GeV^2 using a procedure based on the Gluck et al. formalism [107] in $\overline{MS}$ scheme (solid lines). The hatched area represents the total errors of the fits

— a particular combination of sea quark distributions is parameterized:

$$\Delta\overline{Q} = 1/2(\Delta\bar{u} + \Delta\bar{d}) + 1/5\Delta\bar{s};$$

— x dependence of the polarized strange and sea quarks is assumed to be the same;

— possible higher twist effects are neglected;

— the initial Q_i^2 is surprisingly low. Stability of results versus a variation of Q_i^2 was not tested;

— the fixed-flavor scheme with $n_f = 3$ is used; the heavy quark contributions are included in the running $\alpha_s(Q^2)$;

— the value of $\alpha_s(Q^2)$ is fixed to that corresponding to $\alpha_s(M_z^2) = 0.109$ or $\alpha_s(5 \text{ GeV}^2) = 0.237$ but not to that corresponding to the world average.

The detailed QCD analysis of the final SMC and other (EMC, E143, E142, E154, and HERMES) published data has been performed by the SMC in the most complete way [44]. Two different mathematical approaches and computer codes have been applied. The SMC has used the standard method of g_1 representation described in Subsec. 1.2.2 which differs from the method used by the E154. The initial polarized parton distributions are parameterized at the starting (initial) value $Q^2 = Q_i^2$ as:

$$\Delta f(x, Q_i^2) = N(\alpha_f, \beta_f, a_f)\eta_f x^{\alpha_f}(1 - x)^{\beta_f}(1 + a_f x), \qquad (4.12)$$
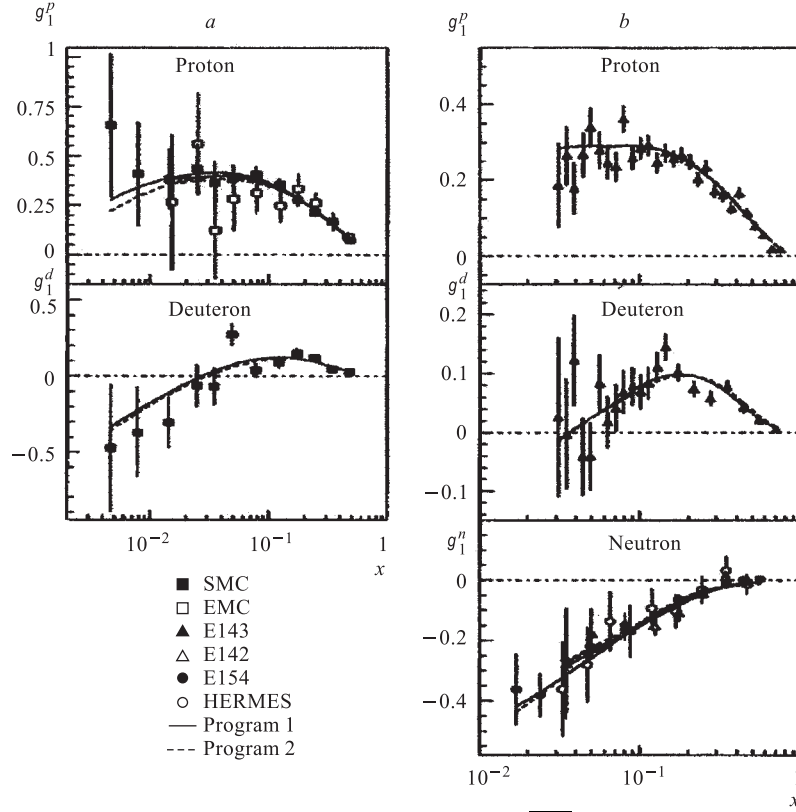
Fig. 16. Comparison of results obtained by the SMC in $\overline{MS}$ scheme using two computer programs. Data on $g_1^{p,d}$ from SMC (a) and on $g_1^{p,d,n}$ from SLAC and DESY experiments (b) are shown at the measured Q^2 together with the QCD fits

where Δf denotes $\Delta\Sigma$, Δq_{NS} or Δg (see (1.18)) and $N(\alpha, \beta, a)$ is fixed by the normalization condition:

$$N(\alpha, \beta, a) \int\limits_0^1 x^\alpha (1-x)^\beta (1+ax) dx = 1.$$

With this normalization the parameters η_g, η_{NS}, and η_S are the first moments of the gluon, nonsinglet quark and singlet quark distributions at Q_i^2, respectively. The normalization of the nonsinglet quark densities $\eta_{NS}^{p,n}$ are fixed using the neutron and hyperon β decay constant and assuming $SU(3)$ flavor symmetry. Then, the initial parton distributions are evolved to the x and Q^2 of the data

points using Eqs. (1.19)–(1.21) with the world average $\alpha_s(M_z^2) = 0.118 \pm 0.003$, the g_1 is evaluated using the Eq. (1.18) and χ^2 is determined as

$$\chi^2 = \sum_{i=1}^{n} \frac{g_1^{\text{calc}}(x, Q^2) - g_1^{\text{data}}(x, Q^2)}{[\delta_{\text{stat}}(g_1)]^2},$$

where n stands for the number of data points applied in the analysis. The χ^2 is minimized by changing the initial parton distribution coefficients η_f, α_f, β_f, and a_f to get the best fit at the $Q_i^2 = 1$ or 10 GeV^2. Only the statistical errors of the data were used in the fit. The systematic uncertainties were estimated separately.

In the paper [42] the SMC has applied the computer code («Program 1») based on the formalism of Ball et al. [106]. Another program which is based on the different mathematical approach to the computations of evolutions was developed within the SMC («Program 2») [106]. As is seen from Fig. 16, the results obtained by the two programs in the $\overline{MS}$ scheme are almost identical and Q_i^2-independent. This has proved the reliability and stability of the SMC QCD analysis. The best parameters of the two fits are given in Table 4. All parameters except those for gluons are nearly the same. The coefficients of the gluon distribution (η_g and α_g) are consistent within the errors but poorly

Table 4. **Parameters determining the polarized parton distributions (4.12) obtained by SMC from fits at the initial $Q_i^2 = 1$ and 10 GeV^2 using the two QCD programs in $\overline{MS}$ scheme**

Parameter	$Q_i^2 = 1$ GeV^2		$Q_i^2 = 10$ GeV^2	
	Program 1	Program 2	Program 1	Program 2
η_S	$0.19^{+0.04}_{-0.05}$	$0.18^{+0.04}_{-0.05}$	$0.18^{+0.04}_{-0.07}$	$0.12^{+0.08}_{-0.17}$
α_S	$-0.46^{+0.12}_{-0.11}$	$-0.43^{+0.13}_{-0.13}$	$-0.61^{+0.12}_{-0.13}$	$-0.72^{+0.10}_{-0.16}$
β_S	$3.05^{+0.38}_{-0.35}$	$3.23^{+0.41}_{-0.38}$	$3.81^{+0.43}_{-0.42}$	$3.60^{+0.63}_{-0.43}$
a_S	$-13.0^{+1.2}_{-1.4}$	$-12.2^{+1.3}_{-1.5}$	$-21.0^{+2.9}_{-4.0}$	$-22.9^{+5.2}_{-6.8}$
η_g	$0.21^{+0.27}_{-0.21}$	$0.38^{+0.29}_{-0.28}$	$0.22^{+0.19}_{-0.18}$	$0.61^{+1.8}_{-0.55}$
α_g	$0.48^{+3.24}_{-1.36}$	$1.02^{+1.44}_{-1.25}$	$0.56^{+0.75}_{-0.94}$	$-0.44^{+1.30}_{-0.48}$
α_{NS}	$-0.11^{+0.05}_{-0.05}$	$-0.12^{+0.05}_{-0.05}$	$-0.29^{+0.03}_{-0.03}$	$-0.29^{+0.03}_{-0.03}$
β_{NS}	$1.69^{+0.16}_{-0.16}$	$1.68^{+0.15}_{-0.15}$	$2.22^{+0.16}_{-0.15}$	$2.12^{+0.16}_{-0.15}$
χ^2	127.4	119.8	122.6	118.8
d. f.	133-8	133-8	133-8	133-8

Table 5. **Parameters of parton distributions (4.12) obtained by SMC in the $\overline{M}S$ and AB schemes at $Q_i^2 = 1$ GeV^2**

Parameter	$\overline{MS}$	AB
η_S	$0.19^{+0.04}_{-0.05}$	$0.38^{+0.03}_{-0.03}$
α_S	$-0.48^{+0.11}_{-0.10}$	$1.20^{+0.29}_{-0.27}$
β_S	$3.29^{+0.40}_{-0.37}$	$4.08^{+0.63}_{-0.58}$
a_S	$-13.8^{+1.3}_{-1.5}$	(0.0)
η_g	$0.25^{+0.29}_{-0.22}$	$0.99^{+1.17}_{-0.31}$
α_g	$0.33^{+2.05}_{-1.05}$	$-0.70^{+0.23}_{-0.20}$
β_g	(4.0)	(4.0)
α_{NS}^p	$-0.19^{+0.09}_{-0.08}$	$-0.15^{+0.09}_{-0.08}$
β_{NS}^p	$1.35^{+0.23}_{-0.21}$	$1.42^{+0.23}_{-0.22}$
α_{NS}^n	$0.06^{+0.14}_{-0.13}$	$0.01^{+0.13}_{-0.12}$
β_{NS}^n	$2.59^{+0.52}_{-0.48}$	$2.48^{+0.51}_{-0.44}$
χ^2	122.9	126.3
d. f.	133-10	133-9

determined by each of the two programs, i. e., the polarized gluon distribution is poorly determined by the present data on g_1.

The SMC has performed the QCD analysis in the $\overline{MS}$ and AB schemes (see Table 5). As follows from Subsec. 1.2.2, the physics results should be scheme-independent. Indeed, Fig. 17, a shows that the $\overline{MS}$ and AB fitted g_1 differ in the region of measurements very little. It means that in the two schemes the input parameterizations are flexible enough to describe the data. Parameters of the polarized parton distributions should be similar in both schemes too for the nonsinglet (NS) quark distribution but not for the singlet (S) one and gluon because they are treated by the schemes differently.

These peculiarities are also seen from Table 5. Within the precision of the data, the first moments of the polarized singlet and gluon distributions obtained in the $\overline{MS}$ and AB schemes are compatible with the relation (1.39). The Table 5 results for $\overline{MS}$ scheme are slightly different (but the same within errors) than those of Table 4 because of different fits with 10 and 8 free parameters, respectively.

In Fig.17, b the fitted polarized parton distributions obtained in the $\overline{MS}$ and AB schemes are compared. In the $\overline{MS}$ scheme $\Delta\Sigma$ becomes negative at $x < 0.05$
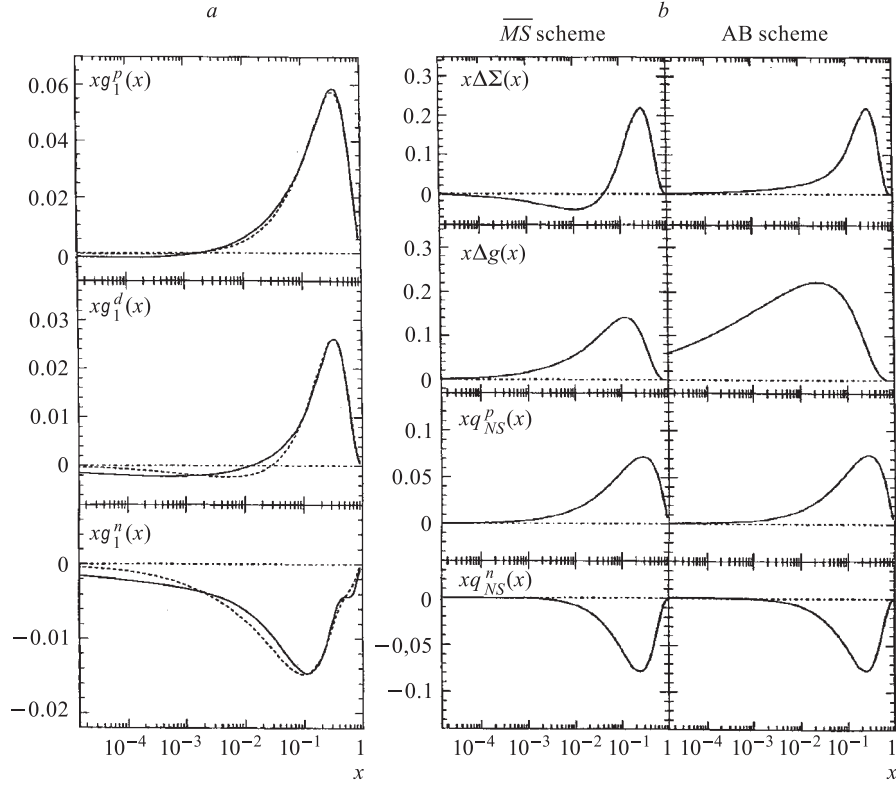
Fig. 17. Comparison of the QCD fits $g_1^{p,n,d}$ (a) and polarized parton distribution functions (b) vs. x at $Q_0^2 = 5$ GeV^2 obtained by the SMC in the $\overline{MS}$ (dotted curves) and AB schemes (solid curves)

due to negative values of g_1^d observed for the first time by the SMC [39]. In the AB scheme $\Delta\Sigma$ remains positive over the whole range of the data. The polarized gluon distribution is larger in the AB scheme and shifted to lower values of x compared to that in the $\overline{MS}$ scheme. The similar features have been obtained in the analysis performed by the E154 collaboration [71]. But this behaviour should be confirmed by future direct measurements of $\Delta g(x)$.

The important feature of the AB fit is the negative value of $g_1^p(x)$ at $x \leqslant 10^{-3}$. As is shown in [71], this can happen due to polarization of sea quarks. So, the experimental observation of the negative value of $g_1^p(x)$ of the proton at $x \leqslant 10^{-3}$ would be a direct evidence of the polarized sea. There is no such indication from the existing data.
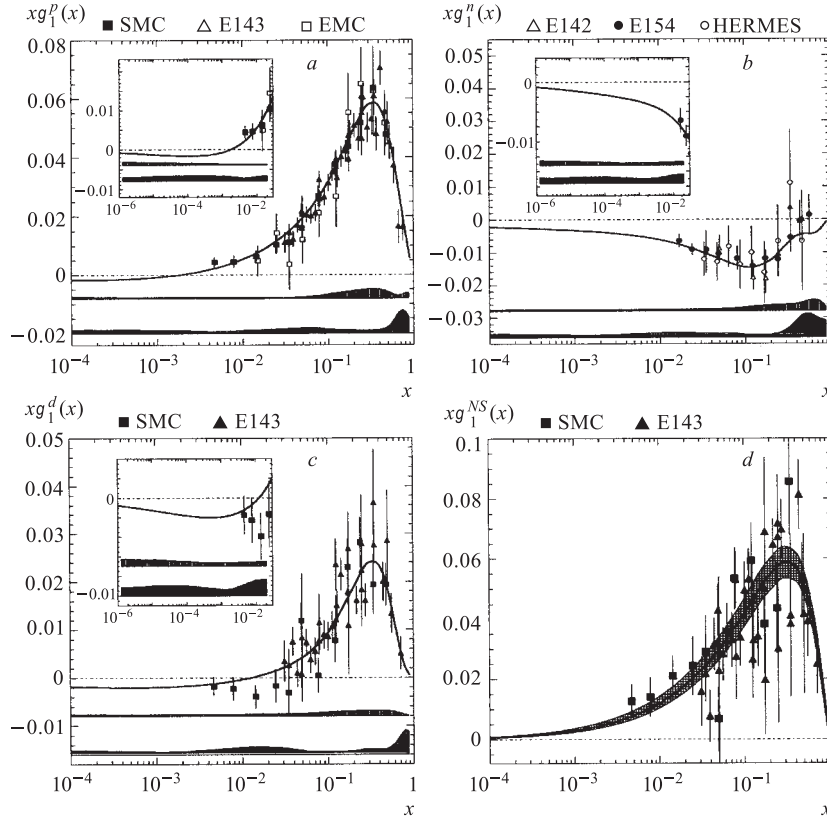
Fig. 18. The world data on xg_1^p (a), xg_1^n (b), xg_1^d (c), and xg_1^{NS} (d) vs. x together with the QCD fits obtained by the SMC at $Q_0^2 = 5$ GeV^2. The low x regions are emphasized in the insets. The data points are shown with their statistical errors. In a–c the uncertainties of the fit due to experimental systematics and theoretical sources are shown by the vertically and horizontally hatched bands, respectively. In d the error band around the curve (cross hatch) represents the systematic uncertainty of the fit, including contributions from experimental systematic and theoretical sources

The results of the SMC best QCD fit of the world data at $Q_0^2 = 5$ GeV^2 including the final SMC data [43] on xg_1^p, xg_1^d, xg_1^n, and xg_1^{NS} are shown in Fig. 18. The fits describe the data very well.

In some papers $g_1(x)$ are calculated and scaled to Q_0^2 assuming that asymmetries A_1^p or ratios g_1^p/F_1^p are Q^2-independent. A comparison of such an evolution (scaling) and the evolution performed by QCD methods of SMC [43], M. Glück,
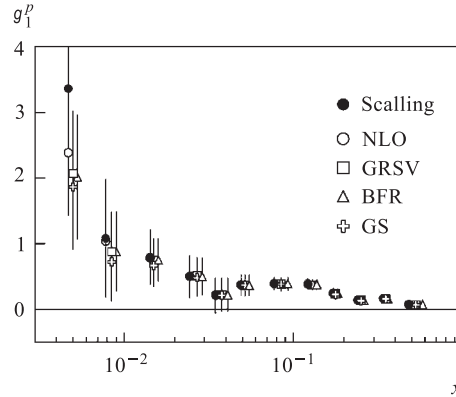
Fig. 19. The structure function g_1^p evolved to $Q_0^2 = 10$ GeV^2 using the assumption that g_1/F_1 is independent of Q^2 (scaling) and using NLO evolutions according to the SMC [43] analysis and those of BFR [106], GRSV [107], and GS [108]

E. Reya, M. Stratmann and W. Vogelsang (GRSV) [107], R. Ball, S. Forte and G. Ridolfi (BFR) [106], and T. Gehrmann and W. Stirling (GS) [108] is shown in Fig. 19 [42]. From this figure one can see that the difference between QCD methods is small compared to experimental errors and the difference between scaling and QCD evolution is significant only at small x. Similar results have been obtained by E154 [71] for g_1^n.

Similar to that of the E154, the E155 has performed the «nonstandard» NLO $\overline{MS}$ fits to all the data using the same assumptions as in [71]. The results of these fits are shown in Figs. 8 and 11 by solid lines. They confirm the results of the more comprehensive «standard» NLO QCD analysis performed by the SMC [44].

Summarizing this paragraph one can note that within the precision of the present experiments the data on g_1 have not shown the apparent Q^2 dependence. This precision is not good enough to demonstrate (as it is done in case of F_2 [6]) the agreement between the observed and predicted Q^2 evolution of g_1. But the agreement between the observed x dependence of g_1 and its QCD inspired para-meterization permits one to conclude that QCD correctly describes the polarization effects in the polarized nucleons and this description can be used in various applications, particularly in cases of extrapolations of data on g_1 to unmeasured regions.

4.2. Tests of the Ellis–Jaffe Sum Rules. To test the Ellis–Jaffe sum rules for protons, neutrons and deuterons one needs to calculate the first moments of the structure function $g_1(x, Q_0^2)$. As it has already been mentioned (see Eq. (1.9)), the contributions to these moments come from three regions: the measured one,

«large-x» extrapolation and «low-x» extrapolation regions:

$$\Gamma_1(Q_0^2) = \int\limits_{x_{\min}}^{x_{\max}} g_1(x, Q_0^2)dx \quad \text{— measured region,}$$

$$+ \int\limits_{x_{\max}}^{1} g_1(x, Q_0^2)dx \quad \text{— «large-}x\text{» extrapolation region,}$$

$$+ \int\limits_{0}^{x_{\min}} g_1(x, Q_0^2)dx \quad \text{— «low-}x\text{» extrapolation region.}$$

The measured regions are typically between $x_{\min} \div x_{\max} = 0.003 \div 0.7$ for SMC experiment and $\sim 0.03 \div 0.8$ for SLAC and HERMES experiments.

The contributions to Γ_1 from the extrapolation regions and their uncertainties are different. The contribution from the large-x extrapolation region is limited by the positivity limit $|A_1(x)| < 1$ and by smallness of $F_1(x \to 1)$. The low-x extrapolation contribution and its uncertainty both depend on the behaviour of $g_1(x \to 0)$ and in principle could be relatively large.

In earlier publications the SMC has assumed that in the large-x region at $x > 0.7$ the asymmetries are flat: $A_1^p(x > 0.7) = 0.7 \pm 0.3$ and $A_1^d(x > 0.7) = 0.4 \pm 0.6$. These assumptions do not exclude that $A_1^{p,d}(x = 1) = 1$.

Usually the low-x extrapolations were performed assuming a Regge type behaviour for $g_1(x \to 0) : g_1(x \to 0) \sim x^{-\alpha}$, $-0.5 < \alpha < 0$, but the starting point of extrapolations was different for SMC and E143. Due to that, relative errors associated with these extrapolations are different in different experiments. Typical examples of contributions to the first moment from the measured and extrapolation regions are given in Table 6.

Table 6. **Typical examples of contributions to Γ_1^p from measured and extrapolation regions**

$\Gamma_1^p(Q_0^2 = 5 \text{ GeV}^2)$		
Regions	SMC	E143
Measured	0.1250(120)	0.1170(70)
Large-x	0.0024(4)	0.0006(2)
Low-x	0.0040(20)	0.0111(20)
Total	0.1310(170)	0.1290(90)
Meas./tot., %	95	91

Table 7. **Contributions to $\Gamma_1(Q_0^2 = 5 \text{ GeV}^2)$ from measured and extrapolation regions evaluated by SMC and E143**

	Measured	
	SMC, $x = 0.003 \div 0.8$	E143, $x = 0.03 \div 0$
p	$0.130 \pm 0.003 \pm 0.005 \pm 0.004$	$0.117 \pm 0.003 \pm 0.006$
d	$0.036 \pm 0.004 \pm 0.003 \pm 0.002$	$0.043 \pm 0.003 \pm 0.02$
n	$-0.054 \pm 0.007 \pm 0.005 \pm 0.004$	$-0.025 \pm 0.007 \pm 0.006$
	Low-x extrapolation	
	SMC, QCD, $x = 0.003 \div 0$	E143, Average $x = 0.003 \div 0$
p	$-0.012^{+0.014}_{-0.025}$	0.012 ± 0.008
d	$-0.015^{+0.010}_{-0.023}$	0.001 ± 0.006
n	$-0.020^{+0.010}_{-0.026}$	-0.010 ± 0.015
	Large-x extrapolation	
	SMC, QCD, $x = 0.8 \div 1.0$	E143, $(1-x)^3$ or flat
p	0.003 ± 0.001	0.001 ± 0.001
d	0.000 ± 0.001	0.000 ± 0.001
n	0.000 ± 0.001	0.001 ± 0.001

The estimated errors of these contributions are indicated in brackets. One can see from this table that the main contribution to Γ_1 comes from the measured region. The total contribution from the regions of extrapolations does not exceed $5(9)\%$ for the SMC (SLAC) experiment.

In the final paper [43] the SMC used the results of the QCD analysis of the data on $g_1(x, Q^2)$ and extrapolated them to unmeasured regions for calculations of $\Gamma_1(Q_0^2)$ (see Table 7). The areas under the QCD fits for $x < 0.003$ in Fig. 18 correspond to the contributions to $\Gamma_1(Q_0^2)$ from the low-x extrapolation regions.

In the final paper [53] the E143 has tried several methods to extrapolate $g_1(x)$ to $x \to 0$ using either the Regge-types behaviour $g_1(x) \sim x^\alpha$, or behaviour in the form $g_1(x) \sim \ln(1/x)$, or parameterization of all existing data on $g_1(x)$. The estimates for contributions to the integral from the region $x = 0.03-0$, $\Delta\Gamma(0.03 \div 0)$, varied from 0.004 to 0.018, the largest one was obtained with parameterization of $g_1(x)$. Finally the average of several estimates was taken for $\Delta\Gamma(0.03 \div 0)$. For the large-$x$ extrapolations the E143 used two methods: (1) assuming $g_1(x) \sim (1-x)^3$ or (2) assuming the asymmetries $A_1^p(x)$ and $A_1^d(x)$ as

Table 8. **Comparison of world data on $\Gamma_1^{p,n,d}$ with the Ellis–Jaffe sum rules**

	Ellis–Jaffe	Experiment	$\langle Q^2 \rangle$	References	
Γ_1^p	0.176±0.006 0.160±0.006	0.126±0.018	11	E80 + E130 + EMC	[33]
		0.136±0.015	10	SMC-93	[36]
		0.127±0.011	3	E143	[49]
		0.112±0.014	5	E154	[71]
		0.120±0.008±0.014	10	SMC Final	[44]
		0.132±0.03±0.09	3	E143 Final	[53]
		0.118±0.004±0.007	5	E155	[75]
Γ_1^n	−0.002±0.005 −0.021±0.018 −0.016±0.006 −0.011±0.005	−0.08±0.055	5	SMC-92 + EMC	[35]
		−0.022±0.011	2	E142	[54]
		−0.031±0.011	2	E142 Revised	[55]
		−0.037±0.014	3	E143	[51]
		−0.055±0.025	5	SMC + EMC + SLAC80/130/142	[48]
		−0.063±0.027	10	SMC-94	[38]
		−0.046±0.025	10	SMC-95	[40]
		−0.056±0.008	5	E154	[71]
		−0.037±0.015	2.5	HERMES	[56]
		−0.078±0.015±0.014	10	SMC Final	[44]
		−0.032±0.018	3	E143 Final	[53]
		−0.058±0.005±0.008	5	E155	[75]
Γ_1^d	0.070±0.004	0.023±0.025	5	SMC-92	[35]
		0.068±0.004 0.042±0.005	3	E143	[51]
		0.034±0.011	10	SMC-94	[38]
		0.041±0.008	10	SMC-95	[40]
		0.026±0.009	5	E154	[71]
		0.019±0.007±0.013	10	SMC Final	[44]
		0.047±0.003±0.06	3	E143 Final	[53]
		0.0288±0.0025±0.0071	5	E155	[73]

almost flat. For both g_1^p and g_1^d the methods gave almost identical $\Delta\Gamma(0.8 \div 1)$: 0.001 for protons and 0.000 for deuterons.

A comparison of contributions to $\Gamma_1(Q^2)$ from the measured and extrapolation regions quoted in the final papers by the SMC [43] and E143 [53] is given in Table 7. As is seen from Table 7, SMC QCD fits gave negative contributions to $\Gamma_1\left(Q_0^2\right)$ from low-x regions for all nucleons and larger errors than that in the Regge case. There is an obvious difference between the SMC and E143 in evaluations of contributions to Γ_1 from the low-x regions. If the QCD approach is correct, the E143 low-x contributions are underestimated. The large-x extrap-
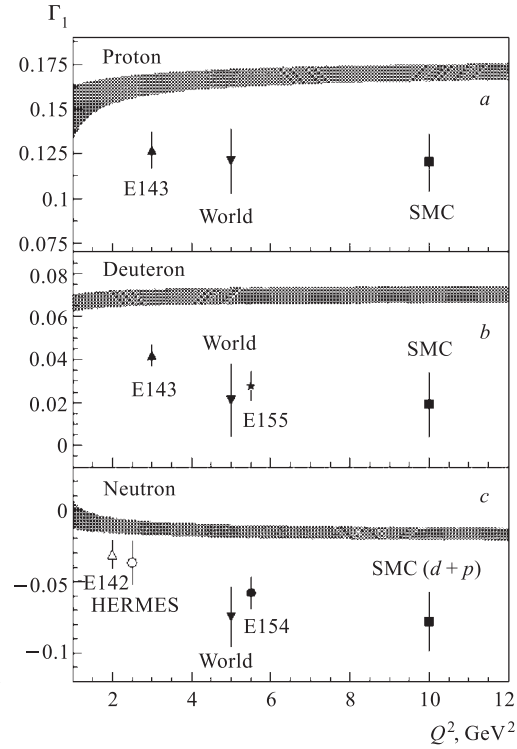
Fig. 20. Comparison of the experimental results on Γ_1 to the prediction of the Ellis–Jaffe sum rules shown by the bands

olations of the SMC and E143 are compatible but the former ones are preferable. In the latest publications of E155 the NLO QCD fits have been also used for extrapolations of data to unmeasured low- and large-x regions.

The data on $\Gamma_1^{p,n,d}$ from different measurements are given in Table 8 as they are quoted in publications and compared with Ellis–Jaffe predictions at average Q^2 of the referred experiments. From this table one can see that all experimental results are compatible and disagree (except E142 for Γ_1^n [54] revized later [55]) with Ellis–Jaffe sum rule predictions by $2 \div 3$ standard deviations.

The Q^2 dependence of the Ellis–Jaffe sum rule for Γ_1 as predicted by Eqs. (1.31), (1.32) is shown in Fig. 20 and compared to some data given in Table 8 and to the combined data at $Q_0^2 = 5$ GeV^2 as calculated by SMC [42]. The disagreement between the data and predictions is clearly seen in this presentation. Quantitatively a comparison of the combined data [42] and world data [44] with predictions is given in Table 9, where for the combined data, statistical and systematic errors are added in quadratures but for the world data statistical, systematic and theoretical uncertainties are given separately. One can see from

Table 9. **Ellis–Jaffe sum rule predictions (theory) compared to the combined [42] and world [44] data on $\Gamma_1^{p,n,d}$ at $Q_0^2 = 5$ GeV^2**

	Γ_1^p	Γ_1^n	Γ_1^d
Combined data	0.141 ± 0.011	-0.065 ± 0.017	0.039 ± 0.006
World	$0.121 \pm 0.003 \pm 0.005\pm$ ±0.0017	$0.075 \pm 0.007 \pm 0.005\pm$ ±0.019	$0.021 \pm 0.004 \pm 0.003\pm$ ±0.016
Theory	0.167 ± 0.005	-0.015 ± 0.004	0.070 ± 0.004

this Table that the difference between the data and predictions on Γ_1^d is more than 5 standard deviations.

The Dubna group [134] has performed a test of the Ellis–Jaffe sum rule for the proton using a parameterization of the virtual photon asymmetries measured by SMC and E143. Assuming that $A_1^p(x = 0) = 0$ and $A_1^p(x = 1) = 1$, two simple parameterizations of $A_1^p(x)$ have been found which cannot be distinguished statistically:

$$A_{1(1)}^p = x^{0.565\pm0.018}, \ \chi^2/DF = 0.95, \tag{4.13a}$$

$$A_{1(2)}^p = x^{0.727\pm0.013}, \ \chi^2/DF = 0.85. \tag{4.13b}$$

The errors of the parameters account for statistical and systematic uncertainties of the experimental data. Using either the first or the second of these parameterizations in Eq. (4.8) instead of experimental values together with parameterizations of F_2 and R, one can calculate $g_1^p(x, Q_0^2)$ and $\Gamma_1^p(Q_0^2)$. These calculations are compared to the theoretical predictions in Fig. 21. Due to substantial reduction of errors the difference between the data and theory is more significant. For instance, the difference between the predicted and combined SMC and E143 data on Γ_1^p is about 9 standard deviations.
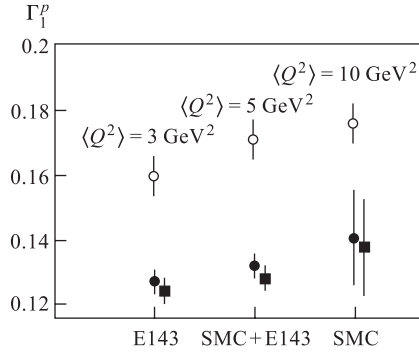

Fig. 21. The first moment of the structure function g_1^p calculated from parameterizations (4.13) of experimental data on asymmetries $A_1^p(x)$ (solid symbols) as compared to the theoretical predictions (open symbols). The solid circles and squares show Γ_1^p calculated with parameterization (4.13a) and (4.13b), respectively. Errors are calculated using the errors of parameterizations

4.3. Determination of Quark and Gluon Contributions to the Spin of Nucleons. Methods to determine quark contributions to the spin of nucleons are outlined in Introduction. Particularly it has been shown that if only 3 flavours (u, d, and s) are active and contribute to the structure functions $g_1^{p,n}$, the first moments $\Gamma_1^{p,n}$ are expressed in terms of matrix elements of the axial vector currents (axial couplings) a_0, a_3, and a_8. For example (see Eqs. (1.24)–(1.28)),

$$\Gamma_1^p(Q_0^2) = \frac{C_1^{NS}(Q_0^2)}{12}\left[a_3 + \frac{1}{3}a_8\right] + \frac{C_1^S(Q_0^2)}{9}a_0(Q_0^2), \qquad (4.14)$$

where a_3 and a_8 are calculated knowing g_A/g_V and F/D. In general:

$$a_u = \frac{1}{6}\left[2a_0(Q_0^2) + a_8 + 3a_3\right], \ a_d = \frac{1}{6}\left[2a(Q_0^2) + a_8 - 3a_3\right],$$
$$a_s = \frac{1}{3}\left[a_0(Q_0^2) - a_8\right]. \qquad (4.15)$$

In QPM the axial couplings a_i, $i = u, d, s$ are associated with contributions of quarks to the nucleon spin: $a_i = \Delta q_i$ and the total quark contribution is equal to $\Delta\Sigma = a_0 = a_u + a_d + a_s$.

The data on $\Delta\Sigma$ and, as a consequence of the Ellis–Jaffe sum rules violation, on Δs are presented in Table 10. SMC used the world data available by 1997,

Table 10. **World data on quark contributions to the nucleon spin**

Source	$\langle Q^2\rangle$	$\Delta\Sigma$	Δs	References	
Γ_1^p	11	0.12 ± 0.17	-0.19 ± 0.06	E80/130 + EMC	[33]
Γ_1^d	5	0.06 ± 0.25	-0.21 ± 0.08	SMC-92	[35]
Γ_1^n	2	0.57 ± 0.11	-0.01 ± 0.06	E142	[54]
	2	0.43 ± 0.12	-0.05 ± 0.06	E142 Revised	[55]
Γ_1^d	3	0.35 ± 0.07	-0.08 ± 0.025	E143 Final	[53]
Γ_1^p	10	0.22 ± 0.14	-0.12 ± 0.06	SMC-93	[36]
Γ_1^p	3	0.27 ± 0.10	-0.10 ± 0.04	E143	[49]
Γ_1^n	3	0.32 ± 0.10	-0.09 ± 0.04	E143 Final	[53]
Γ_1^p	3	0.36 ± 0.10	—	E143	[50]
Γ_1^d	3	0.34 ± 0.05	—	E143	[50]
Γ_1^d	10	0.20 ± 0.11	-0.12 ± 0.04	SMC-94	[38]
Γ_1^d	10	0.30 ± 0.08	-0.09 ± 0.03	SMC-95	[40]
$\Gamma_1^{p,d}$	5	0.20 ± 0.07	—	E154	[71]
$\Gamma_1^{p,d}$	1	0.23 ± 0.19	—	World (SMC)	[44]
Γ_1^d		0.17 ± 0.08	—	E155	[73]
$\Gamma_1^{p,d}$	5	0.23 ± 0.06	—	World (E155)	[75]

Table 11. **Flavor contributions to the spin of the proton**

	Ellis, Karliner [135]	Altarelli, Ridolfi [136]	SMC + all [42]
Δu	0.83 ± 0.03	0.832 ± 0.015	0.82 ± 0.02
Δd	-0.43 ± 0.03	-0.425 ± 0.015	-0.44 ± 0.02
Δs	-0.10 ± 0.03	-0.097 ± 0.018	-0.10 ± 0.02

the E155 has used all the data available by 2000. With QCD corrections all the data are compatible and in the limit of large Q^2 converge to $\Delta \Sigma = 0.3 \pm 0.07$.

Using a slightly different approach to the data selection, Ellis and Karliner [135], Altarelli and Ridolfi [136], SMC [42] and E143 [53] have obtained contributions of different flavors to the spin of the proton (Table 11). Within the errors all the results are compatible. Table 11 shows that the largest contribution to the spin of the proton comes from u quarks. The d- and s-quarks are polarized negatively.

Let us remember that the spin of the proton is built up of several components, the sum of which must be equal to 1/2:

$$S_z^p = \frac{1}{2}\Delta\Sigma + L_q + \Delta g + L_g = \frac{1}{2},$$

where $\Delta\Sigma$ and L_q are contributions from quark spins and orbital momenta, respectively, and Δg and L_g are the same from gluons.

In the naive QPM it is assumed that $\Delta g = L_g = 0$ and $\Delta\Sigma = a_0$. In this model the Ellis–Jaffe sum rules should be valid, from which it follows that $\Delta s = 0$, $\Delta\Sigma \approx 0.6$ and $L_q \approx 0.4$. But we have seen, that the Ellis–Jaffe sum rules are violated, $\Delta\Sigma \approx 0.3$ and $\Delta s \approx -0.1$. So, one should expect large contributions from gluons and orbital momenta. The QCD estimations of these contributions in the context of the generalized parton distribution functions are given by Eq. (1.56).

In QCD gluons are constituents of nucleons and their contribution to the nucleon spin cannot be zero: $\Delta g \neq 0$. The relationship between $\Delta\Sigma$ and a_0 is not trivial either: $\Delta\Sigma \neq a_0$ and it is scheme-dependent. In the Adler–Bardeen normalization scheme an input $\Delta g(Q^2)$ is required to determine $\Delta\Sigma$ from a_0:

$$a_0 = \Delta\Sigma - n_f \frac{\alpha_s(Q^2)}{2\pi}\Delta g(Q^2).$$

So, in this scheme $\Delta\Sigma$ and Δq_i depend on $\Delta g(Q^2)$ (see Fig. 22). From this plot one can see that the naive QPM expectations ($\Delta\Sigma \approx 0.6$, $\Delta s = 0$) correspond to the possible gluon contribution $\Delta g \approx 2$ to the proton spin.

The result on Δg obtained by the SMC from the QCD analysis in AB scheme and quoted in Table 5 as η_g (1 GeV^2) is equal to

$$\Delta g\,(1\ \text{GeV}^2) \equiv \eta_g\,(1\ \text{GeV}^2) = 0.99^{+1.17}_{-0.31}(\text{stat.})^{+0.42}_{-0.22}(\text{syst.})^{+1.43}_{-0.45}(\text{th.})$$
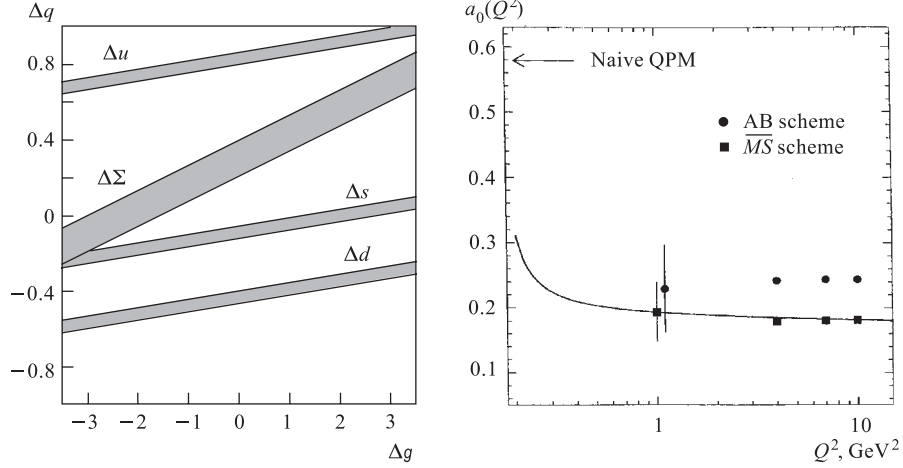
Fig. 22. Quark spin contributions to the proton spin (Δq) as a function of the gluon contribution (Δg) at $Q_0^2 = 5$ GeV^2 in the Adler–Bardeen scheme

Fig. 23. The axial coupling a_0 determined by the SMC from QCD fits using different schemes. The points are determined from fits with different initial $Q_i^2 = 1, 4, 7$ and 10 GeV^2. The solid line is the predicted Q^2-evolution of a_0 in the $\overline{MS}$ scheme. The uncertainties of fits are shown at one point

including statistical, systematic and theoretical uncertainties. The consistent value was also obtained by E155 [75]: Δg (5 GeV^2) $= 1.6 \pm 0.8 \pm 1.1$. The errors are too big to make any conclusion. The more precise data on $g_1(x, Q^2)$ and direct measurements of Δg from semi-inclusive processes are needed.

Figure 23 shows the values of the singlet axial current matrix element $a_0(Q_0^2)$ determined by the SMC [44] from the QCD fits of the world data (Subsec. 4.1) using different schemes.

In the $\overline{MS}$ scheme a_0 is identified with the integral of the singlet quark distribution η_S (Table 5) while in the AB scheme a_0 is calculated from expression

$$a_0 = \eta_S^{AB} - n_f \frac{\alpha(Q^2)}{2\pi} \eta_g^{AB}(Q^2),$$

which is similar to Eq. (4.5) or (1.39). At $Q_i^2 = 1$ GeV^2 from Table 5 it follows:

$$a_0^{\overline{MS}} = 0.19 \pm 0.05(\text{stat.}) \pm 0.04(\text{syst.}),$$

$$a_0^{AB} = 0.23 \pm 0.07(\text{stat.}) \pm 0.19(\text{syst.}).$$

These values are compatible within the errors as it is required for a scheme-independent quantity. The systematic errors in the AB scheme are larger due to

correlations introduced by Δg. As is mentioned above, the difference between the low experimental value of a_0 and its naive QPM prediction could be explained by a large gluon contribution to the nucleon spin. But the value of

$$\eta_S^{\text{AB}} \equiv \Delta\Sigma_{\text{AB}} = 0.38^{+0.03+0.03+0.03}_{-0.03-0.02-0.05}$$

obtained by the SMC [44] from the QCD fit in AB scheme (Table 5) does not support this hypothesis, i.e., it is still significantly below the naive QPM prediction.

The results on the moments of the parton distribution functions obtained in four QCD analyses [109, 110, 71, 44] are compatible. But the treatment of systematic errors is different in different analyses. Particularly, the systematic errors in the analysis [110] are largely underestimated.

4.4. Test of the Bjorken Sum Rule. To test the Bjorken sum rule, one needs to measure $\Gamma_1^p(Q_0^2)$ and $\Gamma_1^n(Q_0^2)$. The SMC for the first time and later on the E143 and E155 experiments obtained these quantities from measurements of $g_1(x)$ with polarized hydrogen and deuterium targets, i.e., measuring Γ_1^p and Γ_1^d. The difference $\Gamma_1^p - \Gamma_1^n$ was calculated using the relation

$$\Gamma_1^p - \Gamma_1^n = 2\left(\Gamma_1^p - \frac{\Gamma_1^d}{1 - 1.5\omega_D}\right). \tag{4.16}$$

The E142 and E154 have tested the Bjorken sum rule measuring Γ_1^n and using Γ_1^p from other experiments. One can perform the test of the sum rule using all available data on Γ_1^p, Γ_1^n, and Γ_1^d listed in Table 10 and accounting for possible correlations of errors.

The conventional method of testing the Bjorken sum rule is to evaluate the difference $\Gamma_1^p - \Gamma_1^n$ and then to compare it with the relation (1.22). Attention should be paid to the method of calculations of Γ_1: if it is calculated using results of QCD fits, the ratio g_A/g_V should not be fixed to the nominal value but left as a free parameter. Otherwise the Bjorken sum rule is assumed in the analysis.

An alternative way to test the Bjorken sum rule, applied for the first time by the SMC [44], is to perform the QCD analysis of the nonsinglet structure function

$$g_1^{NS}(x, Q^2) = g_1^p(x, Q^2) - g_1^n(x, Q^2),$$

which is decouplet from evolutions of $\Delta\Sigma$ and Δg, and to calculate the integral $\Gamma_1^{NS}(Q^2) = \int_0^1 g_1^{NS}(x, Q^2)dx$. This analysis requires less free parameters.

The world data on $\Gamma_1^p - \Gamma_1^n$ are given in Table 12. All the results are compatible and agree with theoretical predictions at the corresponding Q^2.

Table 12. **Bjorken sum rule tests** $\Gamma_1^p(Q^2) - \Gamma_1^n(Q^2)$

Theory	Measurements	$\langle Q^2 \rangle$	Experiments	Ref.
0.191 ± 0.002	0.2 ± 0.065	5	E80/130, EMC, SMC-92	[35]
0.185 ± 0.004	0.163 ± 0.017	5	EMC, SMC-93, E142	[36]
0.171 ± 0.008	0.163 ± 0.025	3	E143	[51]
	0.149 ± 0.014	3	E142 + E143	[49]
	0.160 ± 0.015	3	E142 Revised + E143	[55]
0.186 ± 0.002	0.199 ± 0.038	10	SMC-94	[38]
	0.183 ± 0.033	10	SMC-95	[40]
0.188 ± 0.006	0.171 ± 0.011	5	E154 + E143,	[71]
0.183 ± 0.007	0.146 ± 0.021	2	E142 + EMC	[54]
	0.164 ± 0.023	3	E143 Final	[53]
	$0.174^{+0.024}_{-0.012}$	5	SMC Final + World	[44]
	$0.181^{+0.026}_{-0.021}$	5	SMC, g_1^{NS}	[44]
0.182 ± 0.005	0.176 ± 0.007	5	E155 (World)	[75]
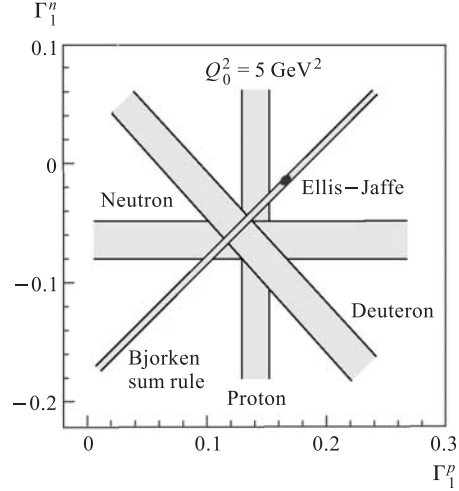
Fig. 24. Comparison of the combined experimental results on Γ_1^p, Γ_1^n, and Γ_1^d to the Bjorken and Ellis–Jaffe sum rules. The Ellis–Jaffe prediction is shown by the black ellipse inside the Bjorken sum rule band

The combined data on $\Gamma_1^p, \Gamma_1^n,$ and Γ_1^d are shown in Fig. 24 together with the Bjorken and Ellis–Jaffe sum-rule predictions. The conservation of the Bjorken sum rule and violation of the Ellis–Jaffe sum rules are clearly seen in this plot.

4.5. Data on Asymmetries A_2 and Structure Functions g_2. The asymmetry A_2 is calculated from measurements of $A_\perp$ and $A_\parallel$ using Eq. (1.9). The results on the proton asymmetry A_2^p of the SMC [37, 42] and E143 [52] are shown in Fig. 25, *a*.
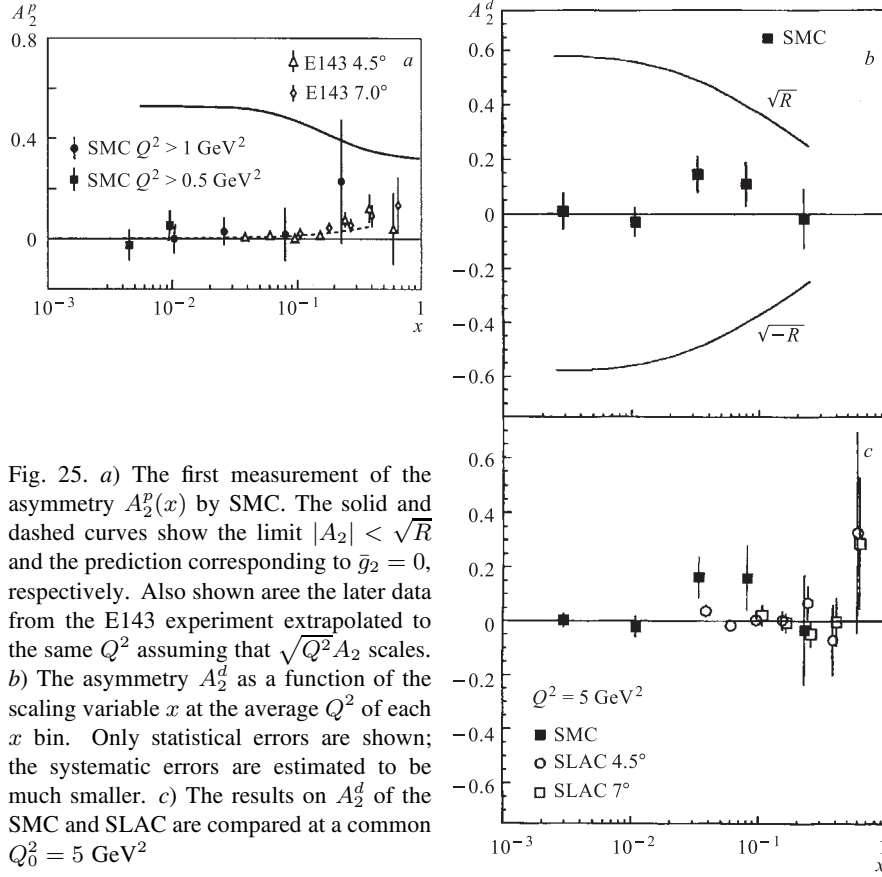
Fig. 25. *a*) The first measurement of the asymmetry $A_2^p(x)$ by SMC. The solid and dashed curves show the limit $|A_2| < \sqrt{R}$ and the prediction corresponding to $\bar{g}_2 = 0$, respectively. Also shown aree the later data from the E143 experiment extrapolated to the same Q^2 assuming that $\sqrt{Q^2}A_2$ scales. *b*) The asymmetry A_2^d as a function of the scaling variable x at the average Q^2 of each x bin. Only statistical errors are shown; the systematic errors are estimated to be much smaller. *c*) The results on A_2^d of the SMC and SLAC are compared at a common $Q_0^2 = 5$ GeV^2

The A_2 is significantly smaller than the $\sqrt{R}$ limit. The results are consistent with $A_2^p = 0$ in the SMC x range ($x > 0.006$) and with the assumption that $\bar{g}_2 = 0$ (dashed line in Fig. 25, *a*). The data of the E143 confirm this observation with a better statistical accuracy for $x > 0.03$.

The results on the deuteron asymmetry A_2^d of the SMC [40] and E143 are shown in Fig. 25, *b, c*. They are consistent between themselves when calculated at the same $Q_0^2 = 5$ GeV^2 and compatible with zero.

The data of E155 [74] and of E143 [53] on A_2^p and A_2^d as a function of Q^2 at various x shown in Fig. 26, *a* indicate that they are Q^2-independent within errors. The averaged over Q^2 values of A_2^p are small and positive in the range $0.2 < x < 0.7$ while A_2^d are around zero (Fig. 26, *b*). The corresponding structure functions $g_2^{p,d}$ are shown in Fig. 26, *c*. The measured values of g_2 are in agreement with Wandzura–Wilczek [158] term g_2^{WW} (Eq. (1.40)) shown by solid lines.
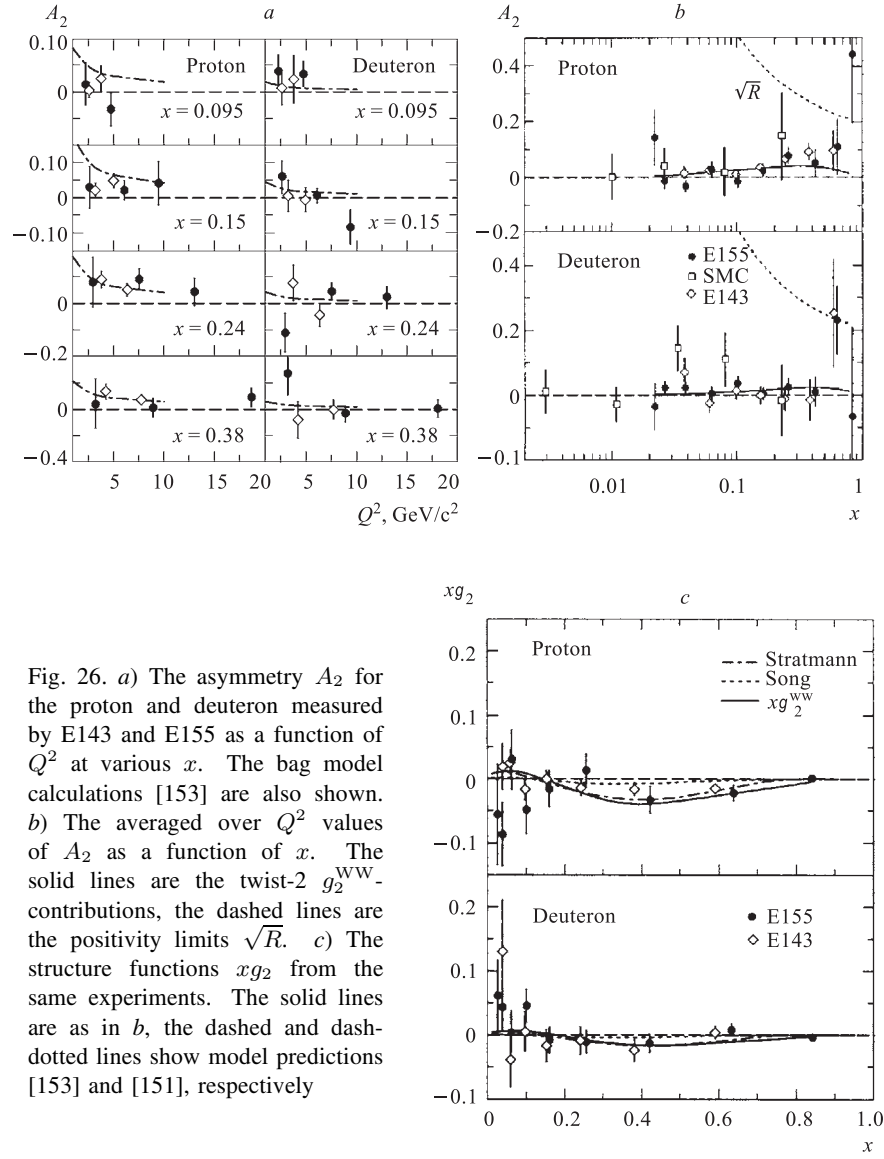
Fig. 26. *a*) The asymmetry A_2 for the proton and deuteron measured by E143 and E155 as a function of Q^2 at various x. The bag model calculations [153] are also shown. *b*) The averaged over Q^2 values of A_2 as a function of x. The solid lines are the twist-2 g_2^{WW}-contributions, the dashed lines are the positivity limits $\sqrt{R}$. *c*) The structure functions xg_2 from the same experiments. The solid lines are as in *b*, the dashed and dash-dotted lines show model predictions [153] and [151], respectively

The data on the neutron asymmetry A_2^n and structure function g_2^n obtained by the E154 and the combined SLAC results [70] on g_2^n are presented in Fig. 27. These results have shown that A_2^n is also small, g_2^n is compatible with the twist-2 g_2^{WW}-predictions (1.40) and the large twist-3 contributions are excluded.
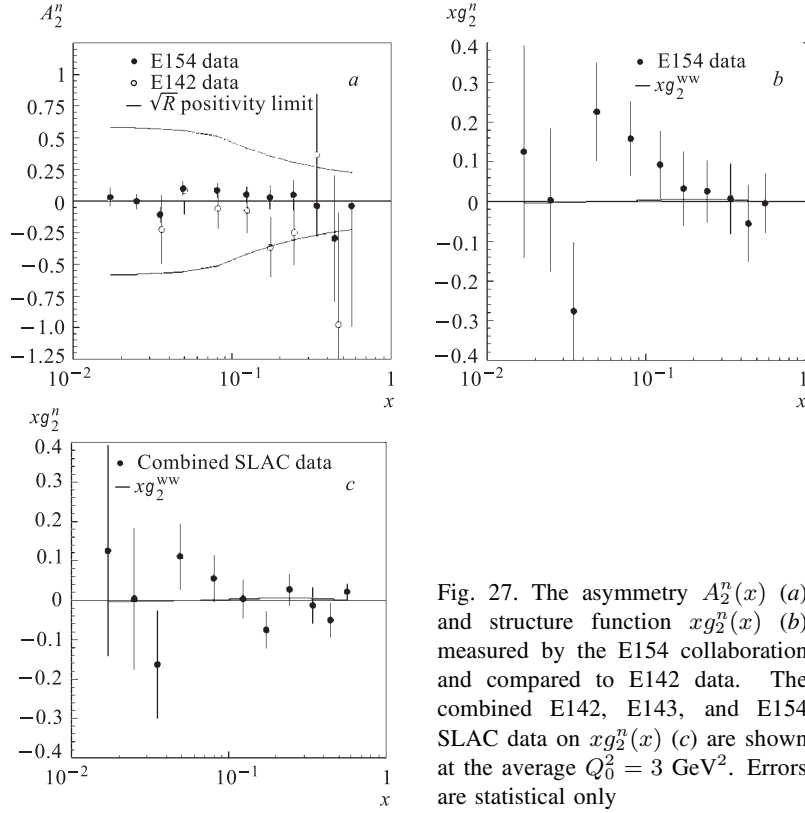
Fig. 27. The asymmetry $A_2^n(x)$ (a) and structure function $xg_2^n(x)$ (b) measured by the E154 collaboration and compared to E142 data. The combined E142, E143, and E154 SLAC data on $xg_2^n(x)$ (c) are shown at the average $Q_0^2 = 3$ GeV^2. Errors are statistical only

The combined SLAC results on the so-called reduced twist-3 matrix element d_2^n and the E143 results on d_2^p and d_2^d calculated as

$$d_2 = \int_0^1 x^2 \left[g_1(x, Q^2) + \frac{3}{2} g_2\left(x, Q^2\right) \right] dx$$

are shown in Table 13 together with theoretical predictions. The data are consistent with zero, but the precision is not sufficient to exclude the models predicting the significant twist-3 contribution.

The Burkhardt–Cottingham sum rule predicts that the first moment of $g_2^p(x)$ should be zero (Subsec. 1.3). This moment was calculated by SMC assuming a constant value of $\sqrt{Q^2} A_2(x)$:

$$-1.0 < \int_{0.006}^{0.6} g_2^p(x) dx < 2.1.$$

Table 13. **Results on the twist-3 contributions to g_2**

	$d_2^n \cdot 10^2$	$d_2^p \cdot 10^2$	$d_2^d \cdot 10^2$	Q^2, GeV^2
SLAC combined [70]	-1.0 ± 1.5	0.54 ± 0.5	0.39 ± 0.92	3.0
X. Song [151]	-0.253	1.76	0.66	5.0
M. Stratmann [153]	0.03	0.6	0.29	5.0
X. Ji et al. [154]	0	—	—	5.0
E. Stein et al. [155]	-3 ± 1	-0.6 ± 0.3	-1.7 ± 0.5	-1.0
I. Balitsky et al. [156]	-2.7 ± 1.2	-0.3 ± 0.6	-1.4 ± 0.6	1.0
M. Gockeler et al. [157]	-0.39 ± 0.27	—	—	4.0

More precise values for Γ_2^p and Γ_2^d have been obtained for combined SLAC data at $Q_0^2 = 5$ GeV^2:

$$\Gamma_2^p = \int_{0.02}^{0.8} g_2^p(x, Q_0^2)\, dx = -0.015 \pm 0.026,$$

$$\Gamma_2^d = \int_{0.03}^{1} g_2^d(x, Q_0^2)\, dx = -0.010 \pm 0.039.$$

The results on Γ_2^n from the E154:

$$\Gamma_2^n = \int_{0.014}^{1} g_2^n(x, Q_0^2)\, dx = 0.19 \pm 0.17 \pm 0.02$$

and from the combined SLAC data:

$$\Gamma_2^n \text{ (combined SLAC)} = \int_{0.014}^{1} g_2^n(x, Q_0^2) = 0.06 \pm 0.15$$

at average $Q_0^2 = 3$ GeV^2 are consistent with zero.

The latest analysis of E155 [76] yields the following results:

$$\Gamma_2^p = -0.044 \pm 0.008 \pm 0.003,$$
$$\Gamma_2^d = -0.008 \pm 0.012 \pm 0.002.$$

Averaging the latest E155 results and E143 data gives:

$$\Gamma_2^p = -0.042 \pm 0.008,$$
$$\Gamma_2^d = -0.006 \pm 0.011.$$

So, the combined SLAC value for Γ_2^p is inconsistent with the Burkhardt–Cottingham sum rule unless there is a specific behavior of the g_2 at $x \to 0$.

For the Efremov–Leader–Teryaev sum rule the SLAC data give $\Gamma_{\mathrm{ELT}} = -0.011 \pm 0.008$ at $Q_0^2 = 5$ GeV^2 which is consistent with (1.42).

Finally, all values on A_2 are significantly smaller than the positivity limit in the measured kinematic range. The data on g_2 are consistent with the twist-2 g_2^{WW}-prediction excluding large twist-3 contributions. The data on g_2 for the proton are inconsistent with the Burkhardt–Cottingham sum rule and all the data are consistent with the Efremov–Leader–Teryaev sum rule but they do not represent conclusive tests of these sum rules because the behaviour of g_2 at $x \to 0$ is not known.

4.6. Tests of the GDH Sum Rule. Except the cases mentioned in Subsec. 1.4, the GDH sum rule for real photons has never been fully tested due to the absence of the circularly polarized light beam in a wide range of energies.

The first most complete tests of the GDH sum rule for virtual photons, i. e., generalized GDH sum rule, were performed by the HERMES using the polarized proton and deuterium targets. Applying different kinematic cuts on W^2, one can test the sum rule in the nucleon resonance region ($1 < W^2 < 4.2$ GeV^2), in the DIS region ($4.2 < W^2 < 45$ GeV^2) and in the whole region ($1 < W^2 < 45$ GeV^2). For the tests of the generalized GDH sum rule HERMES [58] has determined the virtual photon absorption cross section differences ($\sigma_{1/2} - \sigma_{3/2}$) for protons and neutrons as a function of ν in DIS region, $\nu < 23.5$ GeV at different Q^2 between 0.8 and 12 GeV^2, and compared them to other data (Fig. 28).

The corresponding integrals (1.45) $I_{\mathrm{HERMES}}^{\mathrm{DIS}}(Q^2)$ are shown in Fig. 29. They represent DIS components of $I(Q^2)$ for the HERMES kinematic range and agree with estimates (dashed curves in Fig. 28 and 29) based on the assumption that nucleon resonances do not contribute to HERMES and to the data of EMC [33], E143 [52, 53], SMC [41], and E142 [55]. These estimates were obtained using the GRSV parameterization [108] for the asymmetry A_1 derived from NLO QCD analysis. The dashed-dotted curves show the same estimates but for ν up to infinity.

The GDH integrals obtained by the HERMES [63] in a W^2 range $1.0 < W^2 < 45$ GeV^2 wider than the previous one and including the region of nucleon resonances, are shown in Fig. 30 as a function of Q^2. This provides the first experimental determination of the essentially complete GDH integral for the proton. The resonance part of it, $I_{\mathrm{GDH}}^{\mathrm{res}}$, is presented in Fig. 30, *a*. The error bars are statistical. The magnitude of the systematic uncertainties is indicated by the band. The dominant contribution to the systematic uncertainties is due to uncertainties in knowledge of the A_2. This contribution (up to 15 %) was evaluated from the total error quoted for the E143 measurement in the resonance region: $A_2 = 0.06 \pm 0.16$ [53] which is consistent with two possible limits for A_2: $A_2 = 0$ or $A_2 = 0.53\, Mx/\sqrt{Q^2}$. Other contributions to uncertainties are from the beam and target polarizations (5.3 %), from the spectrometer geometry
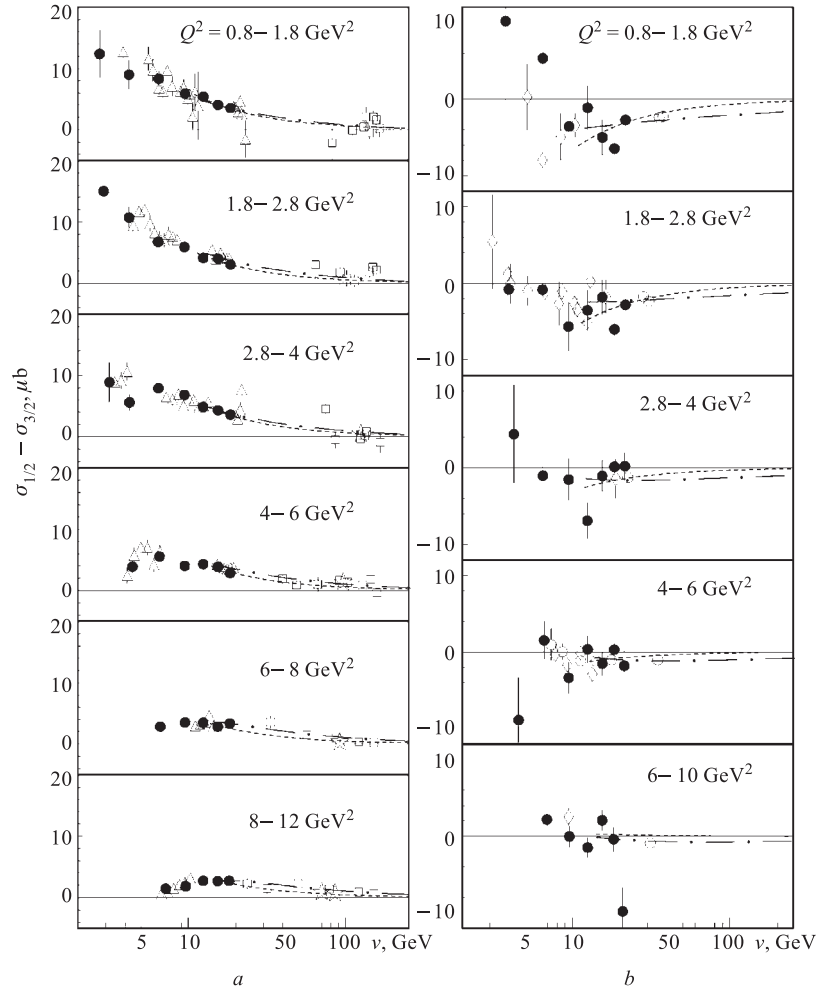
Fig. 28. Virtual photon absorption cross section differences as a function of ν measured in different bins of Q^2 for the proton (a) and the neutron (b). Filled circles are data from HERMES. Open symbols are values derived from other experiments: stars — EMC [33]; triangles — E143 [52]; squares — SMC [41]; diamonds — E142 [55]; circles — E145 [72]. Only statistical uncertaintities are given. The dashed curves are Regge fits to the HERMES data with a cut $W > 4.5$ GeV; the dash-dotted curves show the NLO QCD parameterization [108]
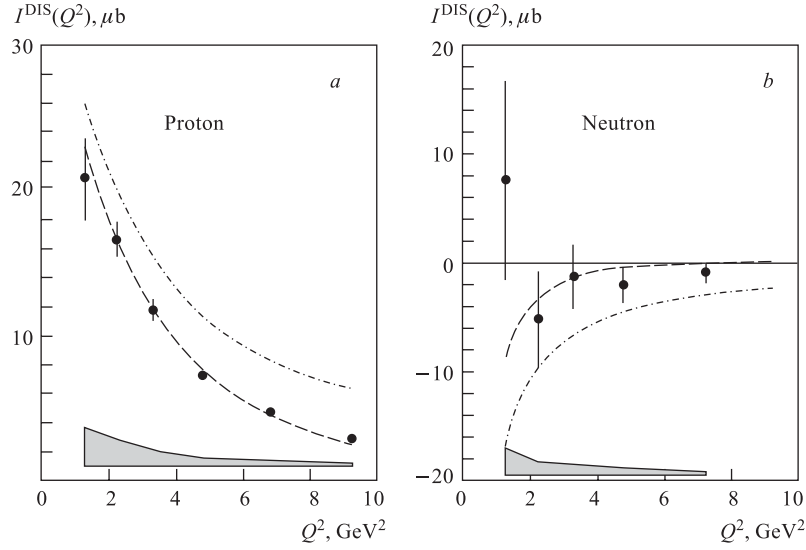
Fig. 29. The generalized GDH integral as a function of Q^2 in the deep inelastic region. The points are $I_{\mathrm{HERMES}}^{\mathrm{DIS}}(Q^2)$ as measured by HERMES in the range $\nu_0 \leq \nu \leq 23.5$ GeV for the proton (a) and for the neutron (b). The error bars show the statistical uncertainties and the bands represent the systematic uncertainties (see text for the explanation of the curves)

(2.5 %), from the combined smearing and radiative effects (up to 10 %) and from the uncertainties of F_2 (2 %). The smearing contribution to the systematic uncertainty was evaluated by comparing the simulated results from two very different assumptions for A_1: a power law ($A_1 = x^{0.727}$) that smoothly extends the DIS behaviour of the asymmetry into the resonance region [134], and a step function ($A_1 = -0.5$ for $W^2 < 1.8$ GeV^2 and $A_1 = 1.0$ for $1.8 < W^2 < 4.2$ GeV^2) suggested by the hypothesis of the possible dominance of the P_{33} resonance at low W^2 and of the S_{11} resonance at higher W^2.

The results for $I_{\mathrm{GDH}}^{\mathrm{res}}$ are compared in Fig. 30, a with two predictions for this integral accounting the contribution of nucleon-resonance excitation: the first one is by Burkert and Li [140], who parameterized the experimental Q^2 evolution of the main nucleon resonances ($P_{33}(1232)$, $P_{11}(1440)$, $S_{11}(1535)$, $D_{13}(1520)$, $F_{15}(1680)$) and assumed single-quark transitions to evaluate the contributions from other resonances (dashed line), and the second one — by Aznauryan [141], described the resonance excitation in the approximation of infinitely narrow resonances and included a contribution from one-pion exchange in the near-threshold
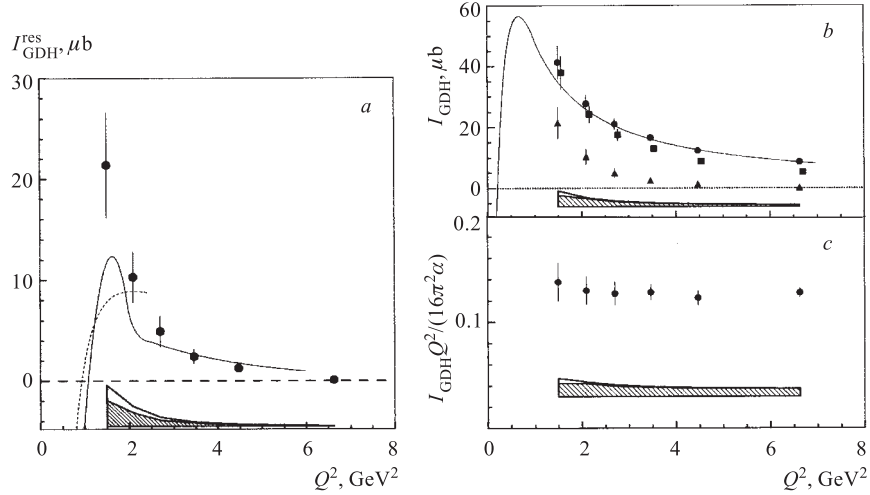
Fig. 30. The generalized GDH integral vs. Q^2 measured by HERMES in the resonance (a) and total W regions (b, c)

region (solid line). The second model qualitatively agrees with the data. Both the models predict a sudden decline in $I_{\text{GDH}}^{\text{res}}$ at Q^2 below 1.5 GeV^2 due to a large negative contribution to it at low Q^2 arising from the helicity structure of the P_{33} resonance. At higher Q^2 the P_{33} resonance magnetic form factor strongly decreases with increasing Q^2 and the positive contribution to $I_{\text{GDH}}^{\text{res}}$ arising from the excitation of higher-mass resonances becomes dominant. Neither of these models includes the nonresonant multihadron production channels which should provide an additional positive contribution to $I_{\text{GDH}}^{\text{res}}$ in the region $W^2 \leqslant 4.2$ GeV^2.

Comparison with the data suggests that at the turn over point $Q^2 \cong 1.5$ GeV^2 the resonance-excitation models are not sufficient to explain the experimental result on $I_{\text{GDH}}^{\text{res}}$. There are other predictions for the resonance-excitation contribution to the generalized GDH integrals but they are limited to the regions of lower Q^2 [142].

To complete the evaluation of the full integral, I_{GDH}, data from the DIS region ($4.2 < W^2 < 45$ GeV^2) were reanalyzed in the same Q^2 bins as for the kinematically more restricted resonance region using the procedure described in [141]. A sample of 1.52 million events was selected to calculate I_{GDH}. Figure 30, b shows the partial integrals $I_{\text{GDH}}^{\text{res}}$ for $W^2 < 4.2$ GeV^2 (triangles) and $I_{\text{GDH}}^{\text{DIS}} + I_{\text{GDH}}^{\text{res}}$ (squares) as a function of Q^2 together with the total GDH integral (circles) containing some estimates of contributions to it from the unmeasured
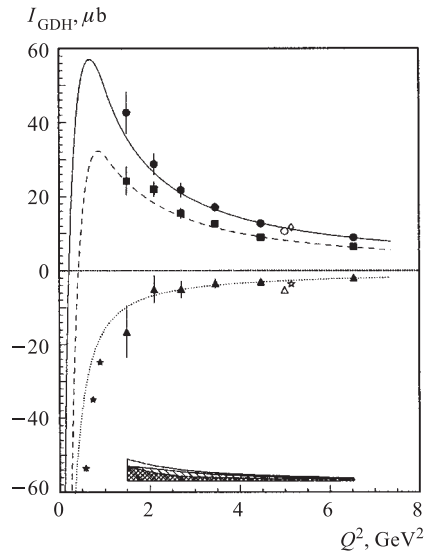
Fig. 31. The Q^2 dependence of the generalized GDH integrals for the deuteron (squares), proton (circles) and neutron (triangles). The curves are the predictions for various targets according to [139]. The error bars represent the statistical uncertainties. The bands represent the systematic uncertainties (open — neutron, lined — deuteron, cross-hatched — proton). The open symbols at $Q^2 = 5$ GeV^2 represent the measurements from [53] (shifted to the left) and [73] (shifted to the right) on proton, deuteron and neutron. The stars represent the three highest Q^2 bins of the measurement from [75]

region $W^2 > 45$ GeV^2. The contribution of the resonance region to the full GDH integral is small for Q^2 values above 3 GeV^2. Figures 30, *b* and 31 show a comparison of the data on I_{GDH} [139] with predictions of the Soffer–Teryaev model [68] based on the Q^2 evolution of the structure functions g_1 and g_2 without consideration of the nucleon-resonance contribution (solid line). These predictions are in good agreement with the experimental data. In the measured energy range the Q^2 dependence of I_{GDH} is consistent with a simple $1/Q^2$ power law. This is demonstrated in Fig. 30, *c* where the results for I_{GDH} are multiplied by $Q^2/(16\pi^2\alpha)$. In the deep inelastic limit this quantity is equivalent to the Γ_1^p (see Eq. (1.45)). The present result on I_{GDH} for protons is in agreement with the measurements of Γ_1^p (see Table 8).

In summary, the Q^2 dependences of the generalized Gerasimov–Drell–Hearn integrals for the proton, deuteron, and neutron are determined by HERMES for the first time in both the nucleon resonance and deep inelastic W^2 regions covering the Q^2 range from 1.2 to 12 GeV^2. In the resonance region the data suggest that for $Q^2 \geqslant 1.5$ GeV^2 the existing resonance-excitation models are not sufficient to fully explain the experimental result on $I_{\text{GDH}}^{\text{res}}$. Above $Q^2 = 3$ GeV^2 the DIS contribution to the generalized GDH integral is dominant. The Q^2 behaviour of I_{GDH} suggests that there are no large effects from either resonances or nonleading-twist and indicates that the sign change of I_{GDH} to meet the real photon limit should occur at Q^2 lower than 1.2 GeV^2.

5. MEASUREMENTS OF SEMI-INCLUSIVE SPIN ASYMMETRIES

5.1. Spin Asymmetries in Production of Charged Hadrons. Asymmetries $A^{+(-)}$ in spin-dependent cross sections for the production of positive (negative) hadrons in semi-inclusive DIS reactions

$$\ell + \mathbf{N} \to \ell' + X + h^{+(-)}$$

are defined as

$$A^{+(-)} = \frac{\sigma_{\uparrow\downarrow}^{+(-)} - \sigma_{\uparrow\uparrow}^{+(-)}}{\sigma_{\uparrow\downarrow}^{+(-)} + \sigma_{\uparrow\uparrow}^{+(-)}},$$

where $\sigma \equiv \sigma(x, Q^2)$ is a lepton-nucleon differential cross section for particular orientation of their spins. Similar to the inclusive asymmetry $A_\parallel$, the asymmetry $A^{+(-)}$ is related to the virtual photon asymmetry $A_1^{+(-)}$.

The first measurement of hadron asymmetries in polarized deep inelastic lepton-nucleon scattering has been performed by the EMC [33] with a longitudinally polarized proton target. In this measurement the hadron asymmetries were determined by the relation:

$$A_{1p}^{+(-)} = \frac{\sigma_{1/2}^{\pm} - \sigma_{3/2}^{\pm}}{\sigma_{1/2}^{\pm} + \sigma_{3/2}^{\pm}},$$

where $\sigma \equiv d\sigma/dz$ and the subscripts refer to the projection of the total angular momentum of the virtual photon-proton system along the incident lepton direction and $z = E_\pi/\nu$. In the naive quark-parton model A_{1p}^{+} is expected to be larger than A_{1p}^{-} because from the helicity conservation the cross section $\sigma_{3/2}^{p}$ is zero and $u(d)$ quarks fragment more readily to $\pi^+(\pi^-)$ mesons, particularly at higher z (see Eqs. (1.13)–(1.16)). Thus, if the $u(d)$ quarks are polarized parallel (antiparallel) to the

Fig. 32. Semi-inclusive spin asymmetries in the charged hadron production by muons on protons measured by the EMC

proton spin, as expected in the naive QPM, A_{1p}^{+} should be larger than A_{1p}^{-} at higher z. The measurement was performed at $z > 0.1$ as a compromise between sufficient statistical accuracy and expected differences between A_{1p}^{+} and A_{1p}^{-}. The results are shown in Fig. 32 where it is seen that both A_{1p}^{+} and A_{1p}^{-} rise with increasing x and the values of A_{1p}^{+} tend to be larger than those of A_{1p}^{-}, consistent with the expectations of the naive QPM.
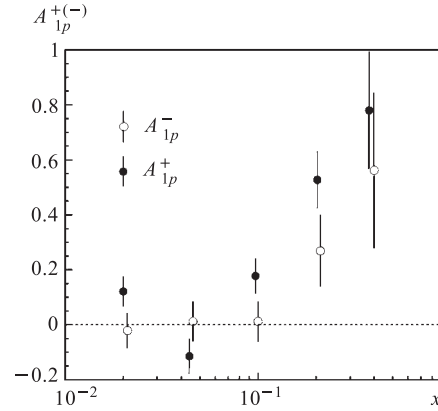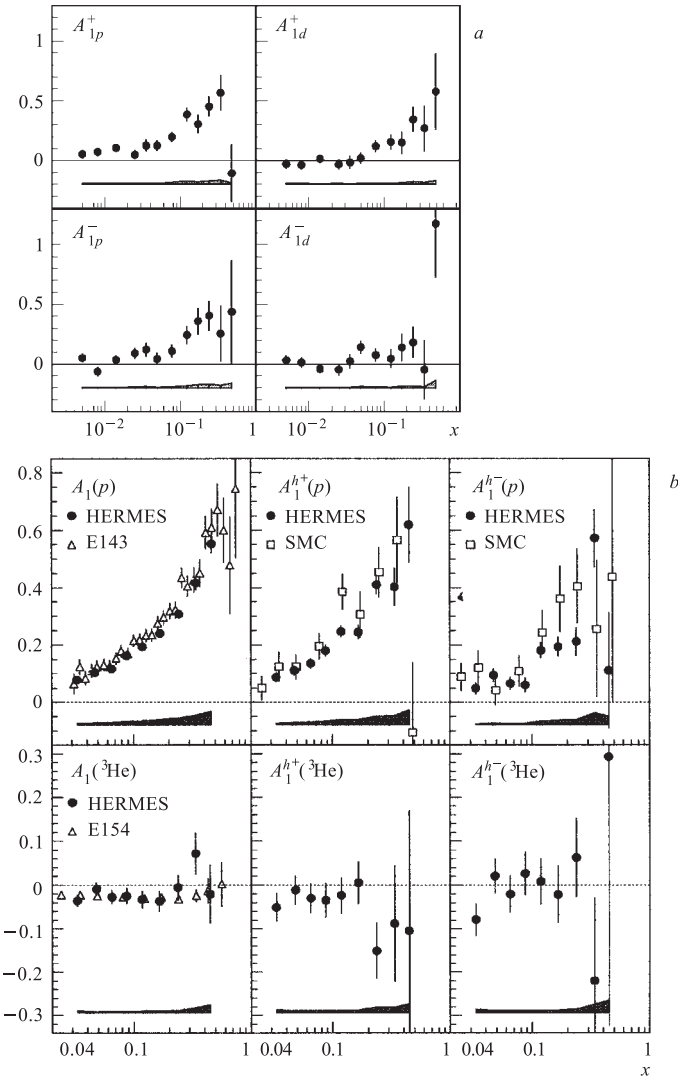
Fig. 33. *a*) Semi-inclusive spin asymmetries in charged hadron production by muon on protons (left side) and deuterons (right side) obtained by the SMC. *b*) Inclusive asymmetries (left side), semi-inclusive asymmetries for electroproduction of positive hadrons (center) and negative hadrons (right side) measured by HERMES. The upper and lower plots are for the hydrogen and ^{3}He target, respectively. Data from other experiments are shown for comparison. The error bars are statistical. The systematic uncertainties are shown by shaded areas everywhere
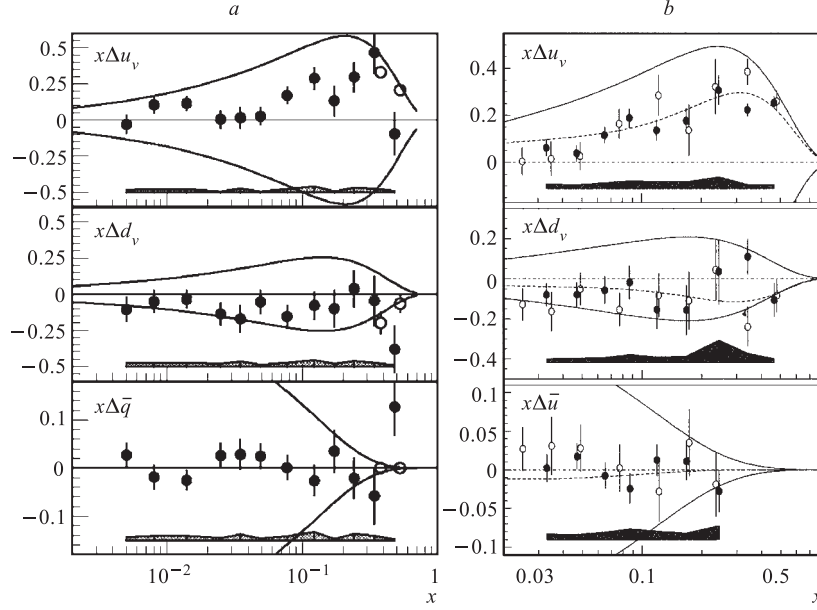
Fig. 34. *a*) The polarized valence and sea quark distributions in the nucleon obtained by the SMC with the assumption $\Delta \bar{u}(x) = \Delta \bar{d}(x)$. The open circles are obtained when the sea polarization is set to zero while the closed circles are without this assumption. *b*) The same distributions measured by HERMES (●). The values obtained previously by SMC (○) in the same x range are shown for comparison. The full lines show the limits defined by spin-independent quark distributions; the dashed lines are the predictions of the Gehrmann–Stirling parameterization [108]. In the bottom plots the curves are $\pm x[\bar{u}(x) + \bar{d}(x)]/2$

The asymmetries $A_{1p}^{+(-)}$ and $A_{1d}^{+(-)}$ for the longitudinally polarized protons and deuterons are also measured by the SMC [39, 46] from about $5 \cdot 10^6 h^+$ and $4 \cdot 10^6 h^-$ in the kinematic domain $x = 0.003{-}0.7$, $\langle Q^2 \rangle = 10$ GeV^2, $z > 0.2$ and $W > 3$ GeV (see Fig. 33, *a*). In QPM these asymmetries can be interpreted in terms of polarized quark distributions Δq and $\Delta \bar{q}$ and fragmentation functions D_f^h and $D_{\bar{f}}^h$ (see Subsec. 1.5). For example,

$$A_{1p}^{+(-)}(x, Q^2) \cong \frac{\sum\limits_{f,h} e_f^2 \left[\Delta q(x, Q^2) D_f^h(Q^2) + \Delta \bar{q}(x, Q^2) D_{\bar{f}}^h(Q^2) \right]}{\sum\limits_{f,h} e_f^2 \left[q(x, Q^2) D_f^h(Q^2) + \bar{q}(x, Q^2) D_{\bar{f}}^h(Q^2) \right]}.$$

One can show that from six measured asymmetries — A_{1p}, $A_{1p}^{+(-)}$, $A_{1d}^{+(-)}$, A_{1d} — it is possible to determine three distributions of the polarized valence
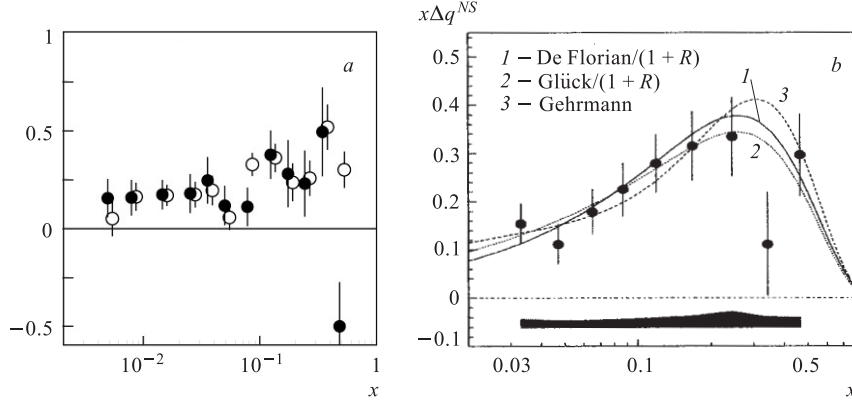
Fig. 35. a) The difference between the spin-dependent structure functions of the proton and the neutron, $6x\left[g_1^p(x) - g_1^n(x)\right]$ (open circles), and the difference between the up- and down-valence quark spin distribution functions, $x\left[\Delta u_V(x) - \Delta d_V(x)\right]$, as determined from SMC semi-inclusive asymmetries under the assumption $\Delta\bar{u}(x) = \Delta\bar{d}(x)$ (closed circles). b) The same difference determined by HERMES from SIDIS asymmetries and compared to parameterization [107, 108, 111] of DIS data. Error bars are statistical only

quarks and nonstrange sea quarks: Δu_V, Δd_V, and $\Delta\bar{q}$ assuming that D_f^h is spin-independent. As is seen from Fig. 34, a, $\Delta u_V(x)$ are positive and increase with x, $\Delta d_V(x)$ are negative and relatively flat in x, and $\Delta\bar{q}(x)$ is consistent with zero. The average relative polarization of the valence quarks $|\Delta q_V/q_V|$ is about 50 %.

In the QPM and with the assumption $\Delta\bar{u}(x) = \Delta\bar{d}(x)$, the quantities $6\left[g_1^p(x) - g_1^n(x)\right]$ and $\Delta u_V(x) - \Delta d_V(x)$ are equal. The former value is obtained from DIS data only while the latter one can be extracted from SIDIS asymmetries alone. The DIS and SIDIS data are in good agreement (Fig. 35, a).

The first moments of the polarized quark distributions are found to be:

$$\Delta u_V = 0.77 \pm 0.10 \pm 0.08,$$

$$\Delta d_V = -0.52 \pm 0.014 \pm 0.09,$$

$$\Delta\bar{q} = 0.01 \pm 0.04 \pm 0.03.$$

The total spin carried by nonstrange quarks is $\Delta\Sigma - 2\Delta\bar{s} = \Delta u_V + \Delta d_V + 4\Delta\bar{q}$ consistent with the value deduced from the first moments of $g_1(x)$ by the SMC [38] and E143 [51].
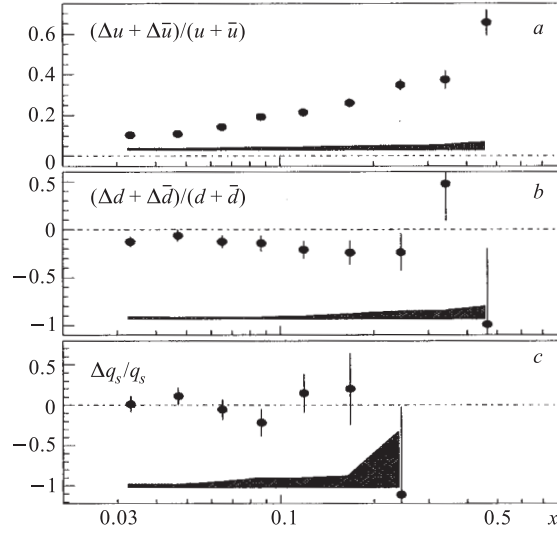
Fig. 36. The relative polarization of up- (*a*), down- (*b*) and sea quarks (*c*) as a function of x (HERMES)

The SMC semi-inclusive asymmetries in production of charged hadrons have been confirmed by HERMES [62] on protons and ^{3}He using $2.3 \cdot 10^6$ and $2.2 \cdot 10^6$ events, respectively, in the kinematic domain $x = 0.023-0.6$, $Q^2 = 1-10$ GeV^2, $z > 0.2$ and $W > 2$ GeV (see Fig. 33, *b*). The agreement of the HERMES data with the SMC data, taken at 6–12 times higher than HERMES Q^2, shows that the semi-inclusive asymmetries are Q^2 independent within the present accuracy of the experiments. Following the procedure described in Subsec. 1.5.1, HERMES has determined the vector **Q** (Eq. (1.47)) defining relative polarizations of quarks under assumption that the polarizations of the strange quarks and total sea are equal: $(\Delta s(x) + \Delta \bar{s}(x)) / (s(x) + \bar{s}(x)) = \Delta q_s(x)/q_s(x)$. For $x > 0.3$ the sea polarization is set to zero and the corresponding effect on the results for the nonsea polarizations is included in their systematic uncertainties. Figure 36 shows the results for $\Delta u/u$, $\Delta d/d$, and $\Delta q_s/q_s$. The up-quark polarizations are positive and the down-quark polarizations are negative over the measured range of x. Their absolute values are the largest at large x. The sea polarization is compatible with zero over the measured range of x. The polarized quark distributions $\Delta q_f(x)$ were determined by forming the products of the polarizations $\Delta q_f(x)/q_f(x)$ and the unpolarized parton distributions from [75] at $Q^2 = 2.5$ GeV^2. The polarizations were assumed to be independent of Q^2 within the Q^2 range of this measurement.

This assumption is justified by the weak Q^2 dependence predicted by QCD and by the experimental results showing no significant Q^2 dependence in the inclusive and semi-inclusive asymmetries.
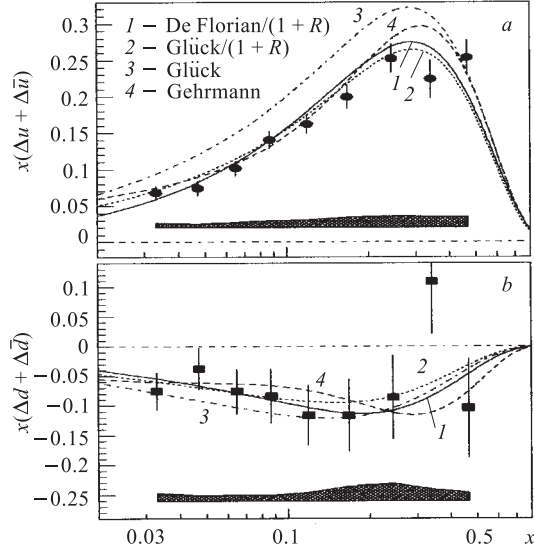
The results for the up- and down-quark distributions are shown in Fig. 37 and compared with different parameterizations of world data [107, 108, 111]. Parameterizations that were fitted to spin asymmetries A_1 under the assumption $R = 0$ do not describe the HERMES data for $x(\Delta u(x) + \Delta \bar{u}(x))$. They can be brought into agreement with the HERMES results dividing the parameterization by $1 + R$. Figure 37 demonstrates the size of this effect for the parameterization from Ref. 107.

Fig. 37. The polarized up- (*a*) and down-quark (*b*) distributions (HERMES) compared to parameterizations of world data on spin-dependent structure functions [107,108,111]

The HERMES and SMC data on polarized valence-quarks and nonstrange sea-quarks distributions are compared in Fig. 34, *b* where the upper plots show the $x\Delta u_V(x)$ and $x\Delta d_V(x)$ derived from the relation $\Delta q_V(x) = (\Delta q(x) + \Delta \bar{q}(x)) - 2\Delta \bar{q}(x)$. Since for scattering off sea quarks, the contribution from $\bar{u}$ quarks dominates, the polarized $x\Delta \bar{u}(x)$ sea distribution is shown in the lower plot. Figure 34, *b* includes results from SMC [38] obtained at $Q^2 = 10$ GeV^2, which are shown here for the x range explored by HERMES and extrapolated to $Q^2 = 2.5$ GeV^2 assuming the Q^2 independence of polarizations $\Delta q(x)/q(x)$.

The SMC [39] and HERMES [67] have tested the alternative method [28] of the analysis of the semi-inclusive asymmetry A_1^{+-} (see Subsec. 1.5.1) for extraction of Δu_V and Δd_V and found the results which are in agreement with the analysis described in Subsec. 1.4.7.

As is mentioned above, in QPM the isospin nonsinglet combination $\Delta q^{NS}(x)$ is directly related to the spin-dependent structure functions g_1:

$$\Delta q^{NS}(x) = \Delta u(x) + \Delta \bar{u}(x) - \Delta d(x) - \Delta \bar{d}(x) = 6(g_1^p(x) - g_1^n(x)).$$

The HERMES result [62] for $\Delta q^{NS}(x)$ is in agreement with the SMC results and with parameterizations of the published inclusive data [107, 108, 111] (see Fig. 35, b).

The measured flavor distributions can be combined into $SU(3)$ singlet $\Delta\Sigma(x, Q^2) = \Delta u(x, Q^2) + \Delta d(x, Q^2) + \Delta s(x, Q^2)$, whose integral $\Delta\Sigma(Q^2) = \int_0^1 \Delta\Sigma(x, Q^2)dx$, defines the total quark contributions to the spin of nucleons. Comparing the HERMES result [62] $\Delta\Sigma = 0.30 \pm 0.04(\text{stat.}) \pm 0.09(\text{syst.})$ with the data collected in Table 8, one can see consistence between DIS and SIDIS results on this value.

The $SU(3)$ nonsinglet combination of the quark distributions $\Delta u(x, Q^2) + \Delta d(x, Q^2) - 2\Delta s(x, Q^2)$ and the axial coupling $a_8(x, Q^2)$ are equal in QPM. The integral $a_8(Q^2) = \int_0^1 a_8(x, Q^2)dx$ can be expressed via hyperon β-decay constants F and D (see Eqs. (1.24)–(1.28)):

$$a_8(Q^2 = 2.5 \text{ GeV}^2) = (3F - D)C_1^{NS} = 0.46 \pm 0.03,$$

where C_1^{NS} is given by Eq. (1.23). The HERMES semi-inclusive results yield $a_8 = 0.33 \pm 0.10(\text{stat.}) \pm 0.11 \text{ (syst.)}$ [62] which is lower than the $SU(3)$ prediction, but still consistent with it within the errors.

5.2. Spin Asymmetries in Production of the High-p_T Hadron Pairs. As is shown in Subsec. 4.3, the gluon contribution to the spin of nucleons estimated from the QCD analysis of $g_1(x, Q^2)$ has a poor precision. The first direct measurement of the gluon polarization in nucleons has been attempted by the HERMES [64]. Selecting events with two hadrons of the opposite charge and with large transverse momentum, HERMES was able to accumulate a sample of events which was enriched by events originating from the process of photon-gluon fusion (see [11]). Requiring the transverse momentum of $p_T^{h_1(h_2)} > 1.5$ (1.0) GeV/c for the first (second) hadron, the subprocess is enhanced where the gluon splitted into two quarks has a hard scale and can be treated perturbatively. The HERMES has estimates from Monte Carlo studies that the average squared transverse momentum of quarks is 2.1 (GeV/c)^2. As long as the fragmentation process is considered to be spin-independent, the spin asymmetry in the production of the quark-antiquark pair is the same as the spin asymmetry of the observed final state with two high-p_T pions, $A_\parallel\left(p_T^{h_1}, p_T^{h_2}\right)$. Remind, that $A_\parallel$ is proportional to the cross-sections difference for longitudinally polarized electrons on longitudinally polarized protons with spins parallel or antiparallel to each other. The spin asymmetry in high-p_T pion-pairs electroproduction is shown in Fig. 38 together with
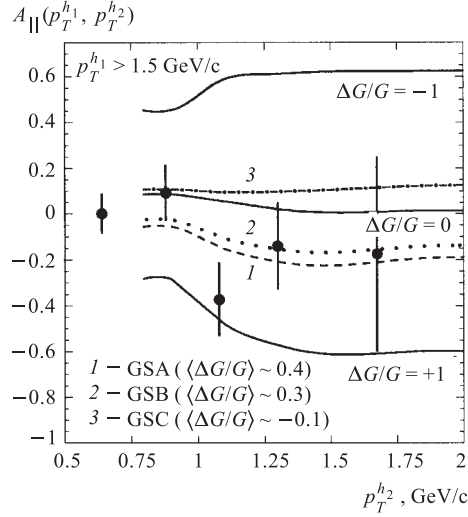
$A_{\parallel}(p_T^{h_1}, p_T^{h_2})$

Fig. 38. The spin asymmetry in high-p_T pion-pairs electroproduction measured by HERMES, as a function of the momentum of second pion, $p_T^{h_2}$, when the first one has a momentum $p_T^{h_1} > 1.5$ GeV/c

Monte-Carlo predictions using various assumptions on polarized parton distributions [56] and on the gluon polarization $\Delta G/G$.

The unique signature of the HERMES results is the negative sign of this asymmetry. Although it is affected by background processes, all of them have a positive asymmetry, since they are dominated by the positive polarization of up-quarks in the proton. The observed negative asymmetry can by explained by significant positive gluon polarization. The change of sign comes from the negative analyzing power of the photon-gluon fusion diagram. Using PYTHIA for background Monte Carlo generator, HERMES has obtained a value of the gluon polarization of $\Delta G/G = 0.41 \pm 0.18 \pm 0.03$ at a mean $x_G = 0.17$. But, unfortunately, the Monte-Carlo sample does not agree with the data and due to that the systematic error on $\Delta G/G$ seems to be underestimated.

Continuation of the analysis see in [58]. So, the quantitative result on $\Delta G/G$ depends critically on the detailed theoretical understanding of the background processes.

5.3. Single-Spin Azimuthal Asymmetries in DVCS. Single-spin azimuthal asymmetries (SSAA) can appear in the reactions either with a polarized lepton and unpolarized targets or with an unpolarized lepton and polarized targets, i.e., with one polarized particle in the initial state. As is outlined in Subsec. 1.5.4, the interest to such reactions has been triggered by introduction of Generalized Parton Distribution (GPD) functions and possibilities to measure them in exclusive channels $\ell p \to \ell' p' \gamma$ (DVCS) and $\ell p \to \ell' p' \pi^0(\rho, \eta)$. The results of the DVCS studies have been reported by HERA detectors ZEUS [79] and H1 [80] at high energies and by HERMES [81] and CLAS (TJNAF) [82] at lower energy.

The results of the ZEUS [79] have been obtained in the kinematic region $Q^2 > 6$ GeV^2 and $0.0005 < x < 0.01$ and compared to the Monte-Carlo simulations. The Monte-Carlo generator GenDVCS [15] based on the formulae given in [119] has been written to simulate the DVCS process. The generator allows one to perform separately the simulation of the DVCS and QED Bethe–Heitler (BH)

processes, or the combination of DVCS, BH and their interference. The results can be summarized as follows:

- the significant excess in the number of low polar angle photons above that expected from the QED process is observed;
- the analysis of the shower shapes has indicated that the potential background from hadron production of (π^0/η) is small and cannot account for the observed excess;
- the data are in reasonable agreement with the leading order prediction for DVCS from Ref. 119, seen in the MC-data comparison.

A signal of DVCS has been also observed at H1 [80]. Cross sections of the reaction $e^+p \rightarrow e^+p\gamma$ as a function of Q^2 and W have been measured in the kinematic range: $2 < Q^2 < 20$ GeV^2, $|t| < 1$ GeV^2 and $30 < W < 120$ GeV. The data are compared separately with the BH prediction and with the full simulations including BH, DVCS and their interference using the same MC generator as ZEUS. The description of the data by such simulations is good enough, both in shape and in absolute normalization.

The HERMES has obtained the first experimental results [81] on the SSAA in DVCS using two different beam helicity states of polarized positrons and unpolarized hydrogen target. This asymmetry allows one to access the imaginary part of DVCS as is seen from Eq. (1.57).

The SSAA in the reaction $ep \rightarrow e'p'\gamma$ versus azimuthal angle ϕ between the real and virtual photons in the laboratory frame was defined as follows:

$$
A_L = \frac{\displaystyle\int_0^\pi d\phi(d\sigma^+ - d\sigma^-) - \int_\pi^{2\pi} d\phi(d\sigma^+ - d\sigma^-)}{\langle|P_B|\rangle \displaystyle\int_0^{2\pi} d\phi(d\sigma^+ + d\sigma^-)},
$$

where the $+$ and $-$ superscripts refer to the beam helicity and $\langle|P_B|\rangle$ is the average beam polarization. For a $\sin\phi$-weighted moment this equation becomes:

$$
A_{LU}^{\sin\phi} = \frac{2\displaystyle\int_0^{2\pi} d\phi(d\sigma^+ - d\sigma^-)\sin\phi}{\langle|P_B|\rangle \displaystyle\int_0^{2\pi} d\phi(d\sigma^+ + d\sigma^-)}.
$$

The detected events correspond to the reaction $ep \rightarrow e'\gamma X$. Scattered protons, p', have been identified by software methods calculating missing mass
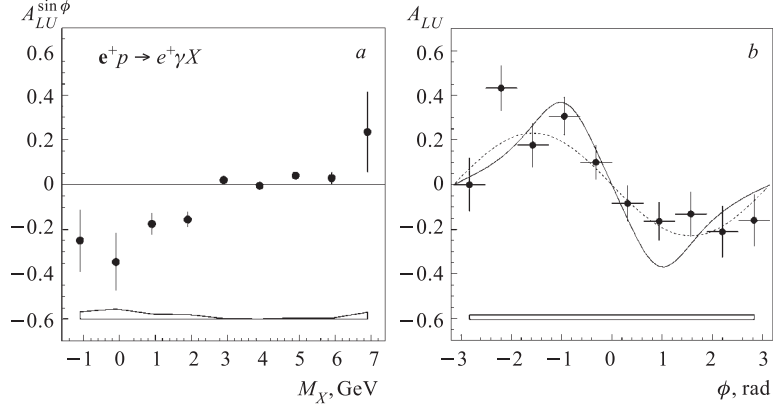
Fig. 39. The $\sin\phi$-weighted single spin azimuthal asymmetry $A_{LU}^{\sin\phi}$ for γ from reaction $ep \to e'X\gamma$ versus the missing mass X (*a*) and the single spin azimuthal asymmetry A_{LU} versus the azimuthal angle ϕ of γ (*b*), where the dashed curve represents the $\sin\phi$ dependence with the amplitude of 0.23 and the solid curve represents the results of the model calculations [84]

M_X and selecting events in the M_X range around the proton mass. The kinematic range was as follows: $M_X = 0.4-1.4$ GeV, $W > 4$ GeV, $Q^2 > 1$ GeV^2 and $\nu > 24$ GeV. The wide enough interval for M_X was selected due to a bad resolution. Figures 39, *a, b* show the $\sin\phi$-weighted asymmetry $A_{LU}^{\sin\phi}$ versus M_X and versus azimuthal angle ϕ between the real and virtual photons, respectively. The azimuthal dependence of the SSAA was fitted by the function $P1 + P2\sin\phi$ with the parameter $P2 = 0.23 \pm 0.04 \pm 0.03$.

DVCS has been also observed by the CLAS Collaboration at TJNAF, USA in the reaction $ep \to e'p'\gamma$ with longitudinally polarized electrons, 4.25 GeV, and the unpolarized proton target [82]. The reaction was identified by analyzing missing mass squared distributions from $ep \to e'p'X$:

$$M_X^2 = (\nu + M - E_p)^2 - (q - \mathbf{P}_p)^2,$$

where ν and q are the virtual photon energy and momentum; E_p and $\mathbf{P}_p$ are the energy and momentum of the recoil proton and M is the proton mass.

The main background to the single photon in a final state comes from π^0 production. The number of single photon events for each beam polarization and for the certain kinematic bin has been determined using the fitting and subtraction techniques. The fitted numbers of events are used to determine an azimuthal

Fig. 40. The ϕ dependence of the single spin azimuthal asymmetry A in electroproduction of the real photons: $ep \to e'p'\gamma$ measured by the CLAS [82]. The error bars are statistical. The dark shaded region is the range of fitted $A(\phi)$ defined by the statistical errors of parameters a and b, the light shaded region includes systematic uncertainties added linearly. The curves are model calculations referred to in the text
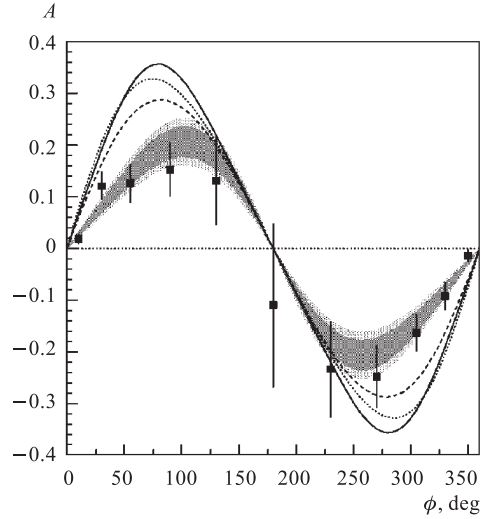
asymmetry A:

$$A = \frac{1}{P_e} \frac{(N_\gamma^+ - N_\gamma^-)}{(N_\gamma^+ + N_\gamma^-)}.$$

For each ϕ bin, where ϕ is an angle between the lepton and hadron planes, the data have been integrated in the region of Q^2 from 1 to 1.75 GeV^2 and $-t = 0.1$ to 0.3 GeV/c. The asymmetry A as a function of ϕ is shown in Fig. 40 together with the fit function $A(\phi) = a \sin \phi + b \sin 2\phi$. The fitted parameters are $a = 0.202 \pm 0.028$(stat.)± 0.013(syst.) and $b = -0.024 \pm 0.021$(stat.)± 0.00(syst.). The last parameter is consistent with zero within the errors.

The curves shown in the same figure are the model calculations [114–116]. None of the models agrees with the data. Comparing results presented in Figs. 39 and 40 one can see that they agree within the errors on the amplitude of modulation and shifted in ϕ by about 180°. This is, probably, due to different definitions of the angle ϕ.

5.4. Azimuthal Asymmetries in Hadron (Pion) Electroproduction and Transverse Spin Effects. The transverse polarization component of the nucleon spin is a subject of further studies in the polarized DIS. Corresponding structure functions are defined in Subsec. 1.5.5. One of them is the transversity which is still unmeasured.

The SMC has presented [47] the first preliminary data on the semi-inclusive DIS hadron production from the transversely polarized targets. It is analyzed in terms of the Collins angle ϕ_c. The preliminary results on the azimuthal asymmetry in distributions of positive hadrons (π^+) produced on the polarized proton and deuteron targets, have been obtained. The asymmetry, A_h, has been obtained

from the measured one, ε_h, after weighting it with a factor of $P_t f D_{NN}$:

$$A_h = \frac{1}{P_t f D_{NN}} \varepsilon_h, \quad \varepsilon_h = \frac{1}{\langle \sin \phi_c \rangle} \frac{N(\phi_c) - N(\phi_c + \pi)}{N(\phi_c) + N(\phi_c + \pi)},$$

where P_t is the target transverse polarization; f is the dilution factor and D_{NN} is the transverse depolarization factor. The results were fitted by $A_h = (C + A_N \sin(\phi_c))$. The nonzero value $A_N^+ = 11 \pm 6\%$ has been found for positive pions produced on protons whereas the negative pions yield $A_N^- = -2 \pm 6\%$ which is consistent with zero. For the deuteron target A_N is small for both π^+ and π^-. Although the statistical precision is limited, indications on possible transverse spin effects are observed at the level of two standard deviations for π^+ produced on protons.

Related to the transversity, some distribution functions can be measured via single-spin asymmetries in certain lepton and hadron experiments [20, 21–24], where only the beam or target are polarized longitudinally. Although in the simplest models the single-spin asymmetries are expected to vanish at the level of «twist-2», they have been observed in some hadron-hadron experiments [85] at relatively small p_T where these asymmetries could arise due to «higher twist» effects.

In the case of semi-inclusive pion electroproduction from longitudinally polarized nucleons, chiral-odd quark spin distribution functions closely related to the transversity can be measured [19]. In such experiments the Collins angle becomes the azimuthal angle ϕ of the pion around the virtual photon direction with respect to the lepton scattering plane (see Fig. 2, b).

Azimuthal asymmetries in the semi-inclusive DIS pion production have been studied for the first time by the HERMES experiment [59] using both unpolarized beam and longitudinally polarized hydrogen target (A_{UL}) and polarized positron beam and unpolarized target (A_{LU}). The kinematic cuts on the scattered positrons were $1 < Q^2 < 15$ GeV^2, $W > 2$ GeV, $0.023 < x < 0.4$, $0.2 < z < 0.7$, and $y < 0.85$. Pions were identified in the energy range $4.5 < E_\pi < 13.5$ GeV. The limit $p_T > 50$ MeV was applied to the pions to allow an accurate measurement of the angle ϕ (see Fig. 2, b). Single-spin asymmetries are evaluated as follows:

$$A_{LU(UL)}^W = \frac{\frac{L^\uparrow}{L_P^\uparrow} \Sigma_{i=1}^{N\uparrow} W\left(\phi_i^\uparrow\right) - \frac{L^\downarrow}{L_P^\downarrow} \Sigma_{i=1}^{N\downarrow} W\left(\phi_i^\downarrow\right)}{\frac{1}{2}\left[N^\uparrow + N^\downarrow\right]},$$

where the $\uparrow / \downarrow$ denotes positive/negative helicity of the beam (target). Each summation is over the number $N^{\uparrow/\downarrow}$ of selected events involving a detected pion for each beam (target) spin state corresponding to the dead-time corrected luminosities $L^{\uparrow/\downarrow}$ and $L_P^{\downarrow/\uparrow}$, the latter being averaged with the magnitude of the beam/target
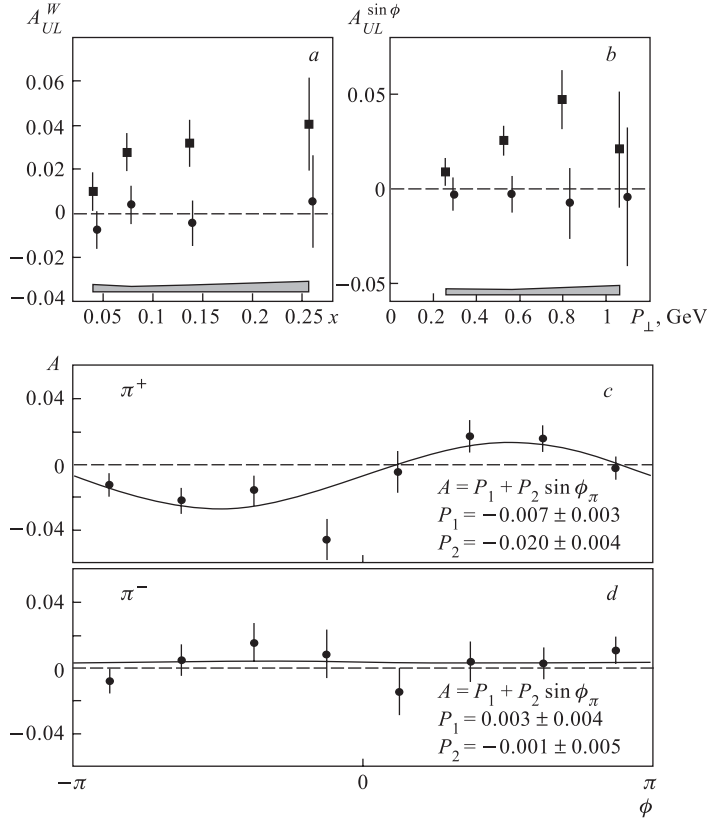
Fig. 41. Single-spin asymmetries for π^+ and π^- from reaction $e^+ p \to e^+ \pi^\pm X$ measured by the HERMES with unpolarized positrons and polarized protons: $A_{UL}^{\sin \phi}$ (squares) and $A_{UL}^{\sin 2\phi}$ (circles) as a function of Bjorken x (a); asymmetry $A_{UL}^{\sin \phi}$ as a function of transverse momentum for π^+ (squares) and π^- (circles) (b); and asymmetry A_{UL} for pions versus the azimuthal angle ϕ (c, d). Error bars show the statistical uncertainties and the bands represent the systematic uncertainties for $A_{UL}^{\sin \phi}$

polarization. The weighting functions $W(\phi) = \sin \phi$ and $W(\phi) = \sin 2\phi$ are expected to provide sensitivity to the Collins fragmentation function [20] in combination with different spin distribution functions [16, 17]. Asymmetries were integrated over the spectrometer acceptance in the kinematic variables y and z. Corrections were applied for the effects of the spectrometer acceptance, based on a Monte Carlo simulation. The values of $A_{UL}^{\sin \phi}$, $A_{UL}^{\sin 2\phi}$, and $A_{LU}^{\sin \phi}$ were extracted from the data. In Fig. 41, a the $A_{UL}^{\sin \phi}$ and $A_{UL}^{\sin 2\phi}$ values obtained for
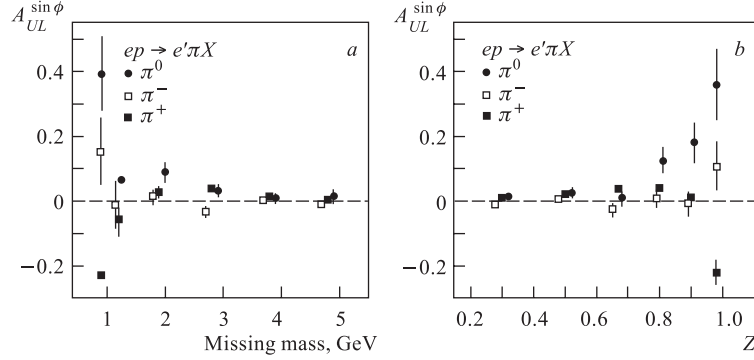
Fig. 42. The single-spin azimuthal asymmetry $A_{UL}^{\sin\phi}$ versus missing mass (M_X) for the pion production from reaction $e^+p \to e'\pi X$ (a) and the same asymmetry versus z (b)

π^+ are shown as a function of x, after averaging over p_T. In the HERMES kinematic domain which covers a range of relatively low Q^2 and moderate p_T, the ratio $A_{UL}^{\sin 2\phi}/A_{UL}^{\sin\phi}$ is predicted to be small in the valence quark region [25]. The data are consistent with such expectations. Data also show an apparent increase of $A_{UL}^{\sin\phi}$ with increasing x. This behaviour is in agreement with existing interpretation of single-spin asymmetries as being associated with valence quark contributions [26, 27]. In Fig. 41, b the $A_{UL}^{\sin\phi}$ averaged over x is plotted for π^+ and π^- as a function of transverse momentum.

The mean $\langle Q \rangle$ is about 1.55 GeV for all bins. There is an indication that $A_{UL}^{\sin\phi}$ increases with increasing p_T for π^+ while it is consistent with zero for π^- at all p_T. This behaviour can be related to the dominant role of the intrinsic quark transverse momentum when p_T remains below a typical value ~ 1 GeV/c [16–18]. The averaged over x and p_T values of asymmetries $\langle A_{UL}^{\sin\phi} \rangle$ are $0.022\pm0.005\pm0.003$ for π^+ and $-0.002\pm0.006\pm0.04$ for π^-. The averaged over x and p_T asymmetries $\langle A_{UL}^{\sin 2\phi} \rangle$ and $\langle A_{LU}^{\sin\phi} \rangle$ are consistent with zero for π^+ and π^-.

The ϕ dependence of the single-spin asymmetries A_{UL} for π^+ and π^- is shown in Fig. 41, c. A clear $\sin\phi$ dependence is observed for π^+. No such behaviour is seen for π^- within the errors. Similar analysis was performed for π^0 production [60]. The π^0 data are close to that of the π^+ (not shown in Fig. 41, c).

The difference between the π^+ and π^- asymmetries can be interpreted in QPM. The asymmetry for π^+ produced on protons is dominated by scattering from the up-quarks which are more abundant in the proton while the π^- asymmetry is dominated by scattering from down-quarks which are less abundant in the proton and the π^0 asymmetry is closer to that of the π^+ because it receives contributions from both up- and down-quarks.

Figures $42, a, b$ show the asymmetries $A_{UL}^{\sin \phi}$ for π^+, π^-, and π^0 versus missing mass of reaction $ep \rightarrow e'\pi X$ and versus z, respectively [61]. The asymmetry for π^+ as a function of the missing mass changes the sign in the region of masses around 1.5 GeV while the asymmetry for π^0 decreases with increasing missing mass and for π^- the asymmetry remains small. The asymmetries as a function of z remain small at $z < 0.7$ and grow rapidly in magnitude at $z \geqslant 0.8$.

6. SUMMARY AND PROSPECTS

1. Following the pioneering experiments by SLAC E80/130 and EMC collaborations, the spin-dependent structure functions g_1^p of the proton and additionally g_1^n of the neutron and g_1^d of the deuteron have been measured by the SMC, SLAC E142/143/154/155 and HERMES collaborations in the kinematic domain $x = 0.003 \div 0.8$, $Q^2 = 1 \div 60$ GeV^2. The first moments of $g_1^{p,n,d}$ and g_1^{NS} have been determined and used for tests of the Ellis–Jaffe and Bjorken sum rules.

2. The Ellis–Jaffe sum rules violations have been observed by all experiments within $3 \div 5$ standard deviations.

3. The Bjorken sum rule is confirmed by all existing data on spin-dependent structure functions g_1^p and g_1^n.

4. The data on the first moments of $g_1^{p,n,d}$ are used to determine contributions of the nucleon constituents to the spin of nucleons. The total quark contribution to the nucleon spin and contributions of u-, d-, and s quarks to it are determined. The original observation of the EMC has been confirmed with better accuracy: quarks contribute little to the spin of nucleons.

5. Possible gluon contributions to the nucleon spin have been estimated from QCD evolutions of $g_1^p(x, Q^2)$, $g_1^d(x, Q^2)$, and $g_1^n(x, Q^2)$ with poor accuracy. Contributions to the nucleon spin from gluons and orbital momenta of constituents are to be identified and measured directly in future experiments and first of all in COMPASS at CERN. The main goal of the COMPASS experiment is to measure for the first time a gluon contribution to the nucleon spin studying the semi-inclusive asymmetries in the production of open charm particles.

6. The QCD tests of structure functions $g_1(x, Q^2)$ have been performed. Although the precision of the experimental data is not good enough to test the direct QCD prediction on Q^2 behaviour of the g_1, the evolution of the QCD inspired x dependence of g_1 agrees with QCD expectations. The QCD running constant $\alpha_s(Q^2)$ determined from polarized experiments is in agreement with unpolarized data. With the improved statistical accuracy and extension of Q^2 range planned by COMPASS, the QCD analysis of g_1 can be one of the most precise methods of α_s determination.

7. The second spin-dependent structure function $g_2(x, Q^2)$ has been measured. The values of g_2 are found to be small and consistent with theoretical

predictions accounting the twist-2 contributions to it. No large twist-3 contributions are seen in the experiment. The g_2 sum rules have not been fully tested because the small x behaviour of g_2 is not known.

8. The generalized Gerasimov–Drell–Hearn sum rule for virtual photons, $I_{\mathrm{GDH}}(Q^2)$, has been tested in the Q^2 range from 1.2 to 12 GeV^2 and found to be consistent with theoretical models.

9. Inclusive spin-dependent effects have been confirmed and complimented by the spin-dependent effects observed in semi-inclusive deep inelastic (SIDIS) processes. New spin-dependent asymmetries in SIDIS — azimuthal asymmetry in production of hadrons (pions) on transversely and longitudinally polarized targets — are observed. Further studies of these asymmetries will give information on the role of different flavors in the nucleon spin structure.

10. A new field in the nucleon spin structure has been opened by studies of spin effects in exclusive deep inelastic processes and, particularly, in the simplest one — Deeply Virtual Compton Scattering (DVCS), associated with new Generalized Parton Distribution (GPD) functions accounting for participation of all nucleon constituents in the nucleon spin build up. Azimuthal asymmetries in production of real photons via DVCS are observed. This is the beginning of a new era in nucleon structure studies similar to that started in 1970s by SLAC DIS experiments.

The pioneering experiments in DVCS studies are HERMES and CLAS. There is a suggestion [192] to include DVCS in the COMPASS program and apparatus upgrade.

The HERMES collaboration at HERA continues to take data by using the polarized and unpolarized positron beams and polarized and unpolarized pure gas hydrogen and deuterium targets. Due to a very good particle identification system, HERMES will measure semi-inclusive and exclusive spin-dependent asymmetries including that in DVCS.

At the upgraded COMPASS one can study the Q^2, x, ϕ, and t dependence of asymmetries in exclusive reaction $\mu p \to \mu' p' \gamma'$ and obtain an access to GPD measurements.

12. Future experiments on the spin physics are planned at RHIC BNL by STAR and PHENIX.

It is obvious that the spin structure of the nucleon will be an active field of research during next years to come.

REFERENCES

Literature on Deep Inelastic Scattering and Quark Parton Model

1. *Feynman R. P.* Photon-Hadron Interactions. Redwood City: Addison Wesley Publ. Co., 1989.

2. *Close F. E.* An Introduction to Quarks and Partons. London; N. Y.: Academic Press, 1979.

3. *Ioffe B. L., Khoze V. A., Lipatov L. N.* Hard Processes. Amsterdam: North-Holland, 1984.

4. *Halzen F., Martin A. D.* Quarks and Leptons. N. Y.: John Wiley and Sons, 1984.

5. *Roberts R. G.* Structure of the Proton: Deep Inelastic Scattering. Cambridge: Cambridge University Press, 1990.

6. *Hagiwara K. et al.* // Phys. Rev. D. 2002. V. 66. P. 010001.

The Phenomenology of Polarized DIS

7. *Anselmino M., Efremov A., Leader E.* // Phys. Rep. 1995. V. 261. P. 1–124.

8. *Lampe B., Reya E.* // Phys. Rep. 2000. V. 332. P. 1–164.

9. *Diakonov D. et al.* // Nucl. Phys. B. 1996. V. 480. P. 341.

10. *Fries R., Schafer A.* hep-ph/9805509.

11. *Bravar A. et al.* // Phys. Lett. B. 1998. V. 421. P. 349.

12. *Glück M., Reya E.* // Z. Phys. C. 1988. V. 39. P. 569.

13. *Burkardt M., Jaffe R. L.* // Phys. Rev. Lett. 1993. V. 70. P. 2537.

14. *Jaffe R. L.* // Phys. Rev. D. 1996. V. 54. P. 6581.

15. *Saull P. R. B.* GenDVCS: A Monte Carlo Generator for Deeply Virtual Compton Scattering at HERA. Sept. 1999;
    http://www-zeus.desy.de/saull/public/dvcs.html

16. *Kotzinian A. M.* // Nucl. Phys. B. 1995. V. 441. P. 234.

17. *Mulders P. J., Tangerman R. D.* // Nucl. Phys. B. 1996. V. 461. P. 197.

18. *Oganessyan K. A. et al.* hep-ph/9808368.

19. *De Sanctis E., Nowak W.-D., Oganessyan K. A.* // Phys. Lett. B. 2000. V. 483. P. 69;
    Efremov A. V. et al. // Ibid. V. 478. P. 94.

20. *Collins J.* // Nucl. Phys. B. 1993. V. 396. P. 161.

21. *Kotzinian A. M.* // Nucl. Phys. B. 1995. V. 441. P. 234.

22. *Mulders P. J., Tangerman R. D.* // Nucl. Phys. B. 1996. V. 461. P. 197.

23. *Jaffe R., Jin X., Tang J.* // Phys. Rev. Lett. 1998. V. 80. P. 1166.

24. *Anselmino M., Boglione M., Murgia F.* // Phys. Lett. B. 1995. V. 362. P. 164.

25. *Mulders P., Boglione M.* // Nucl. Phys. A. 2000. V. 666–667. P. 257;
    Kotzinian A. M. et al. // Ibid. P. 290.

26. *Artru X., Czyzewski J., Yabuki H.* // Z. Phys. C. 1997. V. 73. P. 527.

27. *Anselmino M., Boglione M., Murgia F.* hep-ph/9810228.

28. *Frankfurt L. L. et al.* // Phys. Lett. B. 1989. V. 230. P. 141.

29. *Shevchenko O., Sissakain A., Samoilov V.* JINR Preprint E2-2000-268. Dubna, 2000.

30. *Barone V. et al.* // Phys. Rep. 2002. V. 359. P. 1.

Experimental Data on Polarized DIS

31. *Alguard M. et al. (SLAC E80)* // Phys. Rev. Lett. 1978. V. 41. P. 70.

32. *Baum G. et al. (SLAC E130)* // Phys. Rev. Lett. 1983. V. 51. P. 1135.

33. *Ashman J. et al. (EMC)* // Nucl. Phys. D. 1989. V. 328. P. 1.

34. *Hughes V. H., Kuti J.* // Ann. Rev. Nucl. Sci. 1983. V. 33. P. 611.

35. *Adeva B. et al. (SMC)* // Phys. Lett. B. 1993. V. 302. P. 533.

36. *Adams D. et al. (SMC)* // Phys. Lett. B. 1994. V. 329. P. 399.

37. *Adams D. et al. (SMC)* // Ibid. V. 336. P. 125.

38. *Adams D. et al. (SMC)* // Phys. Lett. B. 1995. V. 357. P. 248.

39. *Adams D. et al. (SMC)* // Phys. Lett. B. 1996. V. 369. P. 93.

40. *Adams D. et al. (SMC)* // Phys. Lett. B. 1997. V. 396. P. 338.

41. *Adeva B. et al. (SMC).* CERN-PPE/97-118; Phys. Lett. B. 1997. V. 412. P. 414.

42. *Adams D. et al. (SMC)* // Phys. Rev. D. 1997. V. 56. P. 5330.

43. *Adeva B. et al. (SMC)* // Phys. Rev. D. 1998. V. 58. P. 112001.

44. *Adeva B. et al. (SMC)* // Ibid. P. 112002.

45. *Adeva B. et al. (SMC)* // Phys. Rev. D. 1999. V. 60. P. 072004.

46. *Adeva B. et al. (SMC)* // Phys. Lett. B. 1998. V. 420. P. 180.

47. *Bravar A. (SMC)* // Nucl. Phys. B (Proc. Suppl.). 1999. V. 79. P. 520.

48. *Adams D. et al. (SMC)* // Phys. Lett. B. 1994. V. 320. P. 363.

49. *Abe K. et al. (E143)* // Phys. Rev. Lett. 1995. V. 74. P. 346.

50. *Abe K. et al. (E143)* // Phys. Lett. B. 1995. V. 364. P. 61.

51. *Abe K. et al. (E143)* // Phys. Rev. Lett. 1995. V. 75. P. 25.

52. *Abe K. et al. (E143)* // Phys. Rev. Lett. 1996. V. 76. P. 587.

53. *Abe K. et al. (E143)* // Phys. Rev. D. 1998. V. 58. P. 112003.

54. *Anthony P. L. et al. (E142)* // Phys. Rev. Lett. 1993. V. 71. P. 959.

55. *Anthony P. L. et al. (E142)* // Phys. Rev. D. 1996. V. 54. P. 6620.

56. *Ackerstaff K. et al. (HERMES)* // Phys. Lett. B. 1997. V. 404. P. 383.

57. *Airapetian A. et al. (HERMES)* // Phys. Lett. B. 1998. V. 442. P. 484.

58. *Ackerstaff K. et al. (HERMES)* // Ibid. V. 444. P. 531.

59. *Airapetian A. et al. (HERMES)* // Phys. Rev. Lett. 2000. V. 84. P. 4047.

60. *Di Nezza P. (HERMES).* Spin Azimuthal Asymmetries in Semi-Inclusive Pion Electro-Production at HERMES // Talk given at the 14th Intern. Spin Physics Symposium (SPIN 2000), Osaka, Japan, Oct. 16–21, 2000.

61. *Airapetian A. et al. (HERMES)* // Phys. Lett. B. 2002. V. 535. P. 85–92;
    Avakian H. (HERMES). Results on Azimuthal Asymmetries from DIS Experiments // Talk
    given at the RIKEN BNL Research Center Workshop on «Future Transversity Measurements»
    held at Brookhaven National Laboratory, Upton, USA, Sept. 18–20, 2000;
    Miller A. (HERMES). Spin Azimuthal Asymmetries in Semi-Inclusive and Exclusive DIS //
    7th Conf. on Intersections of Particle and Nuclear Physics (CIPANP 2000), Quebec City,
    Canada, May 22–28, 2000.

62. *Ackerstaff K. et al. (HERMES)* // Phys. Lett. B. 1999. V. 464. P. 123.

63. *Airapetian A. et al. (HERMES)* // Phys. Lett. B. 2000. V. 494. P. 1.

64. *Airapetian A. et al. (HERMES)* // Phys. Rev. Lett. 2000. V. 84. P. 2584.

65. *Aschenauer E. C. (HERMES)* // 9th Workshop on Deep Inelastic Scattering and QCD, Bologna,
    Italy, Apr. 27–May 1, 2001.

66. *Rith K. (HERMES)* // Prog. Part. Nucl. Phys. 2002. V. 49. P. 245.

67. *Tallini H. A. (HERMES)*. A Measurement of the Quark Spin Distribution of the Nucleon at
    HERMES. PhD Thesis. Oliver Lodge Laboratory, University of Liverpool, UK, 1998.

68. *Airapetian A. et al. (HERMES)* // Eur. Phys. J. C. 2003. V. 26. P. 527–538.

69. *Abe K. et al. (E154)*. Preprint SLAC-PUB-7459; Phys. Rev. Lett. 1997. V. 79. P. 26–30.

70. *Abe K. et al. (E154)* // Phys. Lett. B. 1997. V. 404. P. 1377.

71. *Abe K. et al. (E154)* // Ibid. V. 405. P. 180.

72. *Abe K. et al. (E154)* // Phys. Rev. Lett. 1997. V. 79. P. 26.

73. *Anthony P. L. et al. (E155)* // Phys. Lett. B. 1999. V. 463. P. 339.

74. *Anthony P. L. et al. (E155)* // Ibid. V. 458. P. 529.

75. *Anthony P. L. et al. (E155)* // Phys. Lett. B. 2000. V. 493. P. 19.

76. *Anthony P. L. et al. (E155)* // Phys. Lett. B. 2003. V. 553. P. 18.

77. *Savin I. A.* Results on Polarized Deep Inelastic Scattering from SMC // Proc. of the 13th
    Intern. Symp. on High Energy Spin Phys. (SPIN98), Protvino, Sept. 8–12, 1998 / Ed. by
    N. E. Tyurin et al. P. 78–94.

78. *Windmolders R.* // Nucl. Phys. B. 1999. V. 79. P. 51.

79. *Saull P. R. B. (ZEUS)*. Prompt Photon Production and Observation of Deeply Virtual Compton
    Scattering // Proc. of Intern. Europhysics Conf. on High-Energy Physics (EPS-HEP 99),
    Tampere, Finland, July 15–21, 1999; hep-ex/0003030.

80. *Stamen R. (H1)* // Talk presented at DIS 2000, April 2000; submitted to the 30th Intern. Conf.
    on High-Energy Physics (ICHEP'2000), Osaka, Japan, July 2000;
    Adloff C. et al. hep-ex/0107005. 2001.

81. *Amarian M. (HERMES)*. Deeply Virtual Compton Scattering and Exclusive Meson Production
    at HERMES // Intern. Workshop on Skewed Parton Distributions and Lepton-Nucleon Scat-
    tering, DESY, Hamburg, Germany, Sept. 11–12, 2000;
    Airapetian A. et al. hep-ex/0106068. 2001; Phys. Rev. Lett. 2001. V. 87. P. 182001.

82. *Stepanyan S. et al. (CLAS)*. hep-ex/0107043. 2001; Phys. Rev. Lett. 2001. V. 87. P. 182002.

83. Jefferson Lab. Proposal. The Science Driving the 12 GeV Upgrade of CEBAF. 2001.

84. *Kivel N., Polyakov M., Vandehaeshen M.* // Phys. Rev. D. 2001. V. 63. P. 114014.

85. *Adams D. et al.* // Phys. Lett. B. 1991. V. 264. P. 462;
    Bravar A. et al. // Phys. Rev. Lett. 1996. V. 77. P. 2626;
    Bonner B. E. et al. // Phys. Rev. D. 1990. V. 41. P. 13;
    Bravar A. // Proc. of the 13th Intern. Symp. on High Energy Spin Phys. (SPIN98), Protvino,
    Sept. 1998. P. 167.

    Radiative Corrections

86. *Akushevich I., Shumeiko N.* // J. Phys. G. 1994. V. 20. P. 513.

    The QCD Treatment of Unpolarized Structure Functions

87. *Gribov V. N., Lipatov L. N.* // Sov. J. Nucl. Phys. 1972. V. 15. P. 1138; 675.

88. *Altarelli G., Parisi G.* // Nucl. Phys. B. 1977. V. 126. P. 298.

89. *Martin A. D., Roberts R. G., Stirling W. J.* // Phys. Lett. B. 1996. V. 387. P. 419.

90. *Glück M., Reya E., Vogt A.* // Z. Phys. C. 1995. V. 67. P. 433.

91. *Botts J. et al.* // Phys. Lett. B. 1993. V. 304. P. 159.

92. *Furmanski W., Petronzio R.* // Z. Phys. C. 1982. V. 11. P. 293.

93. *Glück M., Reya E., Vogt A.* // Z. Phys. C. 1990. V. 48. P. 471

    The QCD Treatment of Polarized Structure Function

94. *Altarelli G.* // Phys. Rep. 1982. V. 81. P. 1.

95. *Zijlstra E. B., van Neerven W. L.* // Nucl. Phys. D. 1994. V. 417. P. 61.

96. *Ball R. D., Forte S., Ridolfi G.* // Nucl. Phys. B. 1995. V. 444. P. 287;
    Erratum // Ibid. V. 449. P. 680; Phys. Lett. B. 1996. V. 378. P. 255.

97. *Mertig R., van Neerven W. L.* // Z. Phys. C. 1996. V. 70. P. 637.

98. *Vogelsang W.* // Phys. Rev. D. 1996. V. 54. P. 2023.

99. *Gehrmann T., Stirling W. J.* // Z. Phys. C. 1995. V. 65. P. 461.

100. *Fasching D.* Ph. D. thesis, Northwestern University. 1996; hep-ph/9610261.

101. *Adler S., Bardeen W.* // Phys. Rev. 1969. V. 182. P. 1517.

102. *Altarelli G., Ross G. G.* // Phys. Lett. B. 1988. V. 212. P. 391.

103. *Efremov A. V., Teryaev O. V.* JINR Preprint E2-88-287. Dubna, 1988.

104. *Carlitz R. D., Collins J. C., Mueller A. H.* // Phys. Lett. B. 1988. V. 214. P. 229.

105. *Cheng H. Y.* hep-ph/9512267.

106. *Ball R. D., Forte S., Ridolfi G.* // Phys. Lett. B. 1996. V. 378. P. 255.

107. *Glück M. et al.* // Phys. Rev. D. 1996. V. 53. P. 4775.

108. *Gehrmann T., Stirling W. J.* // Ibid. P. 6100.

109. *Altarelli G. et al.* // Acta Phys. Pol. B. 1998. V. 29. P. 1145; hep-ph/9803237;
    Forte S. et al. hep-ph/9808462;
    Altarelli G. et al. // Nucl. Phys. B. 1998. V. 534. P. 277.

110. *Leader E. et al.* // Phys. Rev. D. 1998. V. 58. P. 114028;
    Leader E. et al. // Phys. Lett. B. 1998. V. 445. P. 232.

111. *De Florian D., Sampayo O., Sassot R.* // Phys. Rev. D. 1998. V. 57. P. 5803.

112. *Radyushkin A. V.* // Phys. Lett. B. 1996. V. 380. P. 417; Phys. Rev. D. 1997. V. 56. P. 5524.

113. *Ji X.* // Phys. Rev. Lett. 1997. V. 78. P. 610; Phys. Rev. D. 1997. V. 55. P. 7114.

114. *Vanderhaeghen M., Guichon P. A.* // Prog. Part. Nucl. Phys. 1998. V. 41. P. 125;
     Vanderhaeghen M., Guichon P. A., Guidal M. // Phys. Rev. Lett. 1998. V. 80. P. 5064.

115. *Diehl M. et al.* // Phys. Lett. B. 1997. V. 411. P. 193.

116. *Goeke K. et al.* hep-ph/0106012. 2001;
     Goeke K. et al. // Prog. Part. Nucl. Phys. 2001. V. 47. P. 401.

117. *Balitsky I., Ji X.* // Phys. Rev. Lett. 1997. V. 79. P. 1225.

118. *Barone V., Calarco T., Drago A.* // Phys. Lett. B. 1998. V. 431. P. 405.

119. *Collins J., Freund A.* // Phys. Rev. D. 1999. V. 59. P. 074009;
     Frankfurt L. L., Freund A., Strikman M. // Phys. Rev. D. 1998. V. 58. P. 114001;
     Frankfurt L. L., Freund A., Strikman M. // Ibid. V. 59. P. 119901;
     Freund A. hep-ph/9903488.

Small-x Behaviour of g_1

120. *Bass S. D., Landshoff P. V.* // Phys. Lett. B. 1994. V. 336. P. 537.

121. *Close F. E., Roberts R. G.* // Ibid. P. 257.

122. *Ellis J.* // Proc. of the 12th Intern. Symp. on High Energy Spin Physicis (SPIN96), Amsterdam, 1996. Singapore, 1997; hep-ph/9611208.

123. *Bartels J., Ermolaev B. I., Ryskin M. G.* // Z. Phys. C. 1996. V. 70. P. 273; DESY-96-025; hep-ph/9603204.

Sum Rules for g_1 and g_2

124. *Bjorken J. D.* // Phys. Rev. 1966. V. 148. P. 1467; Phys. Rev. D. 1970. V. 1. P. 376.

125. *Larin S. A., Tkachev F. V., Vermaseren J. A. M.* // Phys. Rev. Lett. 1991. V. 66. P. 862.

126. *Larin S. A., Vermaseren J. A. M.* // Phys. Lett. B. 1991. V. 259. P. 345.

127. *Kataev A. L., Starshenko V.* // Mod. Phys. Lett. A. 1995. V. 10. P. 235; hep-ph/9405294; hep-ph/9502348.

128. *Kodaira J. et al.* // Phys. Rev. D. 1979. V. 20. P. 627; Nucl. Phys. B. 1979. V. 159. P. 99.

129. *Kodaira J.* // Nucl. Phys. B. 1980. V. 165. P. 129.

130. *Larin S. A.* // Phys. Lett. B. 1994. V. 334. P. 192.

131. *Kataev A. L.* // Phys. Rev. D. 1994. V. 50. P. 5469.

132. *Ellis J., Jaffe R. L.* // Phys. Rev. D. 1974. V. 9. P. 1444; V. 10. P. 1669.

133. *Close F. E., Roberts R. G.* // Phys. Lett. B. 1993. V. 316. P. 165.

134. *Nagaitsev A. P. et al.* // JINR Rapid Commun. 1995. No. 3[71].

135. *Ellis J., Karliner M.* CERN-TH-7324/94.

136. *Altarelli G., Ridolfi G.* CERN-TH-7415/94;
     Altarelli G., Nason P., Ridolfi G. // Phys. Lett. B. 1994. V. 320. P. 152.

137. *Gerasimov S. B.* // Sov. J. Nucl. Phys. 1966. V. 2. P. 430;
     Drell S. B., Hearn A. C. // Phys. Rev. Lett. 1966. V. 16. P. 908.

138. *Anselmino M., Ioffe B. L., Leader E.* // Sov. J. Nucl. Phys. 1989. V. 49. P. 136.

139. *Burkert V. D. et al.* // Phys. Lett. B. 1992. V. 296. P. 223; Phys. Rev. D. 1993. V. 47. P. 46; JETP. 1994. V. 105. P. 1153;
Li Z. et al. // Phys. Rev. D. 1993. V. 47. P. 1854; 1992. V. 46. P. 70; 1994. V. 50. P. 3119;
Soffer J., Teryaev O. // Phys. Rev. Lett. 1993. V. 70. P. 3373; Phys. Rev. D. 1995. V. 51. P. 25;
Ji X. // Phys. Lett. B. 1993. V. 309. P. 187.

140. *Burkert V., Li Z. J.* // Phys. Rev. D. 1993. V. 47. P. 46.

141. *Aznauryan I. G.* // Phys. At. Nucl. 1995. V. 58. P. 1014.

142. *Ma W. X. et al.* // Nucl. Phys. A. 1998. V. 635. P. 497;
Drechsel D. et al. // Phys. Rev. D. 1999. V. 59. P. 094021;
Dong Y. // Phys. Lett. B. 1998. V. 425. P. 177;
Scholten O., Korchin A. Yu. // Eur. Phys. J. A. 1999. V. 6. P. 211.

143. *Karliner I.* // Phys. Rev. D. 1973. V. 7. P. 2717;
Workman R. L., Arndt R. A. // Phys. Rev. D. 1992. V. 45. P. 1789;
Sandorfi A. M., Whisnant C. S., Khandaker M. // Phys. Rev. D. 1994. V. 50. P. R6681;
Drechsel D., Krein G. // Phys. Rev. D. 1998. V. 58. P. 116009.

144. *Bianchi N., Thomas E.* // Phys. Lett. B. 1999. V. 450. P. 439.

145. *Thomas A.* // Nucl. Phys. B. 1999. V. 79. P. 591;
Ahrens J. et al. // Phys. Rev. Lett. 2001. V. 87. P. 0229939.

146. *Helbing K.* // Nucl. Phys. B (Proc. Suppl.). 2002. V. 105. P. 113.

147. *Shuryak E. V., Vainshtein A. I.* // Nucl. Phys. B. 1982. V. 201. P. 141.

148. *Jaffe R. L., Ji X.* // Phys. Rev. D. 1991. V. 43. P. 724.

149. *Mankiewicz L., Rysak Z.* // Ibid. P. 733.

150. *Artru X., Mekhfi M.* // Z. Phys. C. 1990. V. 45. P. 669.

151. *Song X.* // Phys. Rev. D. 1996. V. 54. P. 1955.

152. *Cortes J., Pire B., Ralston J.* // Z. Phys. C. 1992. V. 55. P. 409.

153. *Stratmann M.* // Z. Phys. C. 1993. V. 60. P. 763.

154. *Ji X., Unrau P.* // Phys. Lett. B. 1994. V. 333. P. 228.

155. *Stein E. et al.* // Phys. Lett. B. 1995. V. 343. P. 369.

156. *Balitsky I., Braun Y., Kolesnichenko A.* // Phys. Lett. B. 1990. V. 242. P. 245; Erratum. 1993. V. 318. C. 648.

157. *Gockeler M. et al.* // Phys. Rev. D. 1996. V. 53. P. 2317.

158. *Wandzura S., Wilczek Y.* // Phys. Lett. B. 1977. V. 72. P. 195.

159. *Burkhardt H., Cottingham W. N.* // Ann. Phys. 1970. V. 56. P. 453.

160. *Sasaki K.* // Phys. Rev. D. 1998. V. 58. P. 094007.

161. *Efremov A., Leader E., Teryaev O.* // Phys. Rev. D. 1997. V. 55. P. 4307.

Experimental Set-Ups

162. *Doble N. et al.* // Nucl. Instr. Meth. A. 1994. V. 343. P. 351.

163. *Wu C. S. et al.* // Phys. Rev. 1957. V. 105. P. 1413.

164. *Brown K. L. et al.* CERN Yellow Rep. 80-04.

165. *Iselin C.* CERN Yellow Rep. 74-17.

166. *Kyynarainen J. //* Nucl. Instr. Meth. A. 1995. V. 356. P. 47.

167. *Kramer D. //* Ibid. P. 79.

168. *Dael A. et al. //* IEEE Trans. Magn. 1992. V. 28. P. 560.

169. *Kisselev Y. et al. //* Zh. Eksp. Teor. Fiz. 1988. V. 94(2). P. 344; Sov. Phys. JETP. 1988. V. 67. P. 413.

170. *Le Goff J. M. et al. //* Nucl. Instr. Meth. A. 1995. V. 356. P. 96.

171. *Kyynarainen J. //* AIP Conf. Proc. 1995. V. 343. P. 555.

172. *Adeva B. et al. (SMC) //* Nucl. Instr. Meth. A. 1996. V. 372. P. 339.

173. *Adeva B. et al. (SMC) //* Nucl. Instr. Meth. A. 1994. V. 349. P. 334.

174. *Adams D. et al. (SMC).* CERN-EP/99-90; Nucl. Instr. Meth. A. 2000. V. 443. P. 1.

175. *Adams D. et al. (SMC) //* Nucl. Instr. Meth. A. 1999. V. 437. P. 23;
Kisselev Yu. F. on behalf of SMC // Nucl. Instr. Meth. A. 1995. V. 356. P. 99;
Kisselev Yu. F., Niinikoski T. L. Preprint CERN-PPE/96-146. 1996;
Kisselev Yu. F., Niinikoski T. O. // Proc. of the 12th Intern. Symp. on High Energy Spin Physics (SPIN96), Amsterdam, 1996. Singapore, 1997. P. 389.

176. *Dulya C. et al. (SMC) //* Nucl. Instr. Meth. A. 1997. V. 398. P. 109.

177. *Adams D. et al. (SMC) //* Nucl. Instr. Meth. A. 1999. V. 435. P. 354.

178. *Hayashi N. et al. //* Nucl. Instr. Meth. A. 1995. V. 356. P. 91.

179. *Abragam A.* The Principle of Nuclear Magnetism. Oxford, 1961.

180. *Allkofer O. C. et al. //* Nucl. Instr. Meth. A. 1981. V. 179. P. 445.

181. *Coulter K. et al. (HERMES Proposal).* DESY-PRC 90/01. 1990; DESY-PRC 93/06. 1993.

182. *Sokolov A. A., Ternov I. M. //* Sov. Phys. Dokl. 1964. V. 8. P. 1203.

183. *Ackerstaff K. et al. (HERMES Spectrometer) //* Nucl. Instr. Meth. A. 1998. V. 417. P. 230.

184. *Alley R. et al. //* Nucl. Instr. Meth. A. 1995. V. 365. P. 1.

185. *Crabb D. G., Day D. B. //* Ibid. P. 9.

186. *Wagner B. et al. //* Nucl. Instr. Meth. A. 1990. V. 294. P. 541;
De Raad L. L. et al. // Phys. Rev. D. 1975. V. 11. P. 1586.

187. *Court G. et al. //* Nucl. Instr. Meth. A. 1993. V. 324. P. 433.

188. *Carver T. R., Bouchiat M. A., Varnum C. M. //* Phys. Rev. Lett. 1960. V. 5. P. 373;
Bhaskar N. D., Happer W., McClelland T. // Phys. Rev. Lett. 1982. V. 49. P. 25;
Happer W. et al. // Phys. Rev. A. 1984. V. 29. P. 3092;
Johnson J. et al. // Nucl. Instr. Meth. A. 1995. V. 356. P. 148.

189. *Bultmann S. et al.* SLAC-PUB-7904. 1998;
Rondon O. A. // Phys. Rev. C. 1999. V. 60. P. 35201.

190. RHIC SPIN Proposal. BNL.

191. COMPASS Proposal. CERN/SPSLC/P297. 1996.

192. *Burtin E. et al.* Outline for a Deeply Virtual Compton Scattering Experiment at COMPASS. DAPNIA-SPhN, CEA-Saclay. Private communication;
d'Nose N. Possible experiments on DVCS in COMPASS // Report at the Workshop «Future Physics at COMPASS», CERN, Sept. 27, 2002;
http://compass-cw2002.web.cern.ch/compass-cw2002/programme.html

193. *Amandruz E. et al. //* Phys. Lett. B. 1993. V. 316. P. 429.

194. *Doncel M.G., De Rafael E.* **//** Nuovo Cim. UA. 1971. P. 363;
     Whitlow L. et al. **//** Phys. Lett. B. 1990. V. 250. P. 193.

195. *Abe K. et al.* **//** Phys. Lett. B. 1999. V. 452. P. 194.

196. *Arneodo K. et al. (NMC)* **//** Phys. Lett. B. 1995. V. 364. P. 107;
     Anthony P. L. et al. (SLAC E155) **//** Phys. Lett. B. 1999. V. 458. P. 529.

197. *Buck W., Gross F.* **//** Phys. Rev. D. 1979. V. 20. P. 2361;
     Zuilhof M. Z., Tjon J. A. **//** Phys. Rev. C. 1980. V. 22. P. 2369;
     Lacombe M. et al. **//** Ibid. V. 21. P. 861;
     Machleidt R. et al. **//** Phys. Rep. 1987. V. 149. P. 1;
     Umnikov A. Yu. et al. University of Alberta. Preprint Alberta-Thy-29-94. 1994.

198. *Soffer J., Teryaev O.* **//** Phys. Lett. B. 2000. V. 490. P. 106.

199. *Gagunashvili N. et al.* JINR Commun. E1-96-483. Dubna, 1996.